

AD-A057 439

NAVAL RESEARCH LAB WASHINGTON D C
HIGH-ENERGY ION EXPANSION IN LASER-PLASMA INTERACTIONS.(U)
APR 78 R DECOSTE
NRL-MR-3774

F/G 20/9

UNCLASSIFIED

NL

1 OF 2
AD A057439



AD A057439

AD No. _____
DDC FILE COPY

251 9

Memorandum Report

6

High-Energy Ion Expansion in Laser-Plasma Interactions.

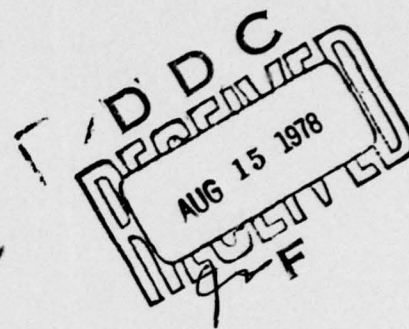
LEVEL III

4049 504

10

REAL DECOSTE

Plasma Physics Division
and
University of Maryland



11

Apr 78

12

142p

14

NRL-MR-3774

78 08 14 217



NAVAL RESEARCH LABORATORY
Washington, D.C.

Approved for public release; distribution unlimited.

251 950

Gen

20. ABSTRACT (Continued)

electron emission. A technique using charge exchange to differentiate ion species with the same A/Z but using different Z is also described.

The experimental results indicate that an important fraction of the ion expansion energy is transported by energetic ions. The energetic ion blow-off from CH_n and CD_2 targets is highly ionized with multi-peak structure on the energy distribution of the ion species. From the CD_2 target results, it is also found that the C^{+6} ions were already fully ionized before the acceleration phase of their expansion with the H^+ or D^+ ions. The H^+ ions carry an important fraction of the fast ion energy due to a preferential acceleration of the H^+ ions over heavier C^{+6} ions.

A 1-D fluid model describes the ambipolar expansion of hot electrons and either one or two relatively cold ion species from an electron pressure gradient. For CD_n , the plasma expansion is adequately represented by a single ion species, whereas for CH_n , two-ion fluids are required to account for the energy and the relative behavior of the high-energy ion species.

sub n

ACCESSION FOR	
NTIS	in the Section <input checked="" type="checkbox"/>
DDC	in the Section <input type="checkbox"/>
UNCLASSIFIED	<input type="checkbox"/>
JUSTIFIED	
BY	
DISTRIBUTION/AVAILABILITY CODES	
Dist.	AVAIL. and/or SPECIAL
A	-

CONTENTS

INTRODUCTION	1
I – MOTIVATION AND REVIEW OF LASER-PLASMA INTERACTION STUDIES	3
A. Motivation for High Energy Ion Studies	3
(a) Review of the Laser-Fusion Concept	3
(b) High Energy Ions and Laser-Fusion	6
B. Review of High Energy Ion Studies	7
(a) Experimental Observations of Energetic Ions	8
(b) Acceleration Mechanisms of Energetic Ions	10
1. Magnetic Fields	10
2. Ponderomotive Force	11
3. Plasma Pressure	12
3.1. Ion Acceleration Model	12
3.1.1. Electron Temperature	14
3.1.2. Density Gradient	16
3.2 Numerical Simulations	17
II – EXPERIMENTAL APPARATUS AND METHODS	18
A. Laser	18
B. Target Facility	20
C. Ion Diagnostics	26
(a) Instrumentation	26
1. Charge Collectors	28
2. Ion Analyzer	30
2.1 Introduction	31

2.2. Theory	33
2.2.1. Particle Dynamics	33
2.2.2. Energy and Species Resolution	36
2.2.3. Space Charge Forces	37
2.3. Analyzer Design and Operation	39
2.3.1. Design Considerations	40
2.3.2. Ion Detection System	43
2.4. Detector Calibration	48
2.4.1. Secondary Electron Ejection	50
2.4.2. Experimental Technique	51
2.4.3. Secondary Electron Coefficient Measurements	55
(b) Methods	57
1. Ion Velocity Distributions	60
2. Ion Energy Distributions	61
2.1. Data Analysis	61
2.2. Charge Exchange Technique	63
III - EXPERIMENTAL RESULTS	71
A. High Energy Ion Expansion	71
(a) Observations Normal to the Target Surface at High Irradiance	73
1. Ion Energy Distributions	73
2. Charge Collector Results	78
3. Ion Energy Content	80
(b) Observations at Other Target Angles and Irradiances	83
1. Ion Energy Distributions	83
2. Angular Dependence of Ion Expansion	85
3. Irradiance Dependence of Energetic Ions	90
(c) Ionization Effects During Ion Expansion	92
B. X-Ray Emission	96
C. Summary and Discussion	98

IV – THEORETICAL MODEL	101
A. Fluid Model	102
(a) Basic Geometry and Parameters	102
(b) Fluid Representation	104
(c) Validity of the Model	106
B. Computational Model	109
(a) Numerical Solution of Fluid Equations	109
(b) Asymptotic Ion Energy Distributions	112
C. Analytic Single-Ion-Species Expansion Model	113
D. Multi-Species Plasma Expansion	117
SUMMARY AND CONCLUSIONS	125
ACKNOWLEDGMENTS	127
APPENDIX A: Boundary Conditions for the Computational Model	129
REFERENCES	131

High-Energy Ion Expansion in Laser-Plasma Interactions

INTRODUCTION

Although laser-produced plasmas have been studied for about 15 years, relatively little is known about the physics of the laser-plasma interaction. This is especially true of the case of plasma produced by very high intensity irradiation of solid targets. These plasmas are relatively very difficult to study experimentally because of their highly transient nature and rather microscopic dimensions. Consequently, experimental comparisons with theoretical predictions have not been very precise. In the context of the laser-fusion application, however, the study of these high density and temperature plasmas remains very important.

The work reported here concentrates on one aspect of the high irradiance (about 10^{16} W/cm²) Nd-laser-produced-plasma, namely, the acceleration of high energy ions during the laser-plasma interaction. As far as the physics is concerned, the observation of energetic ions, i.e. non-thermal ions, suggests that "anomalous" processes dominate the laser-plasma interaction at high laser irradiance. For laser-fusion, the emission of energetic ions can represent an important energy loss mechanism of the absorbed laser light.

Until two or three years ago, not much was known definitively about the importance and significance of energetic ions observed at high laser fluxes incident upon solid targets. The aim of this work was therefore to improve our understanding of the acceleration mechanism of high energy ions. For that purpose, new ion diagnostics were first developed and tested. Next, detailed measurements of the ion expansion were performed under various target conditions at high irradiance. At the same time, a theoretical model, consistent with the observed high

energy ion features and other physical evidence, was developed. Very briefly, Chapter I discuss the experimental and theoretical background, Chapter II the instrumentation, Chapter III the experimental results and Chapter IV the theoretical model.

In Chapter I, we first review the physical processes involved in laser-fusion and the negative aspects of high energy ions in this context. Next, we concentrate on the high irradiance laser-plasma interaction regime and survey the main physical processes identified to be important in the generation of high energy ions.

In Chapter II, we describe the experimental apparatus and diagnostic methods. This includes a detailed description of the design, usage and calibration of a high energy ion analyzer designed for laser-produced-plasma studies. Special diagnostic techniques using charge exchange and the ion analyzer are also discussed in detail.

In Chapter III, we present the results of energetic ion and x-ray spectral measurements obtained at high target irradiance for $1.06\mu\text{m}$ irradiation. Features of the high energy ion species are discussed and correlated to an energetic ion acceleration model.

In Chapter IV, a simple multi-species ion expansion model is presented and is shown to qualitatively agree with the experimental observations. Essentially, the model shows that the large plasma pressure gradients, which are believed to exist at high target irradiance, can account for the energy and the relative behavior of the observed high energy ion species.

The Conclusion contains a summary of results, a discussion and suggestions for future work.

Chapter I
MOTIVATION AND REVIEW
OF LASER-PLASMA INTERACTION STUDIES

The physics of the interaction of high power laser light with solid matter is interesting in its own right, but the basic motivation for the research effort in this field is the possibility of initiating a controlled thermonuclear fusion reaction on a laboratory scale. The first section of this chapter provides an introduction to the basic features of the physics of laser-fusion. Emphasis is placed on absorption and energy transport rather than compression processes and the thermonuclear burn. The description is by no means exhaustive but it does indicate current trends and the role of energetic ions. In the second section, we focus our attention on the laser-plasma interaction with an emphasis on the production of high energy ions. We review both the experimental observations of energetic ions and some theoretical acceleration models that have been suggested in the literature. Since the production of energetic ions is closely related to the absorption and transport of the laser energy, we also review the physical processes believed, at the present time, to be involved in the laser-plasma interaction.

A. Motivation for High Energy Ion Studies

In this section, we review briefly the basic physical processes involved in the laser-fusion concept with emphasis on the laser-plasma interaction itself. The role and origin of the high energy ions will also be pointed out, although more details about this subject will be given in the next section.

a) Review of the Laser-Fusion Concept

The concept of laser-fusion involves compressing a small quantity of deuterium-tritium mixture to high densities in a near isentropic fashion, by employing the high pressures generated by laser irradiation¹⁻⁴. In a typical laser-fusion target interaction, four main processes can be identified, namely: the absorption of the laser energy in the low density plasma atmosphere surrounding the pellet, the transport of this energy to the spherically converging

compression front, the compression itself, and the thermonuclear burn.

A schematic representation of the mass density and electron temperature profiles during the compression of the spherical shell target by the laser beams is shown in Fig. 1.1. Figure 1.1 shows three different regions during the compression process. The incident laser radiation can penetrate the plasma corona of the target up to the critical density n_c , i.e., up to the electron density where the laser light frequency ω_0 equals the plasma frequency $\omega_{pe} = (4\pi n_e e^2 / m_e)^{1/2}$. The light absorption, therefore, occurs in the underdense region at densities $n_e \leq n_c$ [$n_c = 10^{21} \text{ cm}^{-3}$ for $1.06\mu\text{m}$ radiation (Nd-glass laser) and 10^{-9} cm^{-3} for $10.6\mu\text{m}$ radiation (CO_2 -gas laser)]. Thermal conduction carries energy from the absorption region to the ablation surface. The ablation region separates cold dense material from the hot lower density plasma and it is in this region that the core is compressed due to acceleration by the rocket reaction of the ablation. Inside the ablation surface, the D-T fuel is adiabatically compressed to a super-dense pellet core without significant heating during the implosion. In the final collapsing phase, the compressed fuel is shock heated to initiate the thermonuclear burn at the center of the dense core. From then on, the thermonuclear reaction can be self-sustained from the energy released by the emitted 3.5 MeV α -particles (when their mean-free-path is less than the diameter of the dense compressed core). The major idea in laser-fusion is to use the laser to compress the fuel to a very high density ($100\text{-}1000 \text{ g/cm}^3$) rather than to heat all of it.

The targets and laser parameters suitable for laser-fusion have not yet been demonstrated. Different laser irradiances, wavelengths, pulse lengths and shapes with their relevant target designs and expectations have been considered. We do not intend, here, to discuss the relative merits of the different pellet designs and concepts. We will rather briefly consider, in general terms, the physics common to most laser-fusion approaches, namely: the absorption and transport of the laser energy.

If laser-fusion is to succeed, the laser radiation must be efficiently absorbed. For long pulses and low irradiance, the laser energy is mostly absorbed by classical inverse bremsstrahlung^{5, 6} on the low temperature, long density profile. High irradiance and short

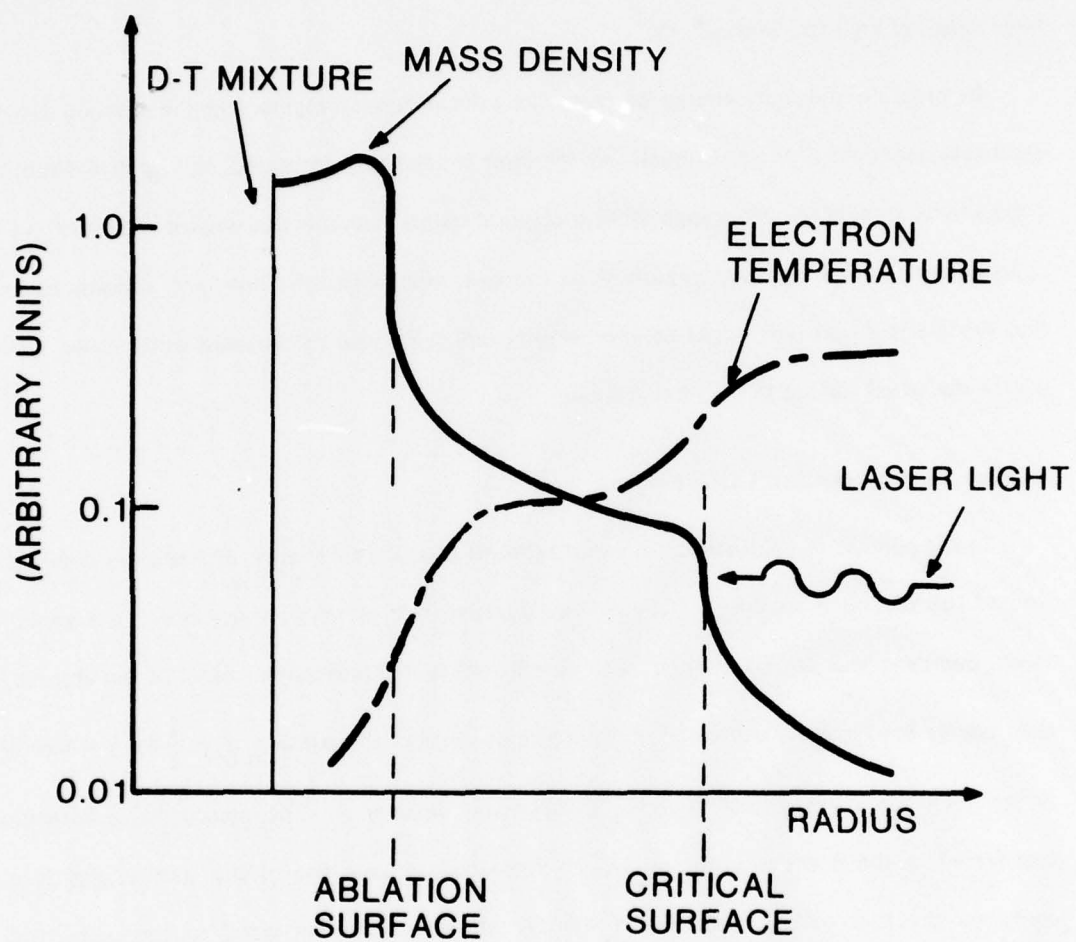


Fig. 1.1. Laser fusion pellet implosion by intense laser light. The laser energy penetrates the plasma to the critical density surface, where it is carried to the ablation surface by thermal electron conduction.

pulses produce high temperatures and steep density profiles which favor anomalous absorption at or near the critical surface. In this case, since the laser intensity is high, parametric backscattering instabilities⁷ such as Raman and Brillouin may occur, and reflect the laser radiation before the absorption region is reached. Brillouin backscattering,⁸ for example, has recently been shown to be potentially harmful for some laser-fusion schemes involving time-structured laser pulses at high irradiances.^{9, 10}

In order to transport energy between the critical density region and the ablation front, good thermal conduction is essential. As the laser irradiance is increased, the electron thermal conductivity is believed to change from a classical collision dominated regime⁵ (Spitzer) to a collisionless thermal transport regime.¹¹ In the collisionless regime, however, indications are that the thermal transport might be anomalously reduced below its free streaming value. This will be discussed further in the next section.

b) High Energy Ions and Laser-Fusion

In the context of good absorption and transport of the laser energy, and efficient compression of the fuel, it is easy to understand the negative role of high energy ions. In a general sense, energetic ions are inconsistent with an efficient fuel compression. Most of the absorbed laser energy is eventually converted into ion kinetic energy of expansion $E_i = \frac{1}{2}Mv^2$, where M is the total ion mass ablated with an average ion velocity v . The associated momentum transferred to the pellet is given by $2E_i/v$. Since the ultimate use of the laser energy is to compress the fuel pellet, a maximum transfer of momentum or recoil to the pellet wall (pusher) should be provided by the ion blow-off upon the conversion of the thermal energy into kinetic energy of expansion. For a fixed amount of laser energy and, therefore, ion energy E_i , the momentum transfer is increased with lower velocity and higher ablated mass. Ablating more target mass at a lower velocity, i.e., more ions with lower kinetic energies, is therefore more consistent with an efficient pellet implosion.

The high energy ions we are referring to in the present work contain a small fraction of

the total ion blow-off mass but transport an important fraction of the ion expansion energy. Therefore, these high energy ions cannot contribute efficiently to the pellet compression. Moreover, we will see in the next section that these high energy ions are most likely produced in the underdense region where a fraction of the absorbed laser energy is directly converted into ion expansion energy. Since the energy expended in the production of energetic ions is not even transported to the ablation surface, the high energy ions can be considered as an important energy loss mechanism for the absorbed laser energy.

It is noteworthy that although the high energy ions represent an important energy loss at high laser irradiance, the physics is likely to be different at lower intensities or for structured laser pulses. We will see later that appropriate conditions for the production of high energy ions are a hot plasma corona coupled with a relatively steep density gradient. Lower irradiances and longer laser pulse lengths should give lower corona temperatures and longer density gradients. The energy losses due to the acceleration of energetic ions in the underdense region would then be reduced and more energy could become available for transport to the ablation region.

B. Review of High Energy Ion Studies

In this section, we review the experimental observations of energetic ions reported in the literature and some theoretical models that have been suggested for the acceleration mechanism of high energy ions. Since the production of energetic ions is closely related to the absorption and transport of the laser energy in and out of the underdense region, we also survey the physical processes believed, at the present time, to be involved in the laser-plasma interaction. The energetic ion studies discussed in this section cover the period of time up to early 1978 for both $1.06\mu\text{m}$ and $10.6\mu\text{m}$ laser radiation. In Chapters II, III and IV, complete details of our own results will be given.

Although most of the interest in laser-fusion is related to the compression of a pellet core, an important fraction of the experimental and theoretical work concerns the absorption and transport of the laser energy. For such studies, single beam irradiation of planar targets is usually sufficient and, therefore, both planar and spherical target geometries are reviewed here.

a) Experimental Observations of Energetic Ions

Most experimental observations, until recently, of energetic ions were of an indirect nature with measurements of the ion velocities rather than energies. Theoretical and computational studies were rather limited to qualitative predictions of the high energy ion phenomena, because of uncertainties in the experimental data and difficulties in modeling the ion expansion. In this section, we review the experimental observations reported in the literature.

At this point, a few words are in order about ion diagnostics commonly used with laser-produced plasmas. Most ion measurements reported in the literature are made with charge collectors and/or ion analyzers. Both diagnostics measure the ion current passing through a small surface a distance far enough from the target that the ion time-of-flight is much longer than the initial ion acceleration time. Charge collectors measure asymptotic ion velocity distributions, whereas ion analyzers measure the asymptotic energy distribution of each ion species. As we will see in Chapter II, charge collectors are very simple to use but can only yield qualitative and sometimes misleading information. On the other hand, ion analyzers can give quantitative information, if properly calibrated, but they are cumbersome to use.

The asymptotic energy distributions of expanding ions measured with a charge collector at high laser irradiance can usually be divided into two distinct ion groups: a low-energy ion group, containing most of the ablated target mass, and a small, but significant group, of higher-energy ions. The low-energy ion group has been extensively studied both theoretically¹²⁻¹⁵ and experimentally,¹⁵⁻¹⁹ although mostly at lower irradiance. It corresponds to the thermal expansion of the high density low temperature plasma. Recombination can affect the ion population in different ionization states during the thermal expansion but, as we will see later, it is not important for the high energy ion component.

The high energy ion group contains a small fraction of the ions and, possibly, between 20% and 80% of the ion expansion energy, depending on the experimental conditions and the arbitrary definition used for the separation between energetic and thermal ions. As we will see in Chapter III, for the case of planar targets, the fraction of the ion energy in energetic ions is

also angle dependent. Typically, 50% of the total ion energy is reported to be carried by energetic ions for conditions similar to those of Chapter III (5×10^{15} W/cm² on glass microspheres²⁰, and 10^{16} W/cm² on small C₈H₈ disks²¹). Under different experimental conditions, 5×10^{13} W/cm² at 10.6 μ m on deuterium targets, up to 80% of the expansion energy has been reported²².

Most laser-produced plasmas contain several ion species. The ion species can be due to different atomic weight or different ionization stages of the same element. In Chapter III, we will show that recombination and ionization effects are negligible during the acceleration and expansion phase of the high energy ions. Some qualitative information about the properties of the accelerating field can therefore be obtained from the observed ratio of different ion species. For example, the early time peaks²³⁻²⁵ on a charge collector were labeled as different ion species A_i/Z_i , identified by their respective time-of-flight $t_i \propto (A_i/Z_i)^{1/2}$. In this case, the basic assumption is that the ion species were accelerated by the same electrostatic target potential ϕ , such that $E_i = Z_i \phi$. The relationship between the ion energy of each species would then be

$$E_i/Z_i = \text{const.} \quad (1.1)$$

This model was physically possible but later experiments,²⁶⁻²⁹ using an ion analyzer instead of charge collector, showed that most of the charge collectors peaks are in fact structure on the energy distribution of the same ion species. This will be shown in detail in Chapter III.

A second assumption, different from the one leading to Eq. (1.1), is to assume that the expansion of the faster ion species decreases self-consistently the electric field such that the acceleration time and the electric field are essentially the same for all the ion species²⁹. From the equation of motion of an ion accelerated in a uniform electrostatic field E_0 the rate of change of ion kinetic energy ($E_i = \frac{1}{2} m_i v_i^2$) is given by

$$\frac{d}{dt} \frac{E_i}{Z_i} = \frac{Z_i}{A_i} \frac{e^2}{m_p} E_0^2 t. \quad (1.2)$$

Equation (1.1) corresponds to the case of different ion species accelerated through the same uniform electrostatic field for *different* time intervals, i.e., $t \propto (A_i/Z_i)^{1/2}$. If, instead, the

acceleration times and the electric fields are the *same* for all the ion species, then, according to Eq. (1.2), the final relationship between the ion species would be given by

$$(E_i/Z_i) (A_i/Z_i) = \text{const.} \quad (1.3)$$

Basically, Eq. (1.3) says that lower A_i/Z_i ion species are accelerated to higher E_i/Z_i than the ion species with higher A_i/Z_i . This assumption will be shown to be in approximate agreement with the experimental results presented in Chapter III. In Chapter IV we will also verify the validity of Eq. (1.3) from the results of a numerical expansion model.

b) Acceleration Mechanism of Energetic Ions

At least three acceleration mechanism have been suggested for the acceleration of energetic ions: the self-generated magnetic fields, the ponderomotive force and the plasma pressure. The self-generated magnetic fields are, in general, important in laser-plasma interaction, but their effect upon energetic ions is not thought to be very strong. The ponderomotive force was among the first mechanisms suggested for energetic ion acceleration³⁰. However, more detailed theoretical work is still required before its relative importance can be assessed. The third and most likely candidate is the plasma pressure. Experimental and theoretical evidences now indicate that the plasma conditions are favorable for this mechanism to play a significant role. In fact, in Chapter III and IV of the present work, we show that the hot electron pressure gradients, now believed to exist at high target irradiance, can account for our experimental observations of high energy ion distributions.

1. Magnetic Fields

The importance of spontaneously generated magnetic fields in laser-produced plasmas³¹⁻³⁴ has now been generally recognized. A number of mechanisms have been proposed^{31,35,37} by which the magnetic fields may occur, but one of the most important contributions comes from currents driven by electron pressure in non-uniform plasmas³¹, i.e., the $\nabla n_e \times \nabla T_e$ source term where n_e and T_e are respectively the electron density and temperature.

Here, we consider only direct effects of magnetic fields on the ion acceleration. Indirect

effects, such as reduction of the electron heat transport which would affect the pressure gradient, are considered in a later section.

The magnetic fields generated in the absorption region and convected outwards may cause acceleration of the lower-density plasma through the $\bar{J} \times \bar{B}$ force, where \bar{J} is the plasma current. A theoretical analysis of this possibility is described in Ref. 38 and 39. The $\bar{J} \times \bar{B}$ force may be thought of as a magnetic pressure $B^2/2\mu_0$, directed away from regions of large B . Thus, when the $\bar{J} \times \bar{B}$ force becomes comparable to the plasma pressure gradient, we can expect to find enhanced acceleration away from the interaction region, similar to pinch effects⁴⁰. The ratio of plasma to magnetic pressure

$$\beta = \frac{3}{2} k (n_e T_e + n_i T_i) / (B^2 / 2\mu_0)$$

provides an indication of the importance of $\bar{J} \times \bar{B}$ forces. Although the magnetic pressure is generally lower than the plasma pressure, $\bar{J} \times \bar{B}$ forces may become significant at lower plasma densities. Deflection of ion trajectories through $\bar{J} \times \bar{B}$ forces or $\bar{E} \times \bar{B}$ drifts⁴¹ could also affect the angular distribution of the energetic ion emission.

2. Ponderomotive Force

Originally invoked³⁰ in connection with laser-plasma interactions to explain energetic ions, the ponderomotive force is nothing more than radiation pressure in a plasma. The time average Lorentz force on a single electron in the electromagnetic field of the incident laser light yields the ponderomotive force^{7,42}

$$\bar{f}_{pe} = - \frac{2\pi e^2}{m_e \omega_o^2} \bar{\nabla} \frac{|E_o|^2}{8\pi}, \quad (1.4)$$

where ω_o is the laser frequency and $|E_o|$ the electric field amplitude. As the electrons respond to \bar{f}_{pe} on a density gradient, they generate a charge separation electric field \bar{E}_s such that $\bar{f}_{pe} - e\bar{E}_s = 0$. The ions therefore feel a force $Z_i e \bar{E}_s$, such that the ponderomotive force on a single ion is given by

$$\bar{f}_{pi} = - \frac{2\pi Z_i e^2}{m_e \omega_o^2} \bar{\nabla} \frac{|E_o|^2}{8\pi}. \quad (1.5)$$

A standing wave pattern⁴³ of the electromagnetic field associated with the incident laser light near the critical density is shown in Fig. 1.2. When the energy density of the incident radiation is comparable to the thermal energy of the plasma, the ponderomotive force can modify and deform the density profile. For $x < x_0$ in Fig. 1.2, the ponderomotive force can push on the plasma and density profile steepening can occur. This effect and its consequences on the laser-plasma interaction are discussed in the next section. Here, we concentrate on the ponderomotive force as an acceleration mechanism for energetic ions. As seen from Eq. (1.5), the light force is conservative. Therefore, only those ions near an amplitude maximum can be accelerated by the field in Fig. 1.2. An analytical evaluation of the number and energy distribution of energetic ions that can be produced by the ponderomotive force is reported in ref. 44 and 45. However, because of uncertainties in the spatial and temporal distribution of the accelerating force field, the results are inconclusive as to whether the ponderomotive force can significantly contribute to the production of energetic ions⁴⁶. At this point, the ponderomotive effect remains a possibility as an acceleration mechanism but both experiments and numerical simulations using fluid codes are probably required to obtain more quantitative information.

3. Plasma Pressure

3.1 Ion Acceleration Model

An important mechanism which can produce strong electric fields at high irradiance is the plasma pressure itself. In the presence of a density gradient, hot electrons try to separate from the ions. The electron expansion, however, is limited by the self-consistent electric field created by the ion-electron separation. This electric field, in turn, accelerates the ions such that an ambipolar expansion results. More quantitatively, the electron pressure p_e must be balanced by the self-consistent electric field \bar{E} according to

$$e n_e \bar{E} = -\nabla p_e, \quad (1.6)$$

where $p_e = n_e k T_e$ and n_e and T_e are respectively the electron density and temperature. Therefore, a large pressure gradient results in a strong electric field which can accelerate ions to high

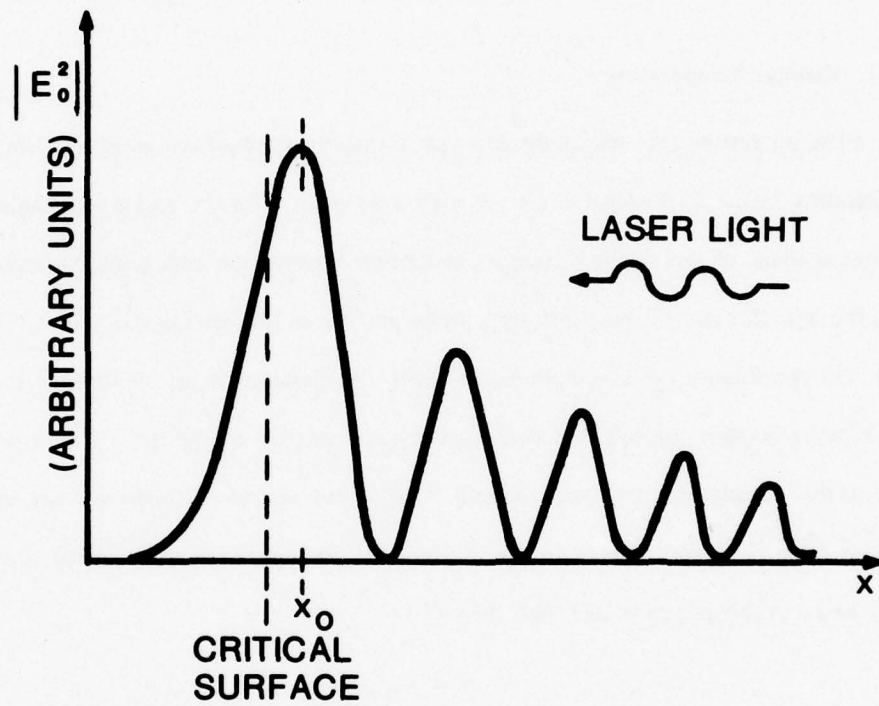


Fig. 1.2. Standing wave pattern of a light wave along the plasma density gradient.

energies.

If we assume that the hot electron temperature is almost uniform in the underdense region, then Eq. (1.6) becomes

$$e n_e \bar{E} \approx -k T_e \nabla n_e. \quad (1.7)$$

This shows that the combination of a relatively high electron temperature and a steep density profile result in strong electric fields. Experimental observations and theoretical calculations now indicate that both of these specific plasma conditions exist at high target irradiance.

3.1.1. Electron temperature

First we review the absorption and heat transport mechanisms which control the electron temperature in the underdense region at high irradiance. The absorption mechanism can affect the initial shape of the electron energy distribution whereas the heat transport mechanism controls the heat flux out of the absorption region and hence the heating rate. Under high incident laser flux conditions, the assumptions on which the classical theory of thermal transport rests can become invalid. Indeed, the collisional mean-free-path of the heated electrons can easily exceed the density gradient scale length. An upper bound estimate on the electron heat transfer from the absorption region is obtained by assuming that the thermal flux instantaneously balances the absorbed laser light flux Q , i.e.,

$$Q = f n_e m_e v_e^3, \quad (1.8)$$

where $v_e = (2kT_e/m_e)^{1/2}$, n_e is the electron density and f is a coefficient of order unity.

For the case where $n_e = n_c$ (critical density) and $f \approx 1$, Eq. (1.8) becomes the so-called flux-limited or free-streaming estimate of the size of electron energy transfer. Some thermal transport experiments⁴⁷⁻⁴⁹ however, suggest that the energy flux is somewhat reduced from its free-streaming value, i.e., $f < 1$ is in better agreement with experimental observations. Several theoretical models have been put forward to explain the flux limiting. Ion acoustic turbulence with strong fluctuating electrostatic fields produced by the ion waves could inhibit the transport of energy by electrons.^{50-52, 20} Ion turbulence is also a possible absorption mechanism

for the laser energy near the critical region^{51, 52, 20}. Alternatively, electron turbulence or the self-generated magnetic fields^{53, 38} discussed above, could reduce heat conduction. The overall effect of flux limiting would be to increase the electron temperature in the absorption region, since the absorbed energy cannot be carried away efficiently.

In the case discussed above electrons are stochastically heated in a region around the critical density, while the heat flux is inhibited by assuming $f < 1$. An alternative approach to Eq. (1.8) is assuming $f \approx 1$ but allowing only a fraction α of the electrons to be heated.⁵⁴ This case corresponds to $n_e = \alpha n_c$ with $\alpha < 1$ and $f \approx 1$ in Eq. (1.8). The reduced number of hot electrons is then associated with an energetic electron tail on the electron energy distribution in the critical region¹¹. Resonant absorption⁵⁵, which can produce such an energetic electron tail, has been observed in numerical simulations^{56, 57} to play a significant rôle at high flux intensities. Resonant absorption, however, does not seem to be efficient enough to account for all the absorbed laser energy⁵⁸, suggesting that other absorption mechanism are involved.

A lower bound estimate of the electron temperature to be used in Eq. (1.8) can be obtained from continuum x-ray measurements. As we will see in Chapter III, the x-ray spectra obtained at high irradiance yield at least two electron temperatures corresponding to two electron groups at different characteristic energies. An electron temperature of 15 keV is typically inferred for the smaller, energetic, electron group. Since this temperature estimate is spatially and temporally integrated, local temperatures for a short time could be much higher and in fact consistent with the high electron temperature predicted by most theoretical models.^{53, 59, 38}

In summary, it is not clear at the present time whether the laser energy is absorbed by a reduced number of energetic electrons ($\alpha < 1$) or the temperature is increased due to flux-limiting ($f < 1$). In any case, hot electrons do exist in the absorption region and the energy is not efficiently transported to the overdense region at high laser irradiance.

3.1.2. Density Gradient

The second requirement to obtain a strong electric field is the presence of a steep electron density gradient. Probing beam techniques coupled with interferometry have been used to measure the density profile for both 1.06 and 10.6 μm irradiation. For the short laser pulse lengths commonly used at high irradiance, the density profile is expected to remain relatively steep (less than a few tens of laser wavelengths) during the laser irradiation, due to finite ion expansion velocities. At high irradiance, however, the energy density of the incident radiation is comparable to the thermal energy of the plasma, such that the ponderomotive force in Eq. (1.5) can modify and deform the density profile. Density profile steepening up to one wavelength of the laser radiation has recently been observed^{60, 61} near the critical surface. Such a steep rise through the critical density region is much shorter than would be predicted for a freely expanding plasma and is consistent with radiation pressure effects.^{62, 63}

This profile steepening in turn can affect the absorption and transport of energy⁵⁴. As an example, it is predicted that these effects enhance the role of resonance absorption while reducing that due to parametric processes, which require shallow gradients. It is noteworthy that radiation pressure affects mostly the critical density region such that the profile scale length above n_c and below $0.1 n_c$ can be longer than at n_c . The effect of different profile scale lengths on the acceleration of high energy ions will be discussed in Chapter IV.

At densities below critical, where the plasma expansion can be approximated as freely expanding into vacuum, analytical self-similar solutions⁶⁴⁻⁶⁶ have been found for the case of an isothermal single-species plasma expansion. The general numerical solutions presented in Chapter IV will be shown to reduce to the self-similar solutions under proper conditions.

At the very low density vacuum interface, where the Debye length becomes comparable to the profile scale length, the self-similar model breaks down and a different numerical modeling of the expansion is required⁶⁷. Vacuum interface expansion can yield very energetic ions but because of the very small number of ions involved, it will not be discussed further in this report.

3.2. Numerical Simulations

It appears that large hot electron pressure gradients probably do exist at high target irradiance. Theoretical studies with computational models have also shown that these large pressure gradients give rise to electric fields strong enough to accelerate ions to high energies. Some plasma simulations, typically fluid codes, consider the complete history of the laser-plasma interactions with absorption and transport of the energy as well as the hydrodynamic response (expansion) of the plasma.^{21, 20, 38, 59} Others are simply expansion models which assume initial plasma conditions after the laser is turned off and concentrate on the parametrization of the ion expansion.^{11, 8, 9} All these simulations use a single ion species to model the ion expansion. They give useful information about the occurrence of energetic ions, but as we will see, do not describe well multiple-ion species expansions. In Chapter IV, we show that, although the hot electron pressure gradient model can account for the presence of high energy ions, a multi-ion species description is usually required to model most laboratory plasma expansions.

CHAPTER II

EXPERIMENTAL APPARATUS AND METHODS

The experimental apparatus used here for high energy ion studies consists of a high power laser, a target irradiation facility and the ion diagnostics. This chapter is accordingly divided into three sections, covering these three instrumentation topics separately. In the first section, the characteristics of the high power glass laser relevant to our experiments are discussed briefly. Next, we describe the target facility with some standard laser beam and general plasma diagnostics. In the last section, details about the ion diagnostics as well as the data analysis are presented.

A. Laser

The Pharos-II glass laser system at the Naval Research Laboratory was used for the target irradiation experiments that will be described in the next chapter. Pharos-II is a 0.6 TW high power glass laser system suitable for single or two beam illumination of solid targets. Since the laser system has been extensively described elsewhere,^{70, 71} only the parameters relevant to our experiments will be discussed in this section.

A schematic of the laser is shown in Fig. 2.1. The Nd:Yag master oscillator-preamplifier section generates a pulse of nominal energy 15 mJ in 75 psec at 1.064 μm . This pulse is amplified by the next three rod amplifiers (diameter $\phi = 23$ mm, 32 mm, 45 mm) to 0.5 J at the end of the intermediate amplifier section and then split into two beams. The final amplification stages consist of a 45 mm diameter rod amplifier and two 67 mm aperture disc amplifiers. Except for the oscillator-preamplifier section, the laser chain uses silicate Nd-doped glass optically pumped by flash lamps. Faraday rotators are used to protect the system against damage to the optical components from the laser energy reflected back from the target. The output energy per laser beam can be as high as 25 J for a 75 psec FWHM pulse.

The first Pockels cell selects a single pulse from the oscillator mode-locked pulse train. Further optical isolation for suppressing other laser pulses and fluorescence are provided by two

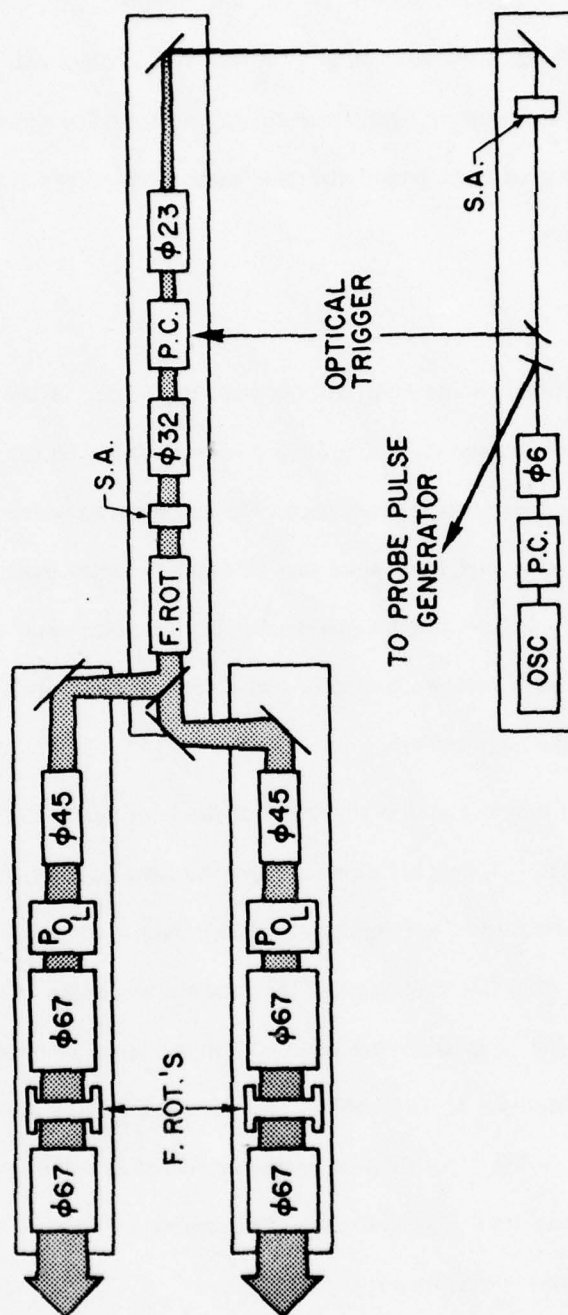


Fig. 2.1. Pharos II laser schematic. The oscillator preamplifier section generates a pulse of nominal energy 15 mJ in 75 ps. This is amplified to 0.5 J in the intermediate amplifier section and then split into two beams. The final amplification stages consist of a 45 mm diameter rod and two 67 mm aperture disk amplifiers. Also indicated are Pockell cells (P.C.), saturable absorbers (S.A.), and Faraday rotators (F.ROT.).

saturable absorbers. The second Pockels cell was not operational during our experiments. With the two saturable absorbers and the first Pockels cell, a contrast ratio of $\sim 10^7$ is achieved between the main pulse and any prepulse level. At this low prepulse level, the plasma can only be created by the arrival of the main laser pulse.⁷⁰ It was also verified that other long pulse pre-irradiation sources such as flashlamp light, fluorescence and amplified spontaneous emission does not damage the surface of most target materials used in these experiments before the arrival of the main laser pulse.

B. Target Facility

The experiments described in the next chapter were performed at the Pharos-II target facility.⁷² Again, only a brief description of the facility with emphasis on the components and diagnostics relevant to our experiments is given here. We first proceed with a brief description of the laser beam characteristics and focal properties relevant to target irradiation. Next, we briefly describe the target facility with some plasma diagnostics which were used to measure some plasma emissions related to the production of high energy ions. Details of the ion diagnostics will be presented in the next sections.

Fig. 2.2 shows schematically the optical alignment of the laser beams in the target facility. The two beams from the Pharos-II laser are directed from the laser building to the target facility through two 21 m evacuated tubes terminated with BK-7 glass windows. The backreflected and transmitted laser light within the solid angle of the lens are monitored from reflections off the tube window surfaces. The laser beams are directed into the target chamber by two dielectric turning mirrors with reflectivity of about 98%. The remainder of the beam energy passes through the turning mirrors and is used for such beam diagnostics as calorimetry, beam divergence monitoring and prepulse level measurements. The beams are focused by lenses within the target chamber onto various targets for experiments.

Five degrees of freedom are available to properly locate a target at the common focal point of both lenses. Both lenses can be translated along the laser beam axis (Z-axis). The target holder can be translated along the Z-axis as well as the X and Y-axes. The translation is

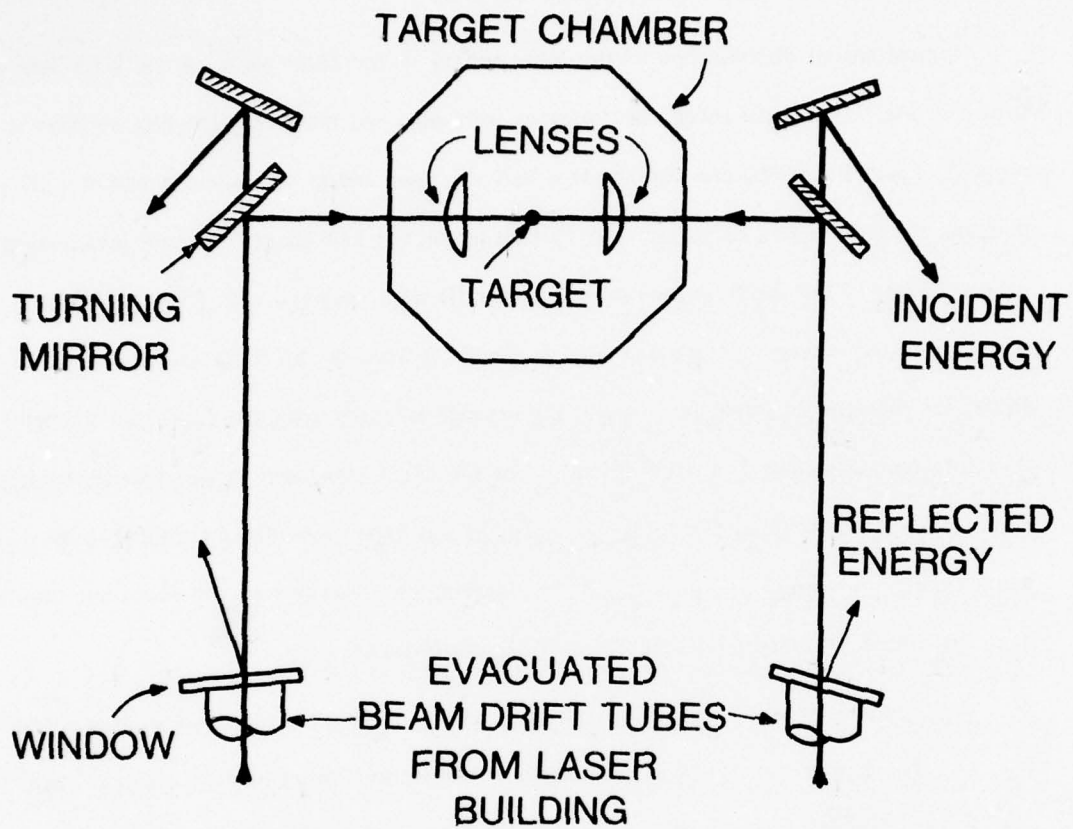


Fig. 2.2. Schematic of the optical alignment of the laser beams in the target facility.

done by remotely controlled precision stepping motors. For most experiments described in this report, a single laser beam was used to irradiate planar slab targets. The target surface was then simply positioned in the focal plane of one of the lenses. However, for proper irradiation of mass-limited targets such as microspheres, for example, the focal points of both lenses must coincide spatially and temporally at the target location.

Typical spatial distributions of the laser energy in the focal plane of the f/1.9 lens are shown in Fig. 2.3. These energy distributions were obtained using the thin-film ablation technique.⁷⁰ From Fig. 2.3b, one can see that half the laser energy is contained within a 20 μm diameter for 8 J incident on target. For 16 J on target, the half-energy diameter is increased to 25 μm . Most of the results presented in Chapter III were obtained with 8 to 16 J incident on target. The half-energy content diameter is usually defined as the focal spot diameter. If 12 Joules are incident on target in 75 psec, the average intensity over the focal spot diameter is therefore approximately $2 \times 10^{16} \text{ W/cm}^2$. For the f/1.9 lens used in our experiments, the depth-of-focus for doubling the focal spot diameter was experimentally determined to be $\pm 100 \mu\text{m}$. Unless mentioned in the text, all the experiments described in the following chapters were performed with target surfaces within the depth-of-focus.

A schematic of the target facility with some of its components and diagnostics is shown in Fig. 2.4. The target chamber is an octahedron-rhombicube with an average diameter of about 0.75 meter. The chamber is evacuated by a 1000 L/sec turbomolecular pump to a pressure as low as a few times 10^{-6} Torr. A nitrogen cold trap is added to the chamber to reduce the base pressure to the 10^{-7} Torr range when necessary. Some target shots were taken at this lower pressure to verify that electron capture by the expanding ions scales with the chamber pressure. It was found that a target chamber pressure of about 5×10^{-6} Torr is sufficient to avoid charge exchange of the expanding plasma with the ambient gas under our experimental conditions. More details about charge exchange processes will be discussed in a later section.

Figure 2.4 also shows some of the laser beam diagnostics used on every shot. The divergence of each laser beam is monitored using a mask and related to a possible focal shift.⁷⁰ The

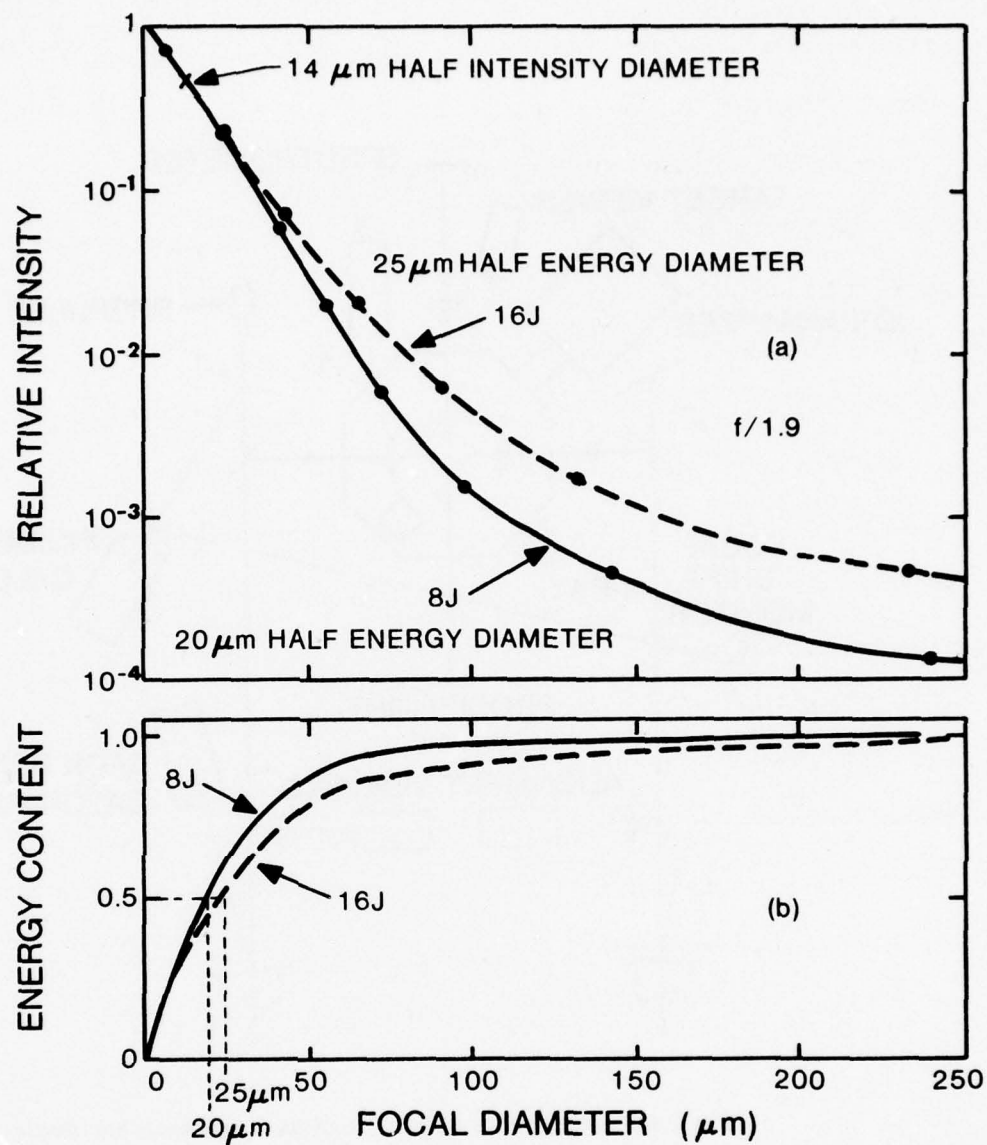


Fig. 2.3. (a) Laser energy distributions at best focus of a $f/1.9$ lens. (b) Energy content of the distributions with increasing focal diameter.

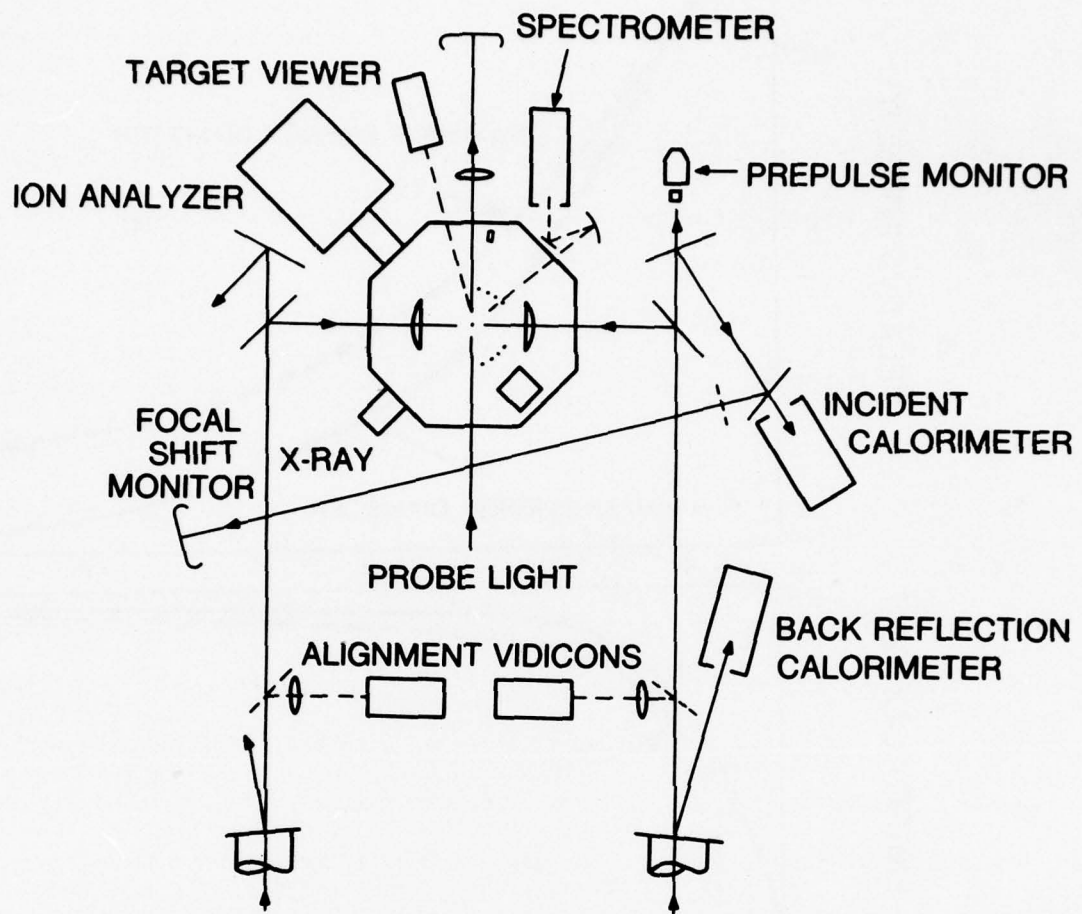


Fig. 2.4. Target facility with some of its components and diagnostics.

prepulse level is measured with PIN diodes and the possible occurrence of a "satellite" pulse is monitored with a vacuum photodiode.⁷² The incident and backscattered laser energy per beam is recorded with calorimeters. An array of small calorimeters is often used inside the target chamber to record the scattered laser light energy distribution.⁹

Most plasma diagnostics are directly attached to the chamber. The location of some of them is schematically shown in Fig. 2.4. The signal lines are directed to the oscilloscope screen room or the computerized data acquisition screen room through shielded conduits designed for minimum ground loop propagation. The ion analyzer,²⁶ used to measure the energy distributions of the expanding ions, will be described in detail in the next sections. Most of the other diagnostics, schematically shown in Fig. 2.4, have been described in details elsewhere and the reader should refer to the appropriate references for more information. Briefly, the continuum X-ray emission from 1 keV to more than 100 keV is measured on every shot by an array of 7 filter-PIN diodes and 8 filter-scintillators-PMT combinations.⁷³ An X-ray spectrum can be unfolded from these data which yield information about the velocity distribution of the confined plasma electrons. The velocity distribution of the high energy electrons escaping the plasma is measured by small magnetic spectrographs.⁷⁴ A probing laser pulse³⁴ (Fig. 2.1) which is synchronized with the main laser pulse, frequency-doubled and Raman shifted to 6328 Å is available for shadowgraphy, interferometry, Faraday rotation, etc. Information about the density gradient scalelengths and the self-generated magnetic field have been obtained using this probing beam. We will show later how the electron energy distribution and the density scalelength are related to the production of high energy ions.

All the ion energy distributions presented in this work were obtained with the electrostatic ion energy analyzer described in the next section. However, another interesting technique which was used in our facility to obtain the ion energy distribution is described by E.A. McLean *et al.*⁷⁵ In this method, the plasma blow-off is observed perpendicular to the laser axis a short distance from the target surface with a monochromator coupled to a fast photomultiplier. The photomultiplier temporally resolves a spectral line corresponding to a specific ionization stage of

the expanding ion species. The ion velocity is then determined from the time-of-flight and the distance between the target surface and the point of observation. An oscillogram of a carbon line observed 1 cm from the target surface is shown in Fig. 2.5. The early peaks before the main peak are associated with high energy ions. Some advantages of this technique are that the measurements can be made close to the target and within the lens cone, i.e., where ion collectors cannot conveniently be used. However, a separate measurement of the electron density and temperature is required to get absolute number densities of the ion species. The spectroscopic technique remains interesting but further developments are required to obtain quantitative results.

C. Ion Diagnostics

In this section, we describe the two ion diagnostics used to measure the expanding high energy ions, namely, charge collectors and a high energy ion analyzer. First, we discuss the design considerations and calibration of the instruments. Second, we describe the experimental method and the data reduction process which yield the asymptotic energy distributions of the ion species.

a) Instrumentation

The experimental apparatus used for ion measurements consists of some charge collectors and a high energy ion analyzer. Both diagnostics measure the ion current through a small surface a large distance away from the target. The charge collectors yield qualitative information about the asymptotic ion velocity distribution, whereas the ion analyzer, by spatially separating the different ion species, measures the energy distribution of each ion species. Both diagnostics rely on the ion time-of-flight measurement between the target surface and the detector location to give the ion velocity. This assumption is valid as long as the ion time-of-flight and flight distance between the target and the collection point remain respectively much larger than the characteristic emission times and dimensions of the ion source.

The charge collectors are conventional devices used extensively by most laboratories

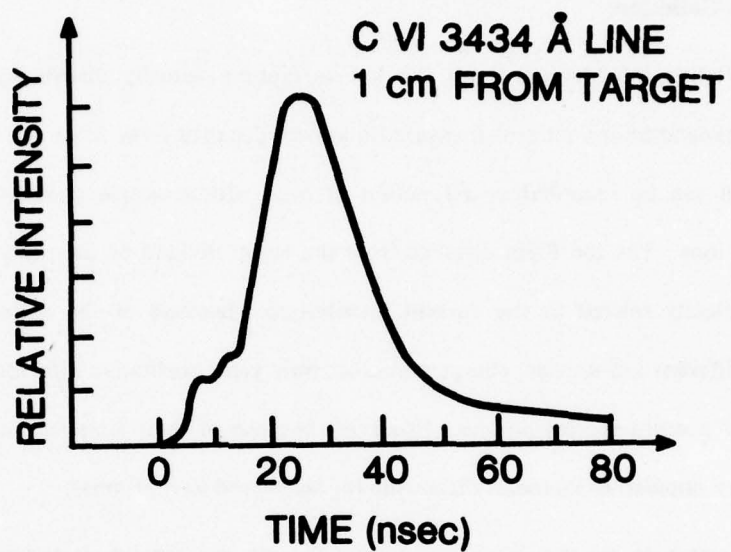


Fig. 2.5. Oscilloscope trace of the C VI 3434-Å ion line intensity observed 1 cm from the target surface. The time $t = 0$ is the time the short laser pulse strikes the target.

engaged in laser-produced plasma diagnostics. The ion analyzer was, however, specifically designed for the measurement of energetic ion distributions from a laser-produced plasma. Design considerations for the ion analyzer are, therefore, presented in detail together with typical applications. A novel absolute calibration technique, involving the measurement of secondary electron emission coefficients for the type of detectors used in the analyzer and charge collectors, is also described.

1. Charge Collectors

Qualitative information about the ion asymptotic velocity distribution can be obtained from the expanding ion current measured a known distance away from the target surface. The ion current can be recorded as a function of time with a simple conductor intercepting the expanding ions. The ion flight distance from the target divided by the time of flight then gives the ion velocity related to the current distribution. Because of the inability to differentiate between different ion species, charge collectors only yield qualitative informations about the ion blow-off of a multi-species plasma. However, because of their simplicity and small size, they remain very popular as a general diagnostic for laser-produced plasmas.

A diagram of the charge collectors used for our experiments is shown in Fig. 2.6a. The mesh spacing is chosen to be less than the Debye length of the impinging plasma [$\lambda_D = (T_e/4\pi n_e e^2)^{1/2}$] so that the electrons can be separated from the ions upon entering the electric field region between the mesh and the collector. Typically, a grounded copper mesh, with 125 lines/inch and 65% optical transmission, is used 1.5 mm in front of the copper collector.

For each ion striking the collector, a number of secondary electrons γ are emitted which is a function of the mass, velocity and charge of the incident ion. In our collector, a bias voltage is applied to the collector in order to repel most secondary electrons to the electrical ground. The problem of secondary electron emission will be addressed specifically in the section dealing with the calibration of the ion analyzer detection system.

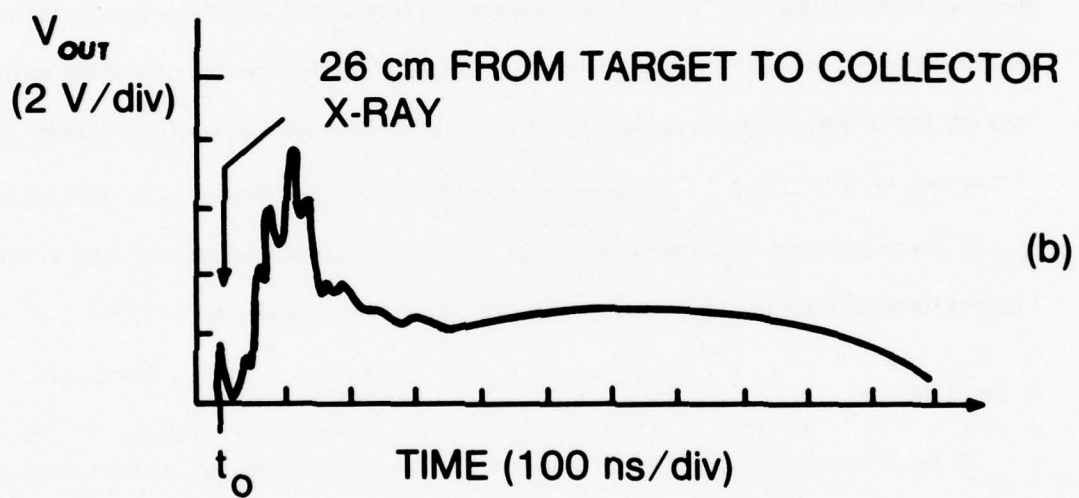
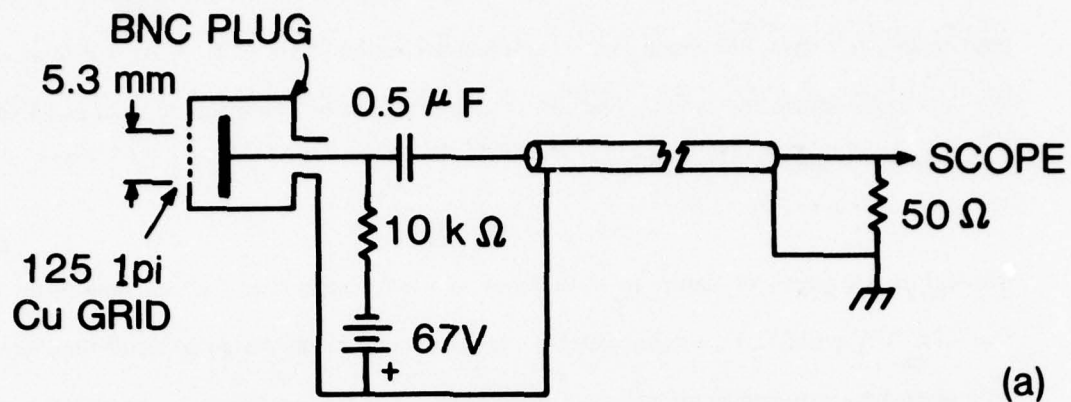


Fig. 2.6. (a) Schematic of the charge collector used to measure the asymptotic velocity distribution of ion blow-offs. (b) Typical oscilloscope trace of a charge collector located 26 cm from the target surface. The output signal is recorded into 50 Ω.

The collector current is recorded with an oscilloscope. Figure 2.6b shows a typical oscilloscope trace of a charge collector located a distance L (26 cm) from the target surface. The first peak is due to X-rays, ultraviolet and fast electrons ejecting electrons from the collector when the laser pulse struck the target. The rise of this peak can be conveniently used as an initial time marker for the ion time-of-flight

$$t = (L/v) - (L/c), \quad (2.1)$$

where c is the speed of light. In most cases $c/v \gg 1$ such that the ion time-of-flight is $t \approx L/v$. Using Eq. (2.1), the ion velocity can be related to the charge collector time history. At a given time t , the collector current I_t can be related to the ion density n_i through the equation

$$I_t = \left[\sum_i (\gamma_i + Z_i) n_i \right] L/t \quad (2.2)$$

where Z_i is the charge state of the i_{th} ion species. Equation (2.2) is valid as long as the ion time-of-flight t and collector distance L remain respectively much larger than the characteristic time and dimensions of the ion source. For most laser produced-plasmas Eq. (2.1) is valid.

As can be seen from Eq. (2.2), a major drawback of a charge collector is that different ion species can be collected at the same time. An independent estimate of γ_i and $Z_i(t)$ is then required for more quantitative information about the ion velocity distribution.

2. Ion Analyzer

In the following sections, the ion analyzer design considerations and performances are addressed. In Section 2.1, the basic requirements for a high energy ion analyzer are described and our analyzer design is compared to others. In section 2.2, equations describing the particle dynamics within the analyzer and the analyzer resolution are derived. Space charge forces which could affect the analyzer resolution are also considered. Section 2.3 deals with the analyzer design and the ion detection system used for this instrument. Finally, in section 2.4, a new technique is described for the absolute calibration of the ion collection system used in the analyzer. This technique includes measurements of the secondary electron emission coefficients

for H^+ and C^{+Z} ions striking copper collectors at high energies.

2.1 Introduction

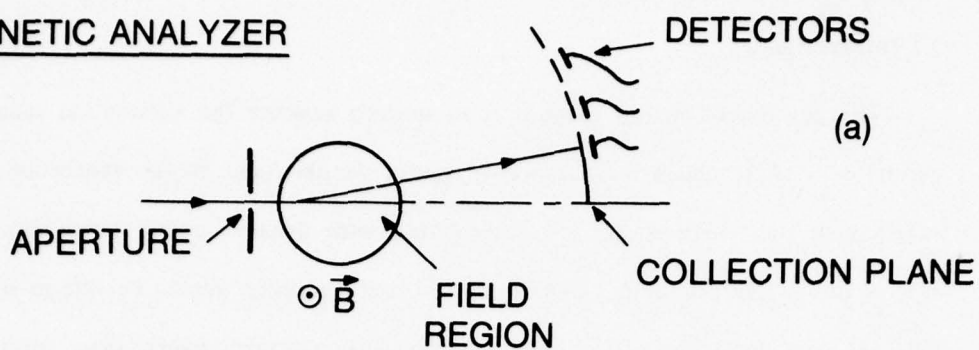
The purpose of an ion analyzer is to spatially separate the various ion species in the plasma blow-off to obtain their respective energy distributions. In our application, the basic requirement for a high energy ion analyzer is a wide dynamic energy range with moderate species and energy resolution. For example, a useful analyzer should be able to separate the different ionization stages of an aluminum target over a dynamic energy range from 1 to 1000 keV/Z. The energy range covered on a single shot should be at least around 10 to 1 and easily adjustable between shots. These requirements are quite restrictive for an ion analyzer. However, some general properties of our laser-produced plasma such as the short time duration and small size of the ion source can be taken advantage of in the analyzer design. The ion time-of-flight can be used to obtain the velocity and, therefore, energy of a known ion species. The small size of the ion source yields an almost radial expansion from the source. Focusing of the ion beam inside the analyzer is, therefore, not required for moderate energy and species resolution.

We first briefly describe three types of conventional ion analyzers which meet most of the requirements mentioned above. Next we show how our analyzer design evolved from some features borrowed from all three analyzers in order to meet the requirements of a practical high energy ion analyzer.

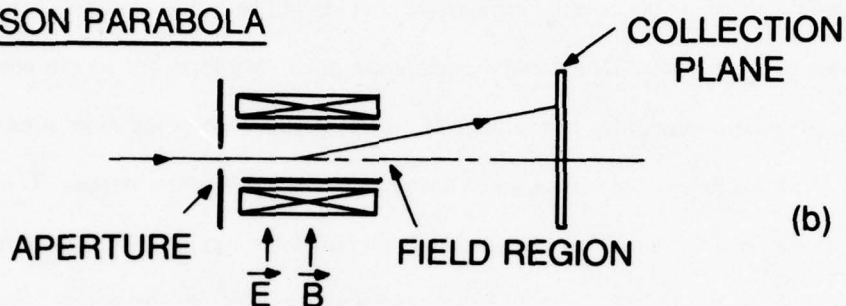
A magnetic analyzer⁷⁶⁻⁷⁸ suitable for high energy ion measurements is shown in Fig. 2.7a. This analyzer does not have any self-focusing properties and, therefore, uses both the finite size and time duration properties of the ion source. The uniform magnetic field can most easily be produced from permanent magnets. The magnet separation, however, limits the vertical cross section of the beam within the analyzer. Another drawback is that the analyzer energy range cannot be easily varied between shots.

A second conventional analyzer design is the Thomson parabola^{79, 80} (Fig. 2.7b). Each

MAGNETIC ANALYZER



THOMSON PARABOLA



45° ELECTROSTATIC ANALYZER

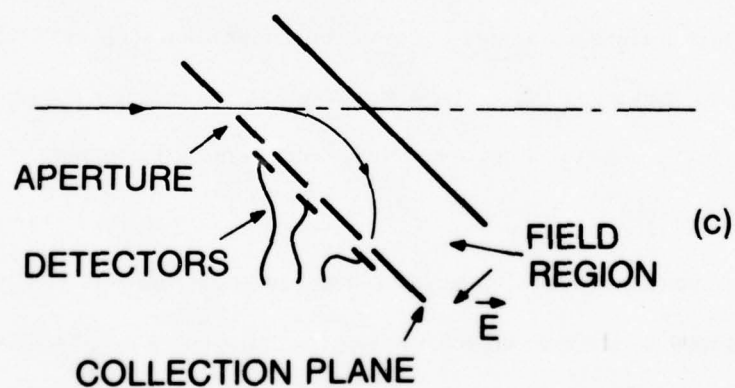


Fig. 2.7. Three conventional ion analyzers for laser-produced plasmas: (a) a magnetic analyzer; (b) the Thomson parabola; (c) a 45° electrostatic analyzer.

ion species, separated by the parallel electric and magnetic field, forms a parabola in the collection plane. Film (cellulose nitrate, for example) is usually used to record the ion parabolas. Tedious data reduction and film calibration are the major problems in obtaining quantitative ion energy distributions.

Conventional multi-channel electrostatic analyzers⁸¹⁻⁸³ currently used to diagnose laser-produced plasmas are of the parallel plate type (Fig. 2.7c). Ions both enter and leave the analyzer through the same plane. Several detectors can be accommodated simultaneously in the collection plane with good energy and species resolution due to the self-focusing of the ion beams inside the analyzer. However, for a given E/Z and voltage V between the plates, the ratio $(E/Z)/V$ is typically only around 2. High voltages are therefore required to deflect high energy ions and an upper energy limit is typically 100 keV/Z.

Our ion analyzer design combines some features from the three analyzers described above. In our analyzer configuration²⁶, the ions are first deflected by an electric field perpendicular to their incident velocity and finally collected by several detectors some distance away from the electric field region. The field of the magnetic analyzer is, in fact, replaced by a more easily adjustable electric field. Unlike the parallel-plate electrostatic analyzer, an $(E/Z)/V$ ratio around 50 is easily achievable, thereby extending the upper energy limit to a few MeV/Z. The short time duration properties of the ion source is used, in contrast with the Thomson parabola. The adjustable energy range and energy and species resolution are consistent with the requirements described above for an high energy ion analyzer. Both the design and construction of this system are simpler than most magnetic analyzers and the Thomson parabola. The analyzer could also be used in an electro-dynamic mode, if desired, by applying a voltage with a $1/t^2$ time dependence at the deflection plates⁸³.

2.2. Theory

2.2.1 Particle Dynamics

The schematic of the analyzer is shown in Fig. 2.8. The z -axis of the coordinate system is

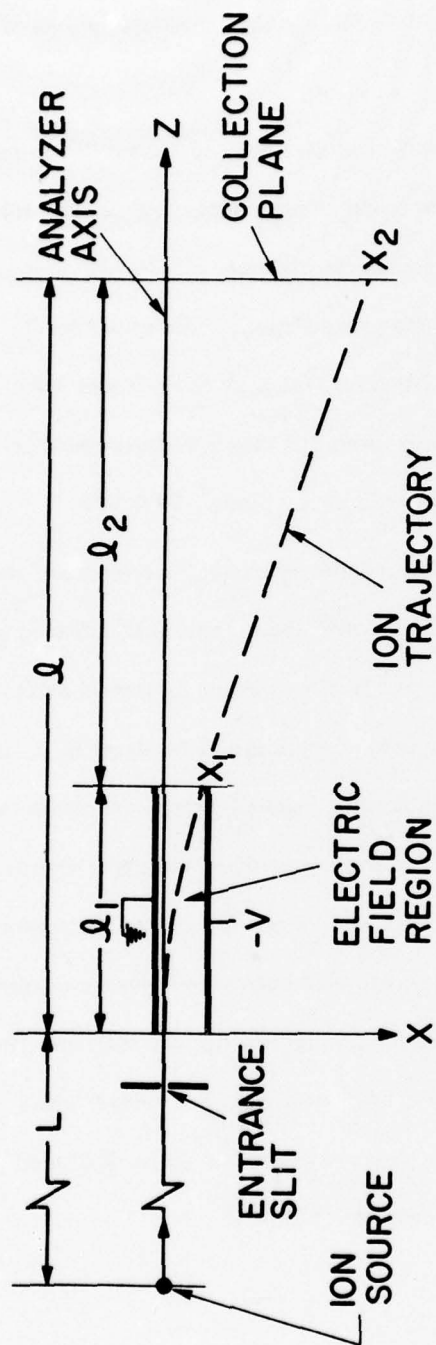


Fig. 2.8. Schematic of the high energy electrostatic analyzer.

between the center of the ion source and the entrance slit of the analyzer. The analyzing electric field is assumed uniform between the parallel plates and the ions are collected at $z = l = l_1 + l_2$ in a plane parallel to the electric field. For an ion of charge to mass ratio q/m having an initial velocity $\bar{v} = v_0 \bar{z}$ at $z = -L$ the equations of motion in the electric field region are, in the z direction

$$\ddot{z} = 0, \quad (2.3)$$

and in the x direction

$$\ddot{x} = \frac{q}{m} \frac{V}{d}, \quad (2.4)$$

where V is the potential between the plates separated by a distance d . Note that the ion motion along the initial direction is not affected by the applied field and therefore the time-of-flight to the detectors in the $z = l$ plane give the true initial velocity. Integrating Eqs. (2.3) and (2.4) and applying the initial conditions at $t = 0$, $z = x = \dot{x} = 0$, $\dot{z} = v_0$, we obtain at $z = l_1$,

$$\dot{x}_1 = \frac{q}{m} \frac{V}{d} \frac{l_1}{v_0}, \quad (2.5)$$

$$x_1 = \frac{1}{2} \frac{q}{m} \frac{V}{d} \frac{l_1^2}{v_0^2}. \quad (2.6)$$

The ions drift freely between this point and the detectors at $z = l$. Therefore, at $z = l$, the deflection from the z -axis is

$$x_2 = x_1 + \dot{x}_1 \frac{l_2}{v_0}.$$

Using Eqs. (2.5) and (2.6), this becomes

$$x_2 = \left(\frac{1}{2} l_1^2 + l_1 l_2 \right) \frac{q}{m} \frac{V}{d} \frac{1}{v_0^2}. \quad (2.7)$$

The time-of-flight of the ion from the source to detector is

$$t = \frac{L + l}{v_0}. \quad (2.8)$$

Equations (2.7) and (2.8) can be solved to yield the atomic mass to charge ratio A/Z of the ion,

$$\frac{A}{Z} = \frac{e}{m_p} \left(\frac{1}{2} l_1^2 + l_1 l_2 \right) \frac{V}{d} \frac{t^2}{(L + l)^2} \frac{1}{x_2}, \quad (2.9)$$

and the ion energy ($E = \frac{1}{2}mv_o^2$) per unit charge Z ,

$$\frac{E}{Z} = \frac{1}{2}e \left(\frac{1}{2}l_1^2 + l_1l_2 \right) \frac{V}{d} \frac{1}{x_2}, \quad (2.10)$$

in terms of the electron charge e and proton mass m_p . Therefore, to each point x_2 in the collection plane corresponds one and only one ion energy E/Z given by Eq. (2.10). As a function of time, the different ion species collected at this point x_2 can be identified using Eq. (2.9).

2.2.2 Energy and Species Resolution

The theoretical energy resolution of the analyzer is

$$\frac{\Delta E}{E} = \frac{\Delta x_2}{x_2}. \quad (2.11)$$

Likewise, the A/Z resolution is

$$\left(\frac{\Delta A/Z}{A/Z} \right)^2 = \left(\frac{2\Delta t_r}{t} \right)^2 + \left(\frac{2\Delta L}{L+l} \right)^2 + \left(\frac{\Delta x_2}{x_2} \right)^2. \quad (2.12)$$

Here, Δt_r can be taken to be the characteristic duration of the ion source, ΔL to be the characteristic length of the ion source and Δx_2 to be the finite dimension of the exit slit in the x direction. It is assumed that the initial thickness of the ion beam determined by the entrance slit plus the spread of the beam within the analyzer is less than the width of the corresponding exit slit. The spread of the beam could be due to poor beam collimation or space charge forces discussed in the next section.

Typical values of laser-produced plasmas of interest are $\Delta t_r \approx 10^{-10}$ sec, $t \approx 10^{-7}$ sec, $\Delta L \approx 10^{-2}$ cm, $L \approx 10^2$ cm and for the analyzer described in a later section $\Delta x_2/x_2 = 0.1$. Therefore, the main contribution to both the energy and species resolution is the finite dimension of the exit slits, i.e., the instrument resolution R_i is

$$R_i = \frac{\Delta A/Z}{A/Z} \approx \frac{\Delta E}{E} = \frac{\Delta x_2}{x_2}. \quad (2.13)$$

We will see in the next section that space charge forces acting on the ion beam within the analyzer can degrade the analyzer resolution if too small an exit slit is used. Space charge effects are most important at low ion energy. Therefore, in order to increase the dynamic

energy range at low energy, we chose the resolution R_i to be 10% for each slit in the analyzer described below. For application where space charge is not important a resolution of $R_i \approx 3\%$ could be easily achieved.

Any loss of energy or species resolution can also be observed experimentally. Using Eq. (2.9) for the A/Z resolution and $E = \frac{1}{2} m [(L + l)/t]^2$ for the energy resolution, the experimental resolution is given by

$$R_x = \frac{\Delta E}{E} = \frac{\Delta A/Z}{A/Z} = 2 \frac{\Delta t_x}{t}, \quad (2.14)$$

where now Δt_x is associated with the pulse width of each ion species recorded from oscilloscope traces. When R_x does not equal R_i , for a certain species at a given energy, a loss of resolution has occurred and quantitative information should not be expected from the measurements.

2.2.3 Space Charge Forces

We have considered only the dynamics of a single ion up to this point. The finite ion density effects within the analyzer are now addressed. The entrance slit width (slit dimension parallel to the deflecting electric field) of the analyzer must be less than the Debye length of the impinging plasma so that the electrons can be separated from the ions upon entering the analyzer. The initial thickness of an ion beam in the analyzer is then determined by the width of the entrance slit. For the case $l \ll L$, the geometrical divergence of the ion beam within the analyzer can be neglected. However, the space charge expansion of the ion beam due to the self-electric field of this non-neutral beam imposes some limitations on the analyzer parameters. The current density of the ion beam within the analyzer should be such that the beam expansion does not exceed the appropriate exit slit dimensions.⁸⁴

We consider a sheet beam of initial thickness d_o and initial current density j composed of a single ion species at an energy E/Z . From the paraxial ray equation, the width d_2 of the ion beam, after traveling a distance l , is given by⁸⁵

$$\frac{d_2}{d_o} - 1 = \frac{e m_p}{2^{5/2} \epsilon_o} j l^2 \left(\frac{E}{Z} \right)^{-3/2} \left(\frac{A}{Z} \right)^{1/2}, \quad (2.15)$$

where E/Z and A/Z are respectively the energy and atomic mass divided by the charge state of the ions. Therefore, if an ion beam defined by the entrance slit width d_o of the analyzer is to pass entirely through its related exit aperture of width d_2 , the following inequality must be satisfied

$$j \leq \frac{2^{5/2} \epsilon_o}{e m_p^{1/2}} \left(\frac{d_2}{d_o} - 1 \right) \frac{1}{l^2} \left(\frac{E}{Z} \right)^{3/2} \left(\frac{Z}{A} \right)^{1/2} \quad (2.16)$$

With too large an entrance slit or a current density, the output current at the exit slit saturates. The input and output ion currents lose proportionality and the instrument resolution is degraded.

Equation (2.16) can also be generalized to the case of several ion species all present at the entrance slit at the same time with the same velocity $v_o (E = \frac{1}{2} Z m_p v_o^2)$. In this case, the initial current density j in Eq. (2.16) becomes the sum of partial beams with current density j_i associated with each ion species. Here, we assume that the spread of each individual beam is due to the sum of the partial beam currents since the total entering current density is present over a fraction of the distance l . Therefore, if one of the partial beams is to pass entirely through its related exit slit of width d_2 , the following inequality must be satisfied

$$\sum_i \left(\frac{Z}{A} \right)_i j_i \leq \frac{2 \epsilon_o m_p}{e} \left(\frac{d_2}{d_o} - 1 \right) \frac{1}{l^2} v_o^3. \quad (2.17)$$

Since most of the transverse impulse is given to the ions within a short distance beyond the entrance slit, Eq. (2.17) is preferable to considering completely separated partial beams within the analyzer. Equation (2.17) is, therefore, an underestimate of the maximum current densities allowed in the analyzer.

The spread in the height (slit dimension perpendicular to the deflecting electric field) of the ion beam within the analyzer is most conveniently estimated by following the diameter of a circular ion beam whose diameter is equal to the rectangular beam height. In this case, if a single species ion beam defined by the entrance slit height h_o is to pass entirely through the exit slit of height h_2 , the current density must satisfy⁸⁵

$$j \leq \frac{2^{5/2} \epsilon_0}{e m_p} \left(\frac{h_2}{h_0} \right)^2 \frac{1}{l^2} \left(\frac{E}{Z} \right)^{3/2} \left(\frac{A}{Z} \right)^{1/2} V \left(\frac{h_2}{h_0} \right), \quad (2.18)$$

where

$$V \left(\frac{h_2}{h_0} \right) = 2 \left[\frac{h_0}{h_2} \int_0^R \exp(u^2) du \right]^2,$$

$$R^2 = \log \frac{h_2}{h_0}.$$

The quantity $V(h_2/h_0)$ can be evaluated numerically for different ratios h_2/h_0 . It is to be noted that, contrary to the beam width case, if the ion beam height does not satisfy Eq. (2.18) the input and output total current would still lose proportionality but the instrument resolution would not be necessarily affected.

The expansion of a circular beam due to space charge effects can be compared to that for a sheet beam, using Eq. (2.18) and (2.16). For the analyzer parameters listed in the next section, a cylindrical beam always expands less than a sheet beam. Therefore, Eq. (2.16) which describes a sheet beam expansion can also be used as an overestimate for a circular beam expansion. Because of its simplicity, Eq. (2.17) for a sheet beam will then be used for future estimates of the maximum current density compatible with both the width and the height of an exit slit.

Measurements of the analyzer resolution [using Eq. (2.19)] can be made to verify whether Eq. (2.17) was indeed satisfied for the ion beam width. The height h_0 of the entrance slit should then be selected small enough such that any loss of proportionality between the input and output current would first be due to the entrance slit width (not the slit height) and result in a loss of instrument resolution. Some examples of maximum output voltages into 50 Ω from an ion detector are given in the next section.

2.3 Analyzer Design and Operation

In this section we discuss the general properties of the electrostatic ion analyzer geometry and its ion detection system. A modified version of the analyzer, which was used for the measurement of secondary electron emission coefficients, will be described in Section 2.4.

2.3.1. Design Considerations

Figure 2.9 shows the design of the analyzer and its location with respect of the target chamber. A bellow-flange combination at the target chamber allows the angle between the analyzer axis and the laser axis to be chosen between 35° and 55° . The distance between the analyzer and the target can be altered by changing the length of the flight tube between the bellow and the gate valve. The one inch diameter copper tube inside the flight tube serves two purposes. First, it acts as a waveguide beyond cutoff ($< 1 \text{ GHz}$) to reduce the low frequency electromagnetic noise propagating into the analyzer chamber and the ion detectors. Next, it makes differential pumping between the two chambers possible by restricting the aperture of the flight tube. The gate valve in front of the analyzer chamber is used to completely isolate the analyzer vacuum chamber from the target chamber when one of the chambers has to be let up to atmospheric pressure. The vacuum system of the analyzer consists of a 150 L/sec diffusion pump with a nitrogen cold trap. An additional cold trap can also be used inside the analyzer chamber to lower the base pressure from 5×10^{-6} Torr to a few times 10^{-7} Torr when necessary.

Figure 2.10 shows the details of the analyzer that was used for the measurements of most of the high energy ion distributions presented in this report. This analyzer was designed to separate ion species of energies from 5 keV to 1000 keV per unit charge with a 10% energy and species resolution. To achieve a wide energy range several E/Z channels were placed in the collection plane. Thus a rather long distance between the deflecting plates and the collection plane (30 cm) was required.

The electric field between the deflection plates is related to the voltage V and plate separation d by V/d . With the plate length and height to separation ratio of 4.35, nonuniformity of the field due to end effects can be neglected. With $l_1 = 10$ cm, $l_2 = 30$ cm and $d = 2.3$ cm, we get from Eq. (2.10) a relation between the ion energy per unit charge, the plate voltage and the exit slit location,

$$\frac{E}{Z} = 83.6 \frac{V}{x_2}. \quad (2.19)$$

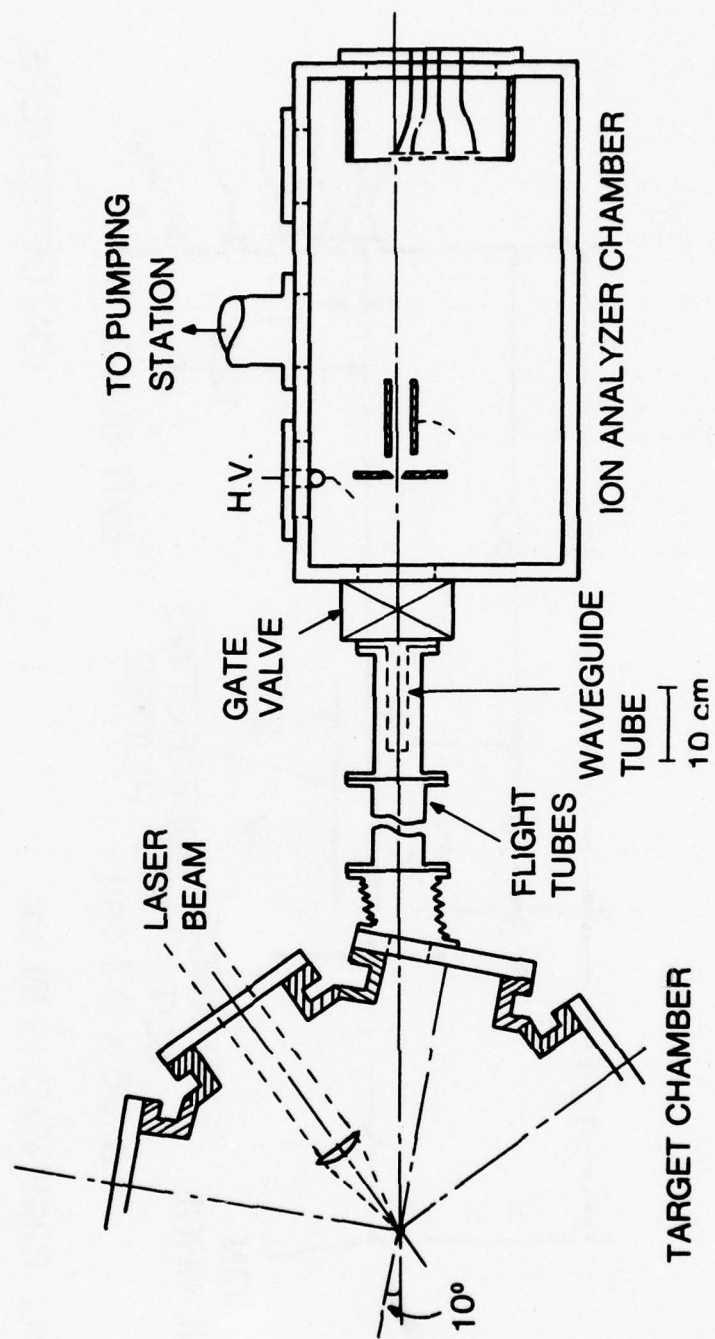


Fig. 2.9. Some design details and the location of the analyzer with respect to the target chamber.

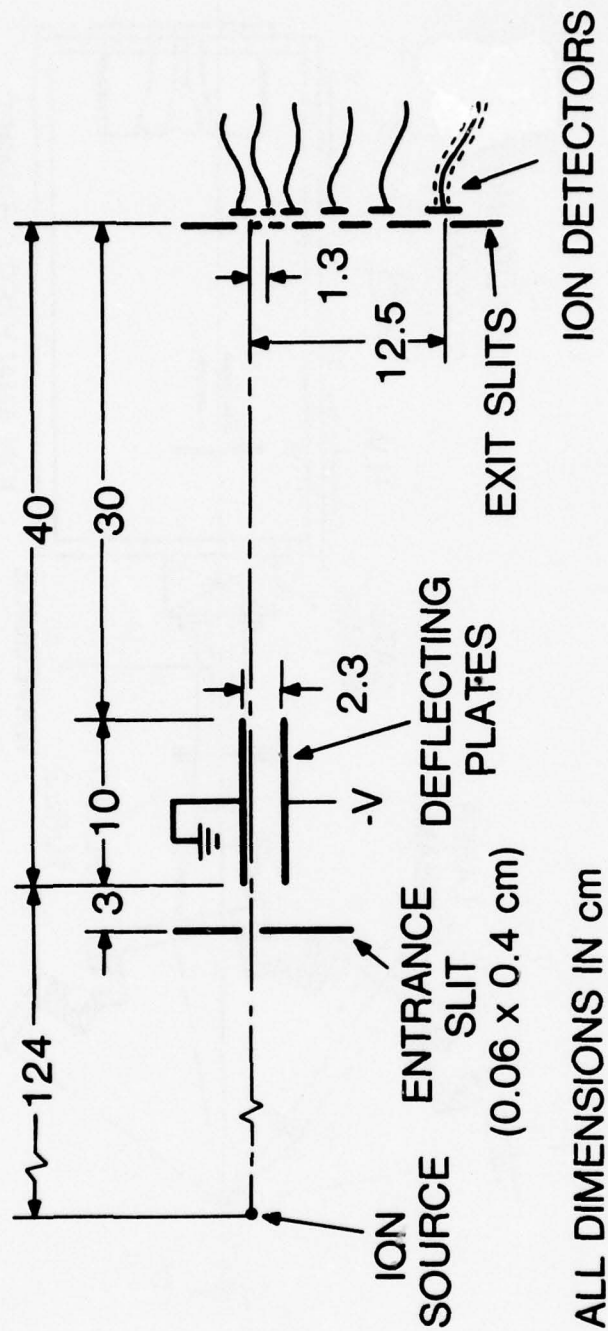


Fig. 2.10. Dimensions of the time-of-flight electrostatic high-energy ion analyzer. This analyzer can be used up to ~ 1.5 MeV/Z with an energy range per shot of 9.6 to 1 and an energy and species resolution of 10%.

For the most energetic channel ($x_2 = 1.30$ cm), the $(E/Z)/V$ ratio is then 64.3. A 15 kV power supply is therefore sufficient to study ions with energies up to 1 MeV/Z. The upper limit on E/Z with this analyzer is probably around 1.5 MeV/Z. Above this energy, the combination of high current densities (from the low energy ions) and high electric field (~ 10 kV/cm) could cause a voltage breakdown between the plates.

The analyzer was designed such that the entrance slit and the exit slit-ion detector system can be changed without tedious alignment. This allows for using a slit arrangement that gives better resolution or a higher signal level when space charge effects are of no concern. The entrance slit used in most experiments is 0.4 cm high by 0.06 cm wide. In the collection plane, twelve exit slits are provided for charge detection, and an additional slit at $x_2 = 0$ is used for neutral particle detection. Table 2.1 shows the distance from the analyzer axis, the relative energy and the height of each of the 12 exit slits used for ion detection. With the centers of the first and last slits at respectively 1.30 and 12.50 cm from the analyzer axis, the E/Z range per shot is 9.6 to 1. The aspect ratio for each of the 12 slits is $d_2/x_2 = \Delta x_2/x_2 = 0.1$. According to Eq. (2.13), this limits the energy and species resolution to 10%. The height of a given exit slit is chosen large enough that the slit width is the limiting parameter on the maximum current allowed in the analyzer due to space charge forces [Eq. (2.17)]. Excessive ion beam expansion due to space charge effects can therefore be identified by a loss of instrument resolution using Eq. (2.14).

2.3.2. Ion Detection System

The ion detector used behind each slit is a planar copper electrode etched onto a printed circuit board. Each detector is connected by a 50 Ω coaxial cable to a biasing circuit, similar to Fig. 2.6a, used to repel secondary electrons. The signal of the neutral detector is due entirely to the secondary electrons emitted from the collector. The output signal from each channel is amplified by 35 dB using 3 cascaded chip amplifiers from Avantek's GPD series. A schematic of the amplifier circuit is shown in Fig. 2.11. Each circuit is mounted on a 50 Ω strip line and protected against electromagnetic interference by a shielded box. Typical input noise level is

TABLE 2.1

Distance from the analyzer axis, relative energy and height of the 12 exit slits for the ion analyzer shown in Fig. 2.10.

Slit number	Slit location x_2 (cm)	Relative energy	Slit height (cm)
01	01.30	1.0	1.0
02	01.63	0.80	1.4
03	01.96	0.66	1.7
04	02.36	0.55	2.0
05	02.84	0.46	2.5
06	03.42	0.38	3.0
07	04.13	0.31	4.0
08	05.04	0.26	5.0
09	06.22	0.21	6.0
10	07.78	0.17	8.0
11	09.83	0.13	8.0
12	12.50	0.10	8.0

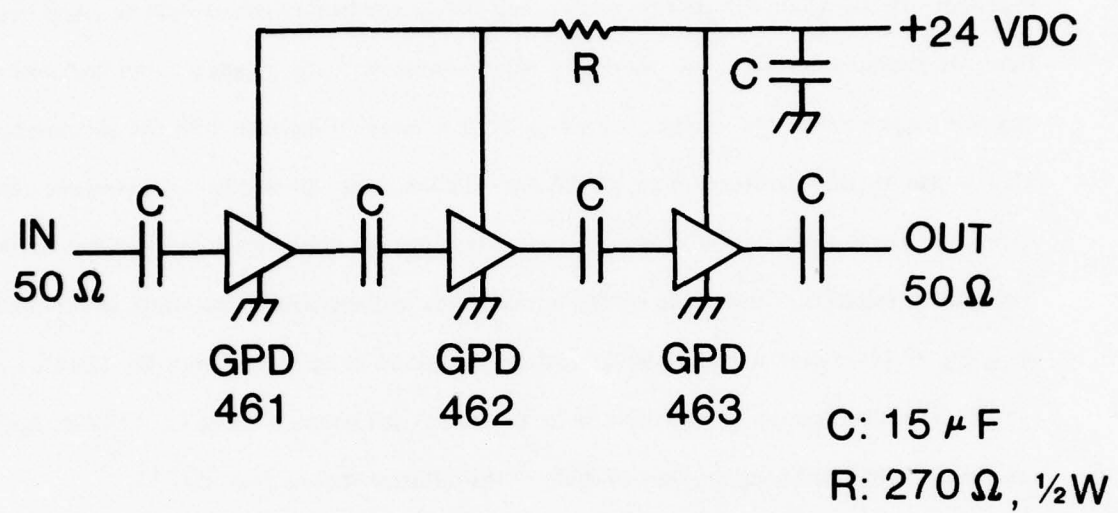


Fig. 2.11. Schematic of the broad bandwidth amplifier circuit.

around $15 \mu\text{V}$ with a frequency response between 10 kHz and 400 MHz. The output of each analyzer channel is finally connected to a 50Ω load and time-resolved by a fast oscilloscope. The arrangement cable-amplifier-oscilloscope is verified to have an adequate rise-fall time, required by Eq. (2.14) for each E/Z channel.

Typical oscilloscope trace outputs from three different E/Z channels recorded on the same shot are shown in Fig. 2.12. The 340, 130, and 44.5 keV/Z energy channels correspond respectively to slit numbers 1, 6 and 11. In this case, the target material was CD_2 with some traces of hydrogen. Details about the shot parameters and the data reduction process will be given later. Here, we simply point out some interesting details about the output signals. One first notices that the output pulses are squared, an effect which is seen to increase with the slit number. This is due to the increasing ratio of the exit and entrance slit widths. A reference time $t_0 = (L + l)/c$ is given by the onset of the electromagnetic noise which is produced by the laser-plasma interaction, picked up by the ion detectors and amplified. The width of the peaks using Eq. (2.14), yields an experimental analyzer resolution in agreement with Eq. (2.13), i.e., $\sim 10\%$. The identification of each peak as to ion species can be made using Eq. (2.9) or, more conveniently, by comparing the time-of-flight of the different species ($t \propto \sqrt{A/Z}$).

The minimum detectable signal level is limited by the amplifier's noise level, i.e., about $15 \mu\text{V}$. At the other end, ion beam blow-up due to space charge effects determines the maximum detectable current without resolution losses. Using Eq. (2.16) and the entrance slit cross section, the maximum output voltage into 50Ω from a detector is given by,

$$V_{\text{omax}}(\text{mV}) = 0.010 \left[\frac{d_2}{.082} - 1 \right] \left[\frac{E}{Z} \right]^{3/2} \left[\frac{Z}{A} \right]^{1/2}, \quad (2.20)$$

where d_2 is in mm and E in keV. If more than one ion species is present, Eq. (2.17) should be used instead of Eq. (2.16). For simplicity, the emission of secondary electrons was neglected in Eq. (2.20). Taking into account a secondary electron coefficient, as in Eq. (2.2), would typically increase V_{omax} by a factor 2 to 5 depending of the ion species and energy. Geometrical expansion of the ion beam within the analyzer was taken into account in Eq. (2.20) by multi-

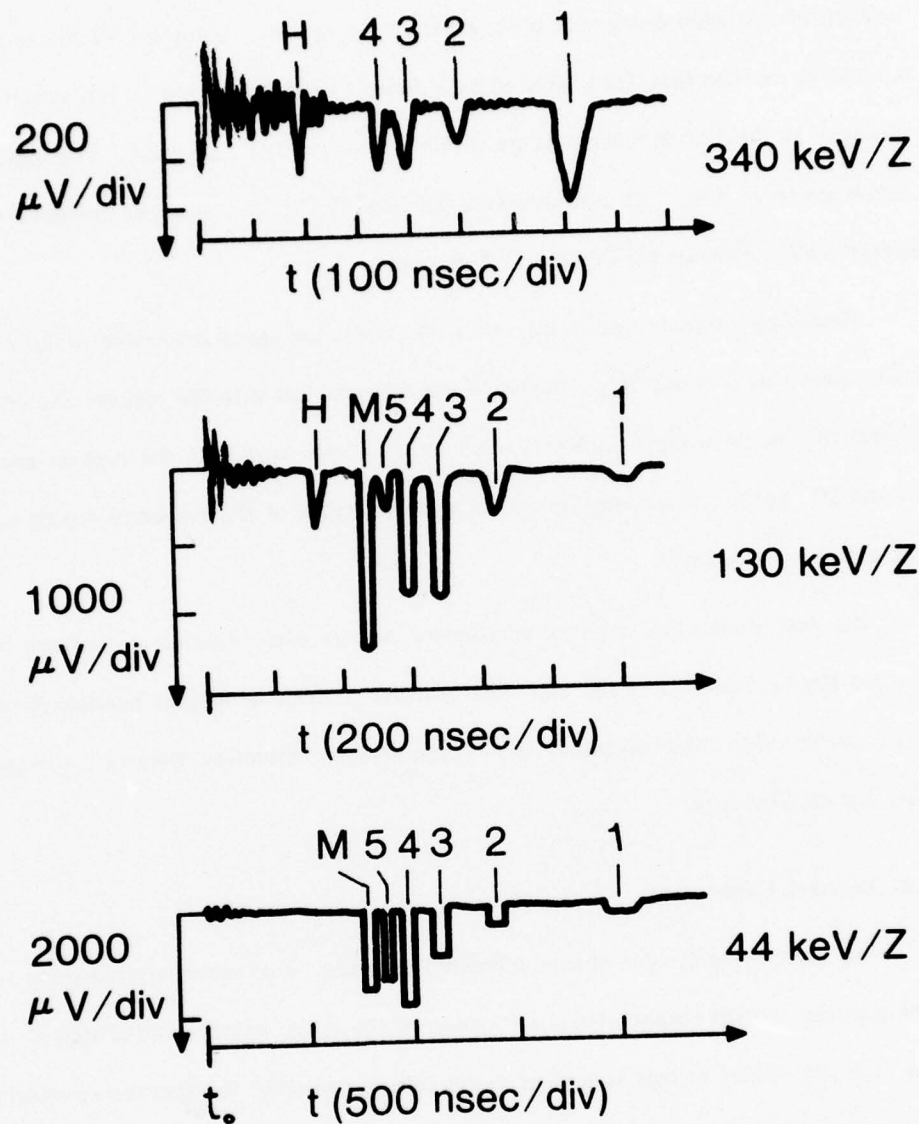


Fig. 2.12. Typical oscilloscope traces from three different E/Z channels recorded on the same shot. The target material is CD_2 with some traces of hydrogen. The numbers represent C^{+z} charge species, H the H^+ ions and M a mixture of C^{+6} and D^+ ions.

plying the entrance slit width by the factor $(L + l)/l$ (see Fig. 2.8).

The output voltage limitation for the highest E/Z detector is plotted in Fig. 2.13 as a function of the beam energy for three different ion species. Using Eq. (2.20) and Table 2.1, it can also be verified that, for a fixed voltage across the deflecting plates, the output voltage limitations of all the analyzer channels are within a factor of 2 of each other. The maximum output signals given in Fig. 2.13 can therefore be used for all the analyzer channels provided the energy scale represents the highest E/Z channel.

Requiring a signal-to-noise ratio of 5, the minimum signal detectable is $75\mu\text{V}$ in Fig. 2.13. This shows that it is not very practical to use this analyzer with the highest E/Z channel below 20 keV/Z . In most cases, however, this analyzer was used with the highest energy channel around 200 keV/Z , extending the output dynamic range of the detection system up to at least two orders of magnitude.

For our plasma and analyzer parameters, a convenient distance L between the entrance slit and the ion source was 121 cm . This distance is made as long as possible since it reduces space charge effects and increases the ion time-of-flight, therefore relaxing the requirement for very fast oscilloscopes.

2.4. Detector Calibration

For each ion striking a charge collector, a number γ of secondary electrons are emitted. The number of such secondaries is a function of the mass, velocity and charge of the incident ion. Usually, a bias voltage is applied to the collector in order to repel the secondary electrons to the electrical ground. Subtraction of the secondary electron emission from the ion signal is therefore required if an absolute ion energy distribution is to be deduced from the data obtained with the ion analyzer.

We first review briefly what is presently known about the properties of secondary electron emission. Next a new experimental technique is described which allows the measurement of relevant secondary electron coefficients from any given metallic collector surface. This tech-

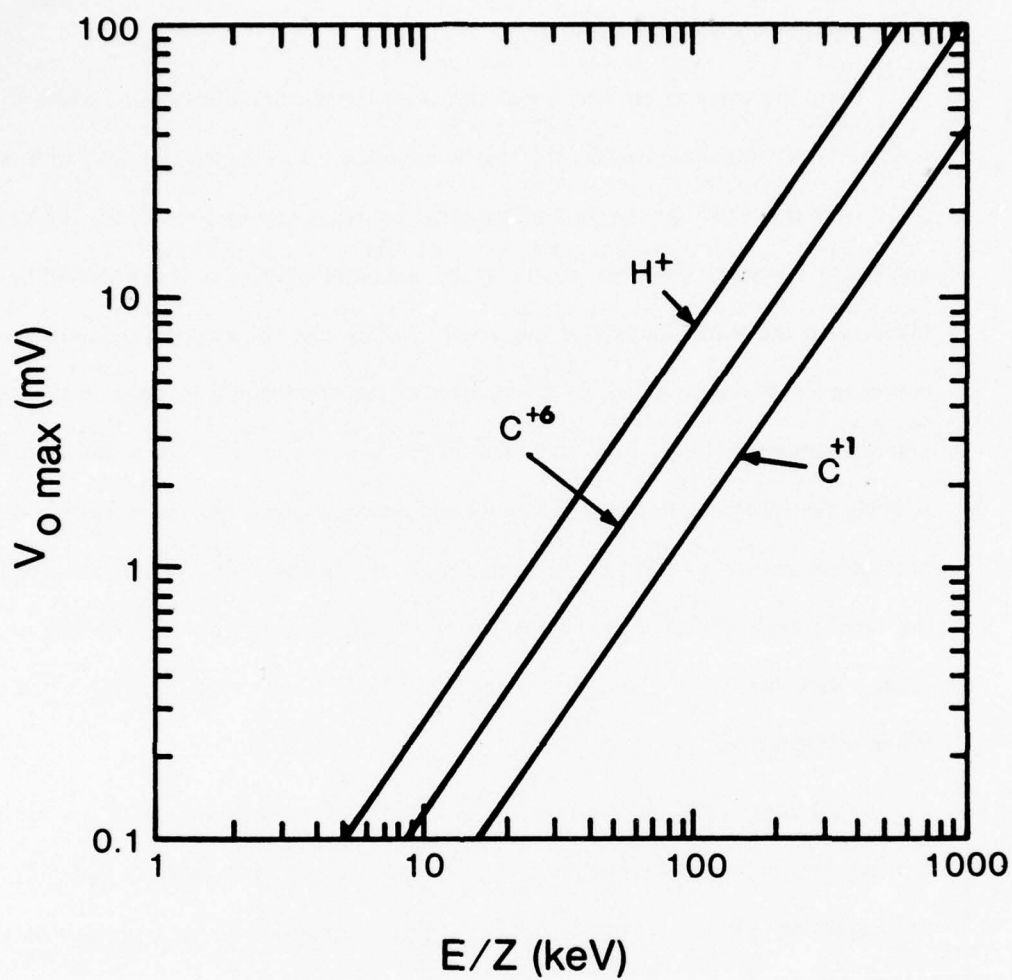


Fig. 2.13. Output voltage limitations into 50Ω due to space charge forces versus ion energy.

nique is specially well adapted for our high energy ion analyzer. Finally, the secondary electron coefficients for carbon and hydrogen ions incident on copper surfaces are given as a function of incident ion energy.

2.4.1. Secondary Electron Ejection

There are two mechanisms which can cause the ejection of electrons when particles strike solid surfaces: the potential and the kinetic emission. An extensive review, with references, is given by Kaminsky⁸⁶ for the case of potential emission and by Krebs⁸⁷ for the case of kinetic emission. Potential emission occurs if the potential energy of the bombarding particles is higher than the work function of the metal. In this case the electron ejection is exclusively a consequence of the potential energy transfer of the bombarding particles to the metal. Thus, potential emission should be independent of the kinetic energy of the bombarding particles but strongly dependent of the charge state of the incident ions. The other mechanism which can produce an ejection of electrons is kinetic emission. In this case a part of the kinetic energy of the bombarding particle is transferred to target electrons (of which a fraction can leave the solid). By definition, the kinetic emission should therefore be independent of the charge state of the incident ions.

In the case of high energy ions ($> 10 \text{ keV/Z}$), the contribution to the secondary electrons emitted due to potential emission becomes small relative to the kinetic emission mechanism. The secondary electron coefficient γ is, therefore, expected to be fairly independent of the charge state of the incident ions in the high energy range of interest. The atomic mass of the impinging ion at a given energy is, however, expected to affect γ since the ion penetration depth into the material is mass dependent.

A parameter which can strongly affect the secondary coefficient γ is the cleanliness of the charge collector surface. It has been shown experimentally⁸⁸ that "gassy" collector surfaces can produce up to 5 times more secondary electrons than atomically clean surfaces. Measurements of γ for a specific collector surface should therefore be extrapolated to other collectors only if the experimental conditions and collector material are similar to the calibrated collector.

Measurement of γ for energetic H^+ ions incident on copper collectors with different surface conditions have been reported in ref. 88. Similar measurements for carbon ions were not found in the literature. Because of the unpredictability of γ due to the collector surface preparation and the unavailability of measurements for carbon ions, a technique was developed to directly measure the secondary coefficients from the collectors in the ion analyzer. The technique and measurements of γ are presented in the following sections.

2.4.2. Experimental Technique

Most measurements of secondary electron coefficients presented in the literature have been done with a similar experimental arrangement to that shown schematically in Fig. 2.14a. In all cases, a single-species monoenergetic ion beam is assumed to be incident on the entrance aperture. The collector current I_c is due to both the incident ions and emitted secondary electrons, whereas, the tube current, I_e , is due to the collected secondary electrons only. In order to make sure that the secondary electrons produced from the edge of the entrance aperture cannot be collected by the tube, a suppressor with a high negative bias voltage is used between the entrance aperture and the tube. The secondary electron coefficient γ is related to the ratio I_c/I_e by the equation

$$\gamma = Z \left(\frac{I_c}{I_e} - 1 \right)^{-1}, \quad (2.21)$$

where Z is the charge of the incident ion. For the case of energetic ions incident on gassy collector surfaces, we have $\gamma > z$ and therefore $I_c/I_e \sim 1$. A small uncertainty in I_c or I_e can therefore lead to a large error in the determination of γ .

In order to facilitate and improve the accuracy of the measurement, the technique shown in Fig. 2.14b was developed. A uniform density ion beam is again assumed to be incident on the entrance aperture. One tube is biased positively in order to attract secondary electron while the other tube is biased negatively to repel secondary electrons back to the ion collector. The collector current I_i associated with the negatively biased tube is therefore due solely to the ion current. The secondary electron coefficient γ is then given by

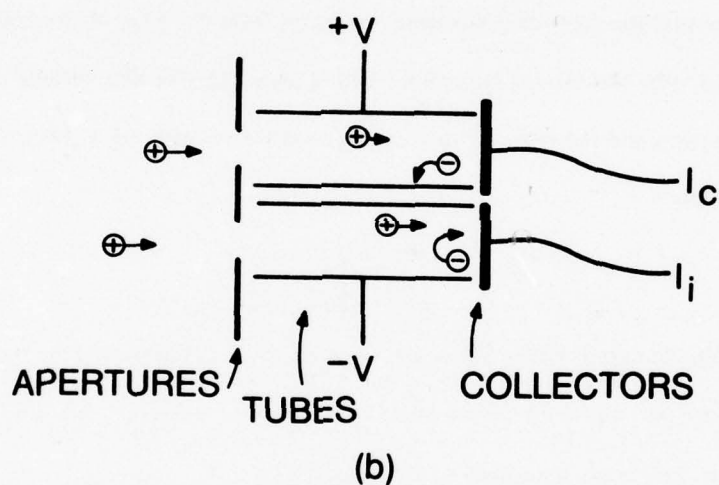
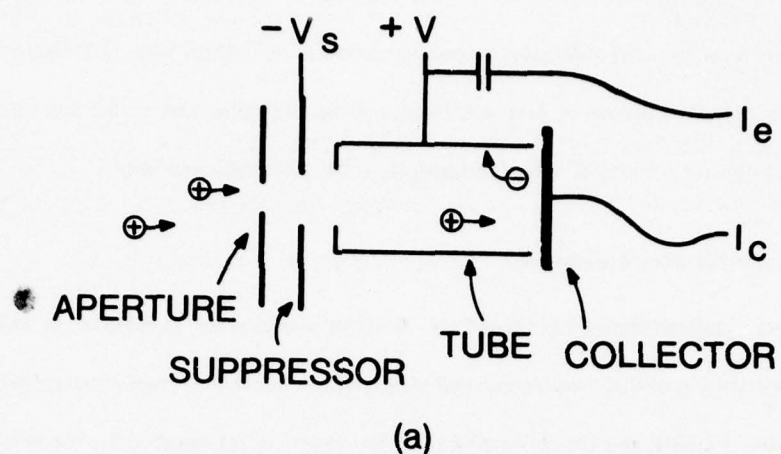


Fig. 2.14. Schematic of experimental arrangement for the measurement of secondary electron coefficients. The arrangement of (b) becomes more accurate than the one in (a) when $\gamma > Z$.

$$\gamma = Z \left(\frac{I_c}{I_i} - 1 \right) \quad (2.22)$$

For $\gamma > Z$, the subtraction error of large comparable numbers can be avoided in Eq. (2.22) since $I_c \gg I_i$. For high energy ions incident on gassy collector surfaces, this technique is therefore preferred.

In principle, the biased tubes in Fig. 2.14b could be replaced by properly biased highly transparent fine meshes. In practice, however, a negatively biased mesh, due to its finite cross section, can itself produce secondary electrons which can be accelerated back to the ion collector and contribute to the ion current. The advantage of the tubular electrode is to supply the suppression potential *without* physically intercepting the ions. This technique of using a negatively biased tube in front of a particle collector was previously used in the design of an electrostatic electron analyzer⁸⁹ and an ion charge collector.⁹⁰ Both applications have been extensively described elsewhere and are shown schematically in Fig. 2.15a and b. In the ion charge collector case (Fig. 2.15b), the negatively biased tube is used to repel the secondary electrons back to the collector. Because of the relatively long distance between the entrance aperture and the collector plane, this charge collector design is more sensitive to space charge problems than the conventional biased charge collector described in a previous section. The tube collector must therefore be used further away from the target, forcing a compromise between a good signal-to-noise ratio and a wide dynamic range of the detector output.

Two other popular charge collector designs incorporating some degree of secondary electron suppression are shown in Fig. 2.15b and c. The Faraday cup (Fig. 2.15c) offers excellent secondary electron suppression⁹¹ but has a very small acceptance angle. At the other end, the double-grid collector (Fig. 2.15d) has a large acceptance angle but suffers from secondary electron emission from the negatively biased grid. The tube collector (Fig. 2.15b) is therefore a good compromise between the two, since it offers excellent secondary electron suppression with a reasonable acceptance angle.

It was mentioned above that the ion beam incident on the collector arrangement shown in Fig. 2.14b should be monoenergetic, uniform and contain a single ion species. An excellent ion

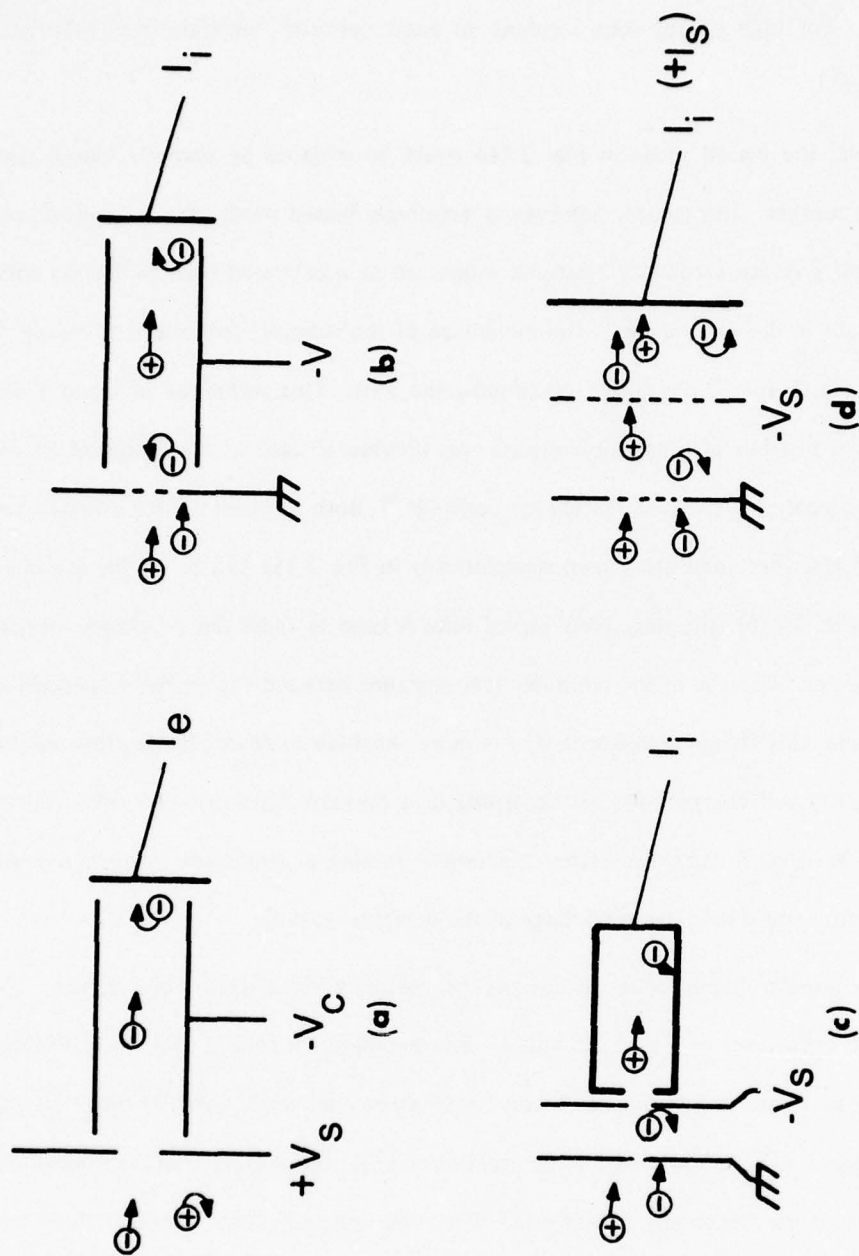


Fig. 2.15. (a) Electrostatic electron analyzer. (b) Ion charge collector using a negatively biased tube to suppress secondary electrons. (c) Faraday cup ion collector. (d) Double-grid ion collector.

source which can meet these requirements is the laser-produced plasma itself coupled with the high energy ion analyzer as an ion species and energy filter. The experimental arrangement is shown schematically in Fig. 2.16a and b. The ion analyzer is the same as the one described in Section 2.3., except that the distance between the deflection plates and the collection plane has been reduced to 6 cm. The beam expansion due to space charge forces is therefore highly reduced and a larger entrance slit can be used.

The exit slit arrangement is shown in Fig. 2.16b. Only two E/Z channels were used on each shot, both with an energy and species resolution of 10%. Each E/Z channel consists of two exit slits with a tube followed by a collector behind each slit. The cross section of each rectangular tube is at least twice that of the corresponding slit and the tube width to length ratio is typically 2.5 to 1. The upper and lower tube of each E/Z channel are usually biased at +300V and -300V respectively. Each collector, mounted individually behind the tubes, is connected to a wide-band amplifier and is time-resolved with a fast oscilloscope.

The use of Eq. (2.22) to obtain secondary coefficients assumes that the incident ion current is the same for both slits at a particular E/Z . This assumption was verified experimentally by comparing the output signals from the collectors associated with the two slits at the same E/Z . The two collector signals, with the same bias voltage on their tube, were found to be equal on the average, with a deviation of up to $\pm 10\%$ from shot-to-shot. This means that the entrance slit height is well aligned with respect to the exit slit arrangement, and that the plasma density over the entrance slit height is uniform to within 10%. This plasma nonuniformity on the entrance slit is mostly observed at high target irradiance and is responsible for some of the data scatter observed during the measurement of the secondary electron coefficients.

2.4.3. Secondary Electron Coefficient Measurement

The collectors used for the measurements of γ are made of copper etched on printed circuit boards and are very similar to those used for the 12 channel analyzer (they were in fact etched at the same time and processed the same manner). Since the collector surfaces are only

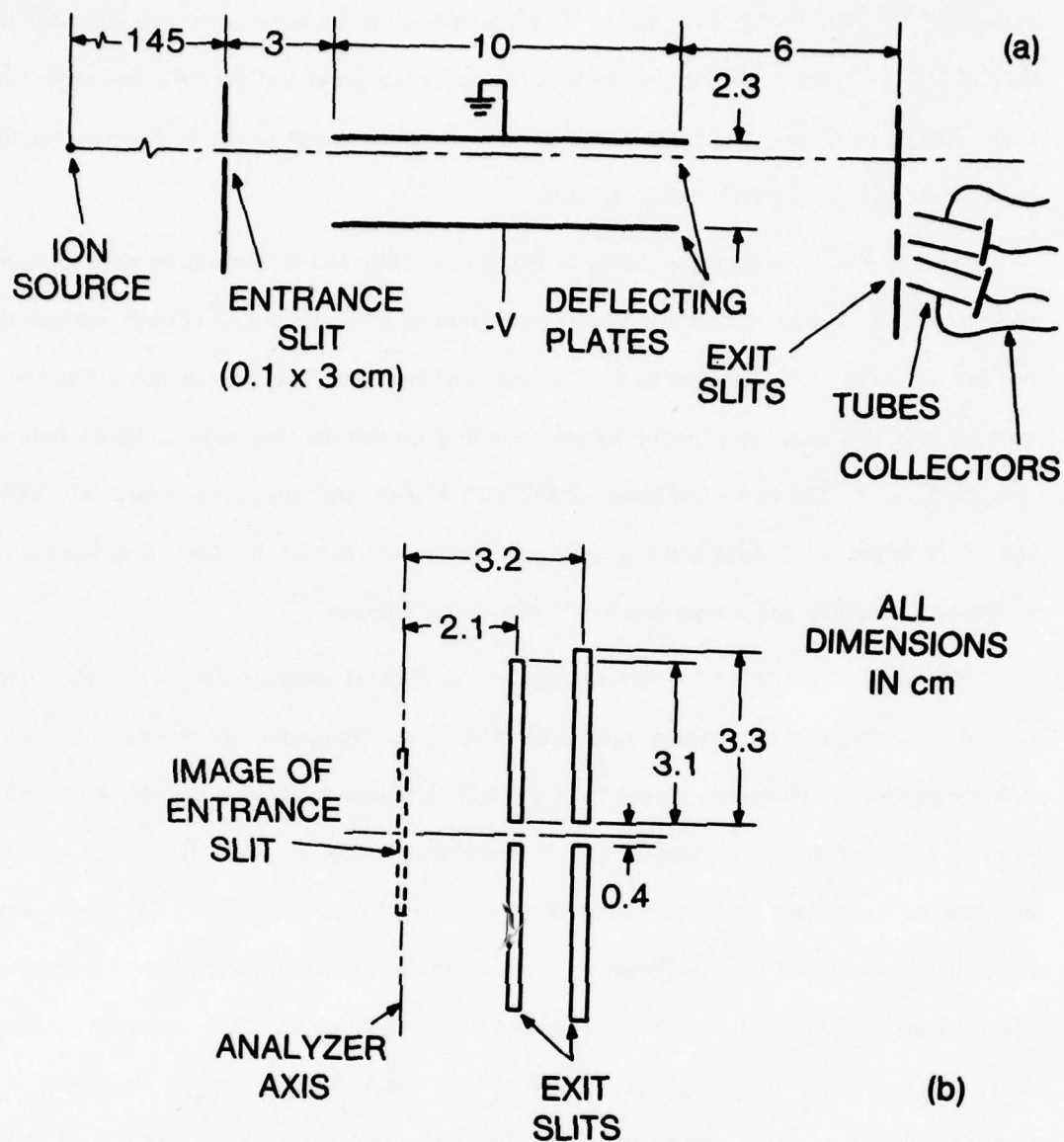


Fig. 2.16. (a) Ion analyzer used as an ion species and energy filter for the measurement of secondary electron emission coefficients. Each E/Z channel consists of two exit slits with a tube followed by a collector behind each slit. (b) Exit slit arrangement.

simply cleaned with acetone at room temperature before being mounted, they can, therefore, be categorized as "gassy" surfaces, in contrast with "atomically cleaned" surfaces.

The secondary electron emission coefficients for C^{+6} and H^+ ions incident on the copper collectors are shown in Fig. 2.17 as a function of ion energies. The curves are simply smooth fits through the points. Each point and its associated standard deviation represents an average of 5 measurements of γ using Eq. (2.22). As mentioned in the previous section, the scatter in the data points is mostly due to some nonuniformity of the ion current incident on the two collectors at the same E/Z . For the H^+ results in Fig. 2.17, the secondary coefficient γ for our gassy surfaces is typically three times higher than those reported for atomically cleaned surfaces.⁸⁸

Figure 2.18 shows the influence of the charge state of the incident carbon ions on the secondary coefficient using our copper collectors. Each point is an average of 5 data points with a typical standard deviation of $\pm 10\%$ (not shown in Fig. 2.18). One notices that the difference $\Delta\gamma = \gamma(C^{z+}) - \gamma(C^{(z-1)+})$ is nearly independent of the kinetic energy of the ions. This is not surprising since the difference $\Delta\gamma$ is due to secondary electrons emitted by the potential emission mechanism discussed in section 2.4.1. Since the incident ion kinetic energy is much higher than the ion potential energy, the kinetic emission mechanism dominates the potential emission. For energetic carbon ions (> 100 keV), the secondary electron coefficient γ is, therefore, fairly independent of the charge state of the incident ions, as predicted in Section 2.4.1.

b) Methods

In the previous section, we described in detail the instrumentation developed to measure the ion expansion. We now address the analysis of the data to obtain useful information such as the ion energy distributions, with the experimental apparatus. In the first section, we discuss the use and qualitative information that can be obtained from charge collectors. Most quantitative information about the plasma expansion can, however, only be obtained with the ion analyzer. We therefore discussed in detail, in Section 2, the data reduction process that yields ion energy distributions from the analyzer data.

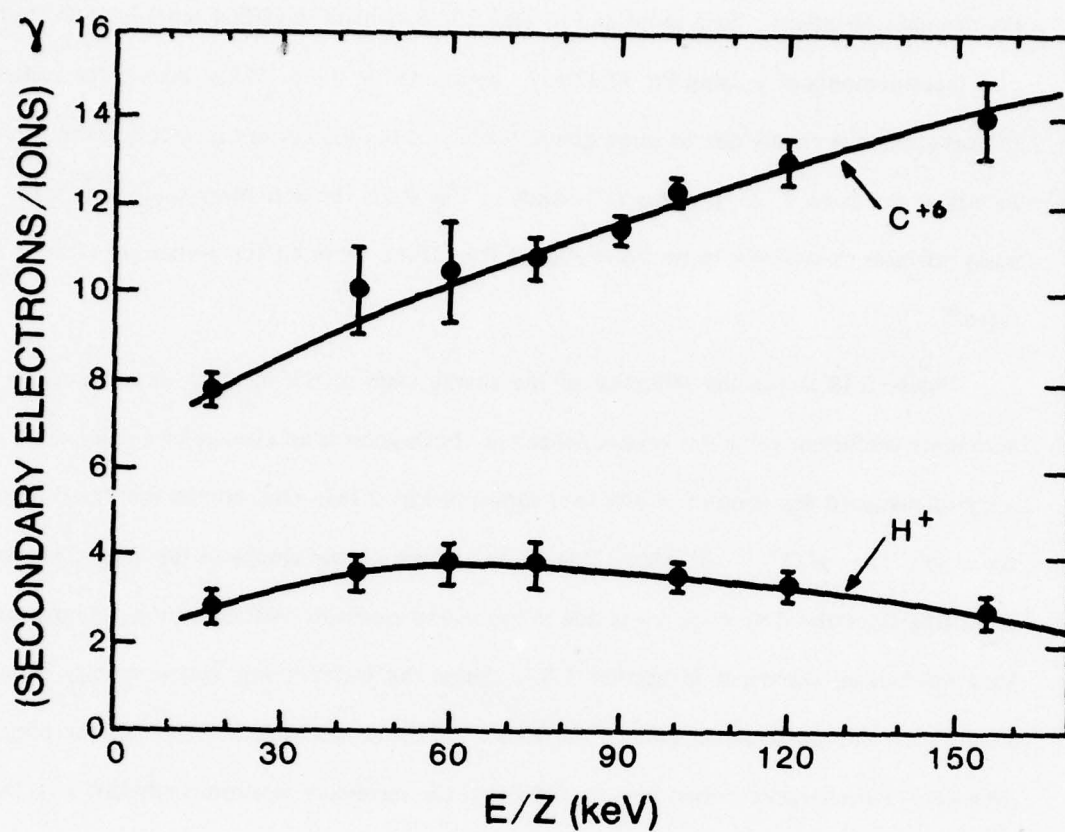


Fig. 2.17. Secondary electron emission coefficients for C^{+6} and H^+ ions incident on "gassy" copper surfaces as a function of ion energy.

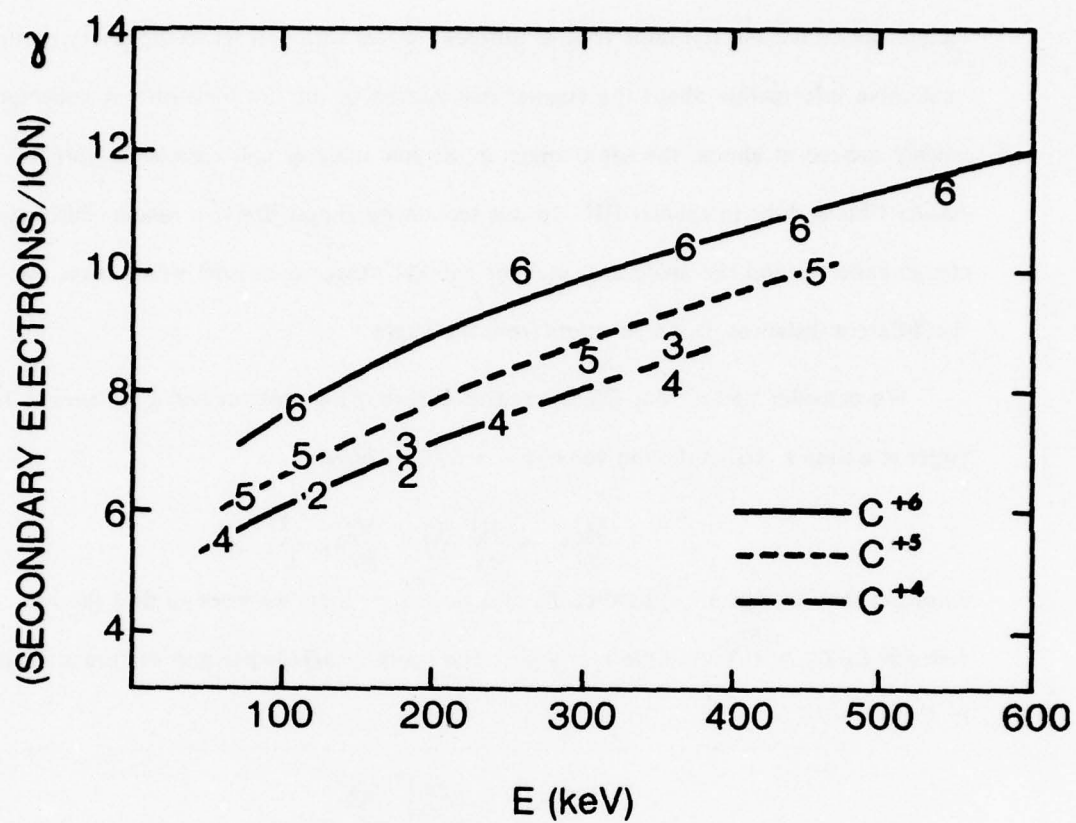


Fig. 2.18. Influence of the charge state of carbon ions on the secondary electron emission coefficients for copper surfaces.

1. Ion Velocity Distributions

As discussed before, charge collectors are not as useful as an ion analyzer to obtain quantitative information about the plasma expansion. However, because of their small size and simplicity they can be used as a complement to the ion analyzer. For example, several charge collectors can be used at the same time at different angles with respect to the laser axis to provide qualitative information about the angular distribution of the ion blow-off. A collector is then usually located at almost the same angle as the ion analyzer and correlated with the analyzer results (this is done in chapter III). In this section we simply derive a relationship between the charge collector and the analyzer signal (or another charge collector) which takes into account the different distances of the detectors from the target.

We consider the current $\partial Q/\partial t$ measured through a unit surface a distance L from the target at a time t . Using the ion velocity $v = L/t$, we have

$$\frac{\partial Q}{\partial t}\bigg|_L = \frac{\partial Q}{\partial v} \frac{\partial v}{\partial t} = \frac{\partial Q}{\partial v}\bigg|_L \frac{v^2}{L}. \quad (2.23)$$

Knowing the ion current a distance L_1 at a time $t_1 = L_1/v$, we want to find the ion current a distance L_2 ($L_2 > L_1$) at a time $t_2 = L_2/v$. The quantity $\partial Q/\partial v$ per unit surface at L_2 is related to L_1 by

$$\frac{\partial Q}{\partial v}\bigg|_{L_2} = \left(\frac{L_1}{L_2}\right)^2 \frac{\partial Q}{\partial v}\bigg|_{L_1}, \quad (2.24)$$

where the factor $(L_1/L_2)^2$ is due to spherical expansion. Using Eq. (2.24) and (2.23), we find that the ratio between the ion current measured at two different locations is given by

$$\frac{\partial Q/\partial t|_{L_1}}{\partial Q/\partial t|_{L_2}} = \left(\frac{L_2}{L_1}\right)^3 \quad (2.25)$$

The ion current corresponding to a given ion velocity is therefore expected to decrease as $1/r^3$ with increasing distance from the target. This of course, assume that charge exchange and/or recombination does not affect the charge state of the expanding ions.

2. Ion Energy Distributions

In this section we discuss how to obtain ion energy distributions from raw analyzer data. We first treat the case where the analyzer resolution was sufficient to separate all the ions species emitted by the plasma. Next, in Section 2.2, we address the case where two ion species have the same A/Z but different charges.

2.1. Data Analysis

The first step in the data reduction process is the identification of the ion species on the oscilloscope trace associated with each E/Z channel, as described in Section 2.3.2. of the instrumentation section. Next, the actual signal response of each ion species for each E/Z channel is determined, using the amplification factors of the analyzer channels. At this point, the signals levels are simply due to the ion current plus the secondary electrons according to

$$\frac{dQ_\alpha}{dt} = (Z + \gamma) e \frac{dN_\alpha}{dt}, \quad (2.26)$$

where Z , γ and N_α are respectively the atomic charge, secondary coefficient and number density of the α_{th} ion species. The ion flux dN_α/dt is the number of ions of species α passing the entrance slit of the ion analyzer per unit time.

The results from a typical shot are shown in Fig. 2.19a for the fast ion blow-off from a CH_2 target. Here, the ion current distributions dQ_α/dt as a function of E/Z , are shown for the H^+ and C^{+6} ion species. The curves are simply smooth fits through the analyzer data points. In Fig. 2.19b, the ion current distribution is converted to an ion flux distribution using

$$\frac{dN_\alpha}{dt} = \frac{dQ_\alpha}{dt} \frac{1}{e(Z + \gamma)}, \quad (2.27)$$

where γ is obtained from Fig. 2.17.

The final step in the data reduction process is to convert the ion flux distributions in Fig. 2.19b to ion energy distributions, i.e., $dN_\alpha/d(E/Z)$ as a function of E/Z . Using the ion energy $E = \frac{1}{2} Am_p (L/t)^2$ in the equation

$$\frac{dN}{dt} = \frac{dN}{d(E/Z)} \frac{d(E/Z)}{dt}, \quad (2.28)$$

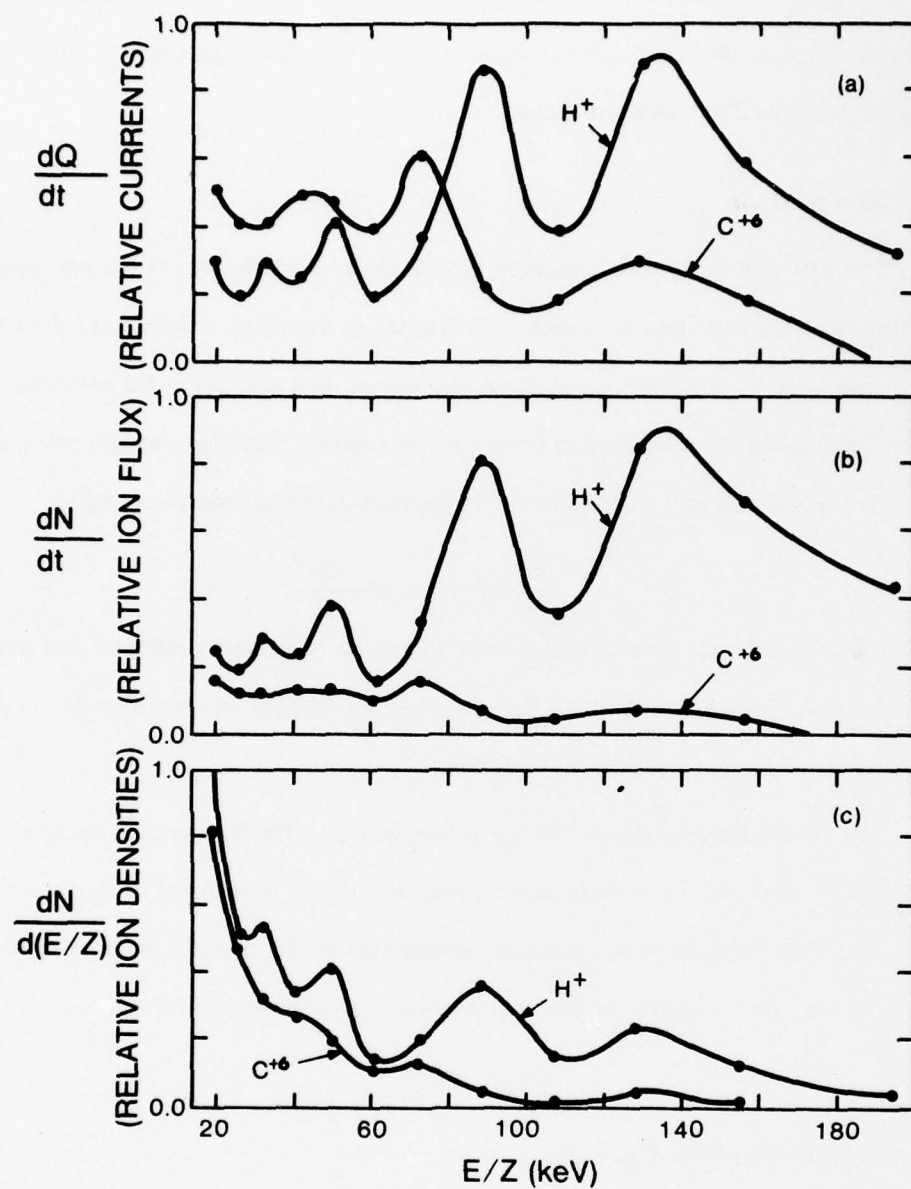


Fig. 2.19. Ion plus secondary electron current (a), ion flux (b), and ion number density (c) versus ion energy divided by the charge for C^{+6} and H^+ ion species.

given by

$$\frac{dN_{\alpha}}{d(E/Z)} = \frac{dN_{\alpha}}{dt} \left(\frac{m_p L}{2^{3/2}} \right) \left(\frac{A}{Z} \right)^{\frac{1}{2}} \left(\frac{E}{Z} \right)^{-3/2} \quad (2.29)$$

The ion energy distributions obtained from Fig. 2.19b, using Eq. (2.29), are shown in Fig. 2.19c.

In Fig. 2.19, the evolution of the data after each step of the data reduction process was shown as an example. In chapter III, however, only the ion energy distributions (Fig. 2.19c) will be presented for each shot that is discussed.

2.2. Charge Exchange Technique

Two ion species with an A/Z different by less than the analyzer resolution cannot be identified uniquely from Eq. (2.9). In our instrument the A/Z difference must be at least 10%. With that respect, C^{+6} and D^{+} ions from a CD_2 target would not be resolvable. However, one noticeable difference between D^{+} and C^{+6} ions is their atomic charge. We describe a charge exchange technique,^{92, 29} in this section, used to separate ions with the same A/Z but appreciably different Z . We first discuss the details of the technique and then give a specific example where this technique was used to obtain the energy distribution of C^{+6} and D^{+} ions from a CD_2 target. More information about the experimental results obtained from CD_2 targets using this technique will be given in chapter III.

The capture of an electron by an ion from a neutral atom, "charge exchange", is a two-body process that has been extensively studied in the literature^{93, 94}. In our case we are most interested in the charge exchange of ions with energies of tens of keV with the neutral background gas in a vacuum chamber. The charge exchange cross sections typically increase approximatively linearly with the ion charge. The C^{+6} ions are therefore much more sensitive to charge exchange than D^{+} ions (about one order-of-magnitude). One can therefore use charge exchange to preferentially lower the ionization state of the C^{+6} ions during their expansion. The resulting carbon ions, initially C^{+6} , would then have a lower A/Z which can be

distinguished from the D^+ upon detection in the ion analyzer. Since charge exchange does not significantly affect the ion energy, the original C^{+6} ion distribution can be reconstructed by the summation of the partial currents of the lower carbon ionization stages. This assumes that initially (at the target) the only carbon species present is C^{+6} and that the amount of the lower ionization states are known. We will soon show that under good vacuum conditions, the assumption that C^{+6} is the predominant species in the target plasma is valid.

We now proceed with an example where charge exchange was used to separate D^+ from C^{+6} ions for the case of a CD_2 target. First, we look at a shot that was taken with the pressure in both the analyzer and target chamber in the 10^{-7} Torr range. The ion current distributions are shown in Fig. 2.20. As expected the D^+ cannot be distinguished from the C^{+6} ions. One also notices the relatively small number of carbon ions with ionization state below 6 at this low chamber pressure. When the pressure was raised to 1.5×10^{-4} Torr (N_2 gas) on another shot under similar irradiation conditions, many carbon ion species with ionization state below 6 were now observed. This is shown in Fig. 2.21 where the carbon ion distributions are now plotted as a function of E instead of E/Z . In this example, one notes that, except for the amplitude, the current distributions of the different carbon species have the same general shape when plotted as a function of energy. This is not surprising since the carbon species were all C^{+6} initially. Since very few C^{+1} are observed, we infer that the neutral channel response was due primarily to neutral deuterium atoms (ejecting secondary electron emission from the detector).

At 1.5×10^{-4} Torr, most of the carbon ions are C^{+5} , C^{+4} and C^{+3} ions but a small fraction of C^{+6} is still present. The remaining C^{+6} ions are part of the D^+ signal in Fig. 2.21. The fraction of C^{+6} remaining after charge exchange can be determined by repeating the experiment under the same conditions with a CH_2 target instead of a CD_2 target. Current distributions similar to the ones shown in Fig. 2.21 are then obtained for all the carbon species, including C^{+6} ions. From these current distributions, the ratio between the C^{+6} ion current and the summation of the currents due to the other carbon species can be obtained as a function of the ion energy. The result

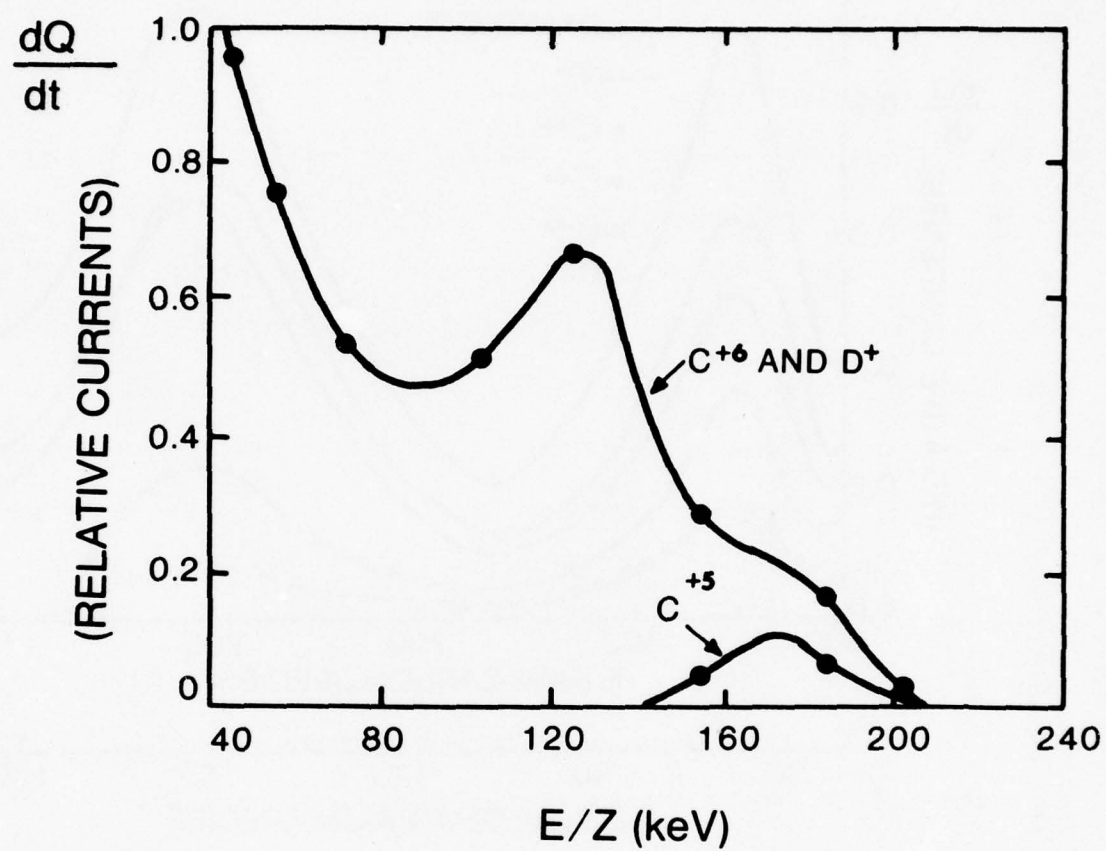


Fig. 2.20. Current distributions from a CD_2 target under good vacuum conditions (8×10^{-7} Torr).

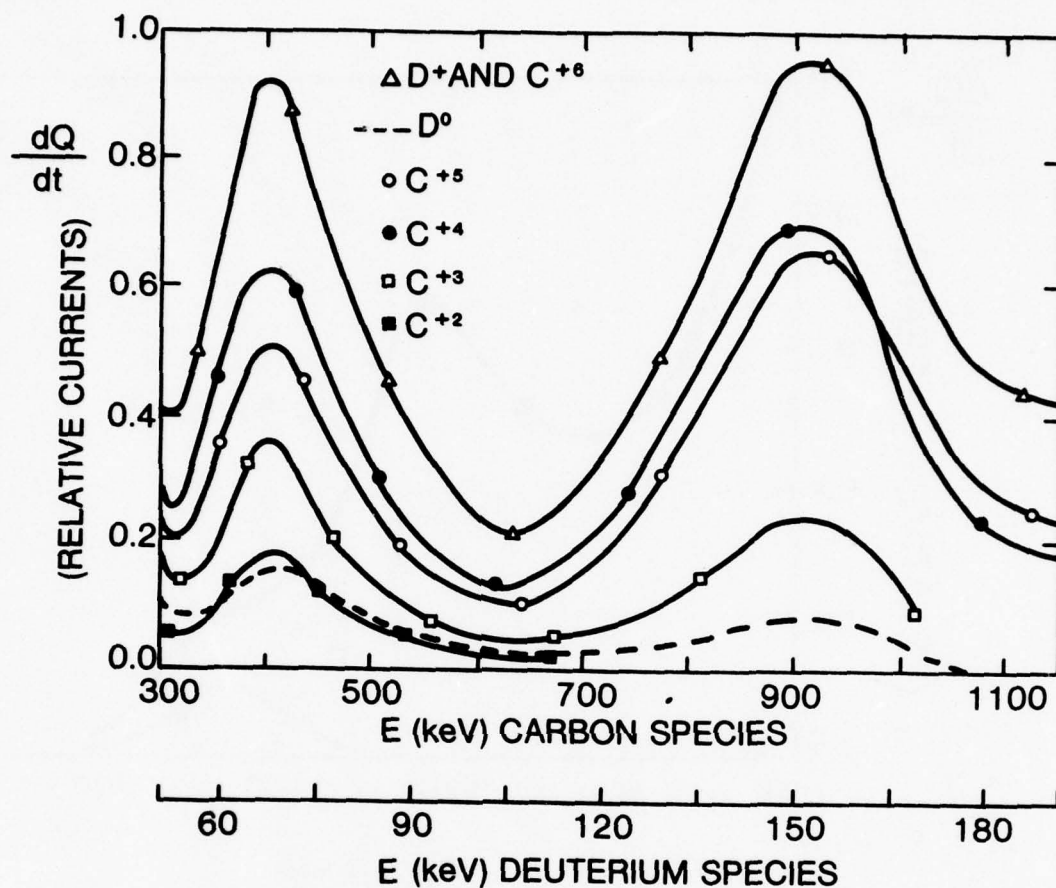


Fig. 2.21. Current distributions from a CD_2 target with a nitrogen gas background in the target chamber (1.5×10^{-4} Torr). The signal corresponding to C^{+1} ions was negligible over this energy range.

$$\left(I_{6,Z} / \sum_{Z=1}^5 I_Z \right),$$

where $I_{6,Z}$ is the carbon ion species current, is shown in Fig. 2.22. Due to the unavailability of data points at high ion energies, the dashed portion of the curve was extrapolated from the data using published charge exchange cross sections⁹³ (the ratio between the cross section at 1.2 and 0.9 MeV was used).

It should be mentioned, here, that all the charge exchange experiments were done with the target chamber backfilled with dry nitrogen to the appropriate pressure. In order to avoid a degradation of the analyzer resolution, charge exchange is avoided in the analyzer chamber by keeping its pressure as low as possible. With differential pumping, the analyzer chamber pressure can be kept an order-of-magnitude lower than the pressure in the backfilled target chamber. The ion flight distance at a pressure of 1.5×10^{-4} Torr is then about 80 cm with the analyzer arrangement shown in Fig. 2.9.

The ion energy distributions using CD_2 targets have been measured at a pressure of 1.5×10^{-4} Torr. The amount of charge exchange increases or decreases almost linearly with the chamber pressure for slight pressure variation around 1.5×10^{-4} Torr. This operating pressure was chosen such that the observed number of C^{+6} and C^{+1} ions would both be minimal at the same time. A small C^{+1} signal means that neutral carbon atoms are almost absent and can therefore not be confused with the fraction of neutral deuteriums observed on the neutral channel of the analyzer.

Using Fig. 2.2, one can now reconstruct the original C^{+6} and D^{+} ion current distributions from Fig. 2.21. The C^{+6} ion current left after charge exchange is first obtained from the summation of the carbon ion currents as explained above. Each carbon ion signal in Fig. 2.21 is next reduced to an ion flux dN_a/dt . The summation over the ion fluxes of each carbon species at a given energy gives the initial C^{+6} ion flux before charge exchange. Similarly, the D^{+} ion flux is determined by adding the neutral deuterium signal to the D^{+} ion current after correction for the secondary coefficient. The resulting ion flux distributions for C^{+6} and D^{+} ions are shown in Fig. 2.23 as a function of E/Z . The ion energy distributions can be obtained from the

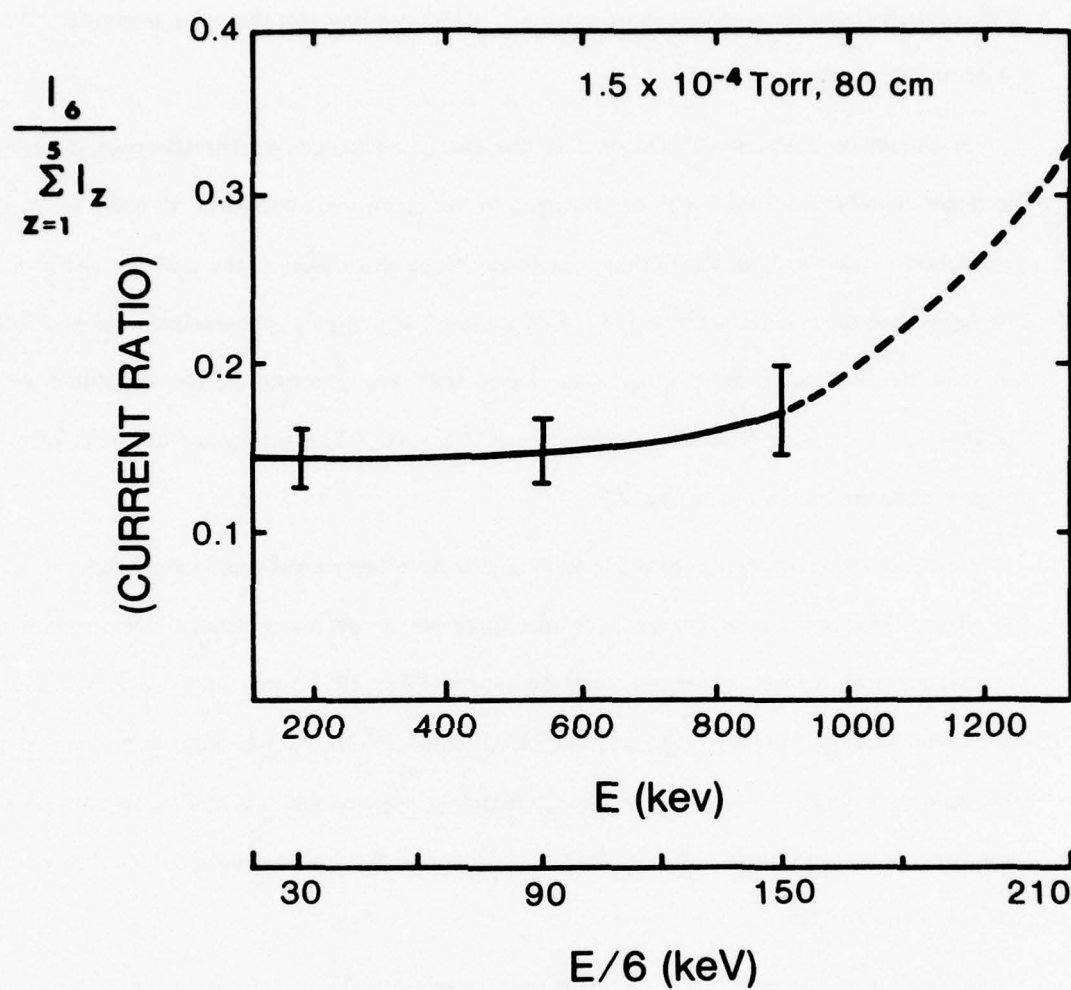


Fig. 2.22. Ratio of the C^{+6} ion current and the summation of other carbon species currents versus ion energy. The error bars are standard deviations over 4 shots.

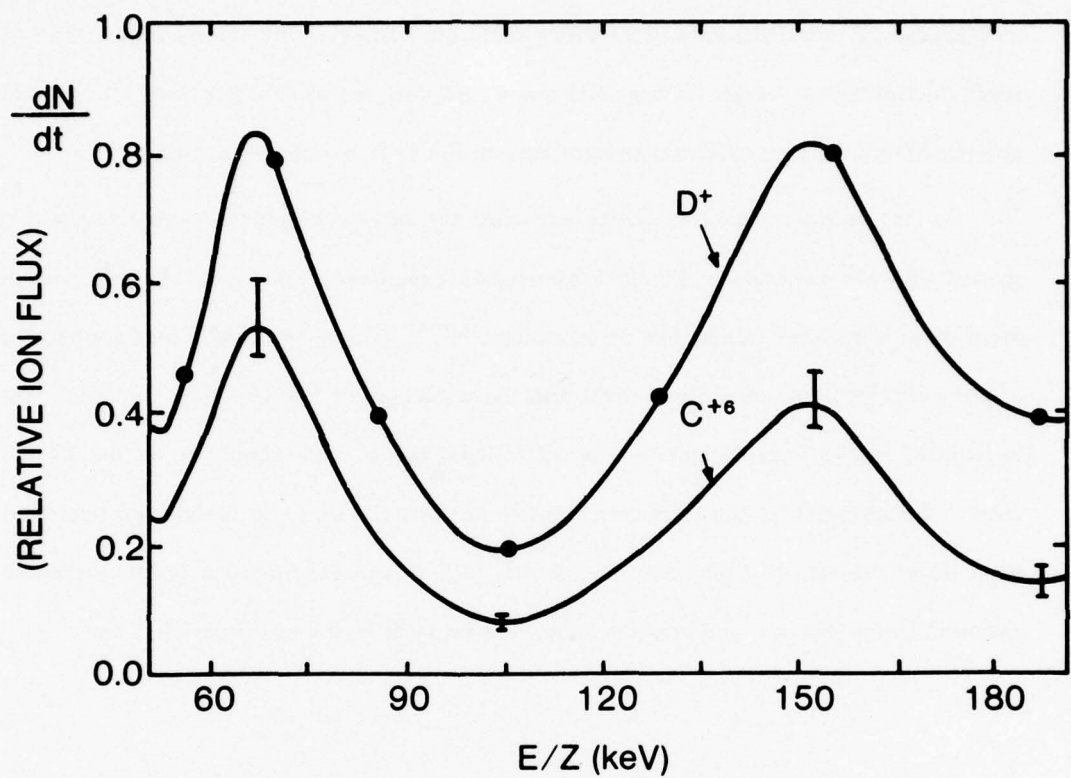


Fig. 2.23. Ion flux distributions for both C^{+6} and D^+ ions reconstructed from Fig. 2.21 and 2.22. The error bars represent uncertainties associated with the data reduction process.

ion flux distributions using Eq. (2.29), as discussed in the previous section.

A potential source of error in the data reduction from Fig. 2.21 to 2.23 is the finite energy channel spacing of the ion analyzer. The spacing between the channels is chosen such as to resolve the structure on the ion energy distributions with a minimum of data points. Interpolations of the exact shape of the distributions between the data points are therefore required. In most cases, this interpolation process yields some uncertainty in the summation of the carbon species at any given energy. In Fig. 2.23 and Chapter III, we usually represent the uncertainty estimated from the data reduction as error bars on the C^{+6} ion energy distribution.

So far, we have seen that charge exchange can be advantageously used to separate ion species with the same A/Z . In most laser-fusion experiments, however, charge exchange is more often a nuisance rather than an advantage.^{26,27,95} If only 5% of C^{+6} ions are allowed to charge exchange over a one meter flight distance, a vacuum of 5×10^{-6} Torr ($\sigma \approx 10^{-15} \text{ cm}^{-2}$) is required in the target chamber. For Al^{+11} ions, the vacuum should be in the 10^{-7} Torr range. These pressures are, however, usually inconsistent with the design and operation of most target facilities. In our case, except for CD_2 , all the experimental results presented in chapter III were obtained at a pressure which was below at least a few times 10^{-6} Torr.

Chapter III

EXPERIMENTAL RESULTS

In this chapter, experimental observations of high energy ions obtained at high laser irradiance are presented. Although the emphasis is on energetic ion measurements, some x-ray spectra obtained on the same shots are also presented. The chapter is divided into three sections. In the first section, the measurements of ion energy distributions for different target parameters are detailed, together with some general properties of the energetic ion expansion. The relative importance of energetic ions with respect to the total ion blow-off is also pointed out. The second section deals with the x-ray emission obtained on the same shots as the energetic ions. From the x-ray spectra, a lower-bound estimate on the hot electron temperature required to produce energetic ions is derived. In the last section the results are summarized and some interpretations of the observations are discussed.

A. High Energy Ion Expansion

The ion measurements reported in this chapter were obtained over a limited but interesting range of parameters. In most cases the laser irradiance was around 10^{16} W/cm² for 75-psec Nd-laser pulses. The targets were thick (\approx 1-2mm) plastic slabs (CH₂, CH, CD₂) which were oriented at different angles with respect to the laser axis (Fig. 3.1). This particular choice of experimental conditions is relevant to many laser-fusion schemes, as noted in chapter I.

When the target is irradiated normal to the laser axis, the ion blow-off peaks back toward the focusing lens. In order to observe the intense portion of the ion blow-off, the target is then rotated by an angle θ_t toward the ion analyzer which is itself at an angle θ_d (see Fig. 3.1). The minimum observation angle for the analyzer (35°) is limited by practical considerations such as the geometry of the target chamber and the solid angle subtended by the focusing lens holder. For $\theta_t = \theta_d$, the ion energies and densities are maximum for the analyzer, although the angular distribution is no longer symmetrical with respect to the target normal. Most of the ion features emphasized in this chapter were obtained for the case $\theta_t = \theta_d$. However, we will point

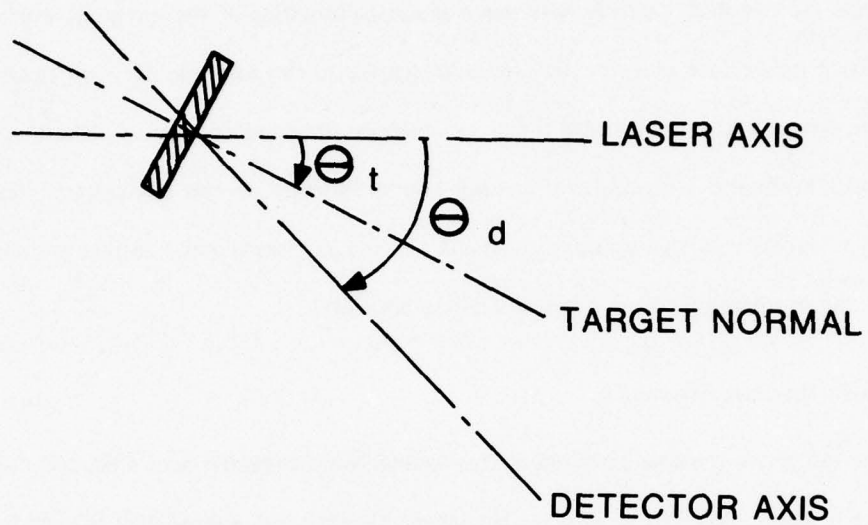


Fig. 3.1 Schematic defining the angle of the target normal and the detector axis with respect to the laser axis.

out some of the differences in the ion expansion properties as a function of angle between the analyzer and the target normal.

First, we are going to discuss in details the features of high energy ions emitted normal to a CH_2 and CH target for the case $\theta_i = \theta_d = 35^\circ$ at 10^{16} W/cm^2 . Second, we consider other angles, the angular dependence of the ion expansion, and the irradiance dependence of energetic ions. Finally, information about ionization effects during the acceleration phase of the ion expansion are inferred from the ion energy distributions obtained using CD_2 targets.

a). Observations Normal to the Target Surface at High Irradiance

In this section, we consider only the case where both the target normal and ion analyzer are at 35° with respect to the incident laser beam, the laser irradiance is fixed at about 10^{16} W/cm^2 . The energy distributions of the high energy ion species are first measured for both CH_2 and CH targets and some features about the relative behavior of the ion species are pointed out. Next, the ion analyzer results are correlated with charge collector signals obtained at almost the same angle as the analyzer axis. The energy content and the relative importance of the energetic ions with respect to the entire ion blow-off are then estimated.

1. Ion Energy Distributions

Typical single-shot energy distributions of high energy ions due to the Nd-laser irradiation (75 psec, $\sim 10^{16} \text{ W/cm}^2$ with an $f/2$ lens) of a CH_2 (polyethylene) target are shown in Fig. 3.2a. In this case, the analyzer axis and target normal were both at 35° with respect to the laser axis. The laser beam polarization orientation is at 45° with respect to the plane defined by the target normal and the laser axis. The analyzer data points have been reduced as in Chapter II, and the curves are simply smooth fits through the data points associated with each ion species. Figure 3.2b shows the oscilloscope trace of the charge collector located at almost the same angle as the analyzer. The portion of the collector trace between the dashed lines corresponds to the energy range covered by the analyzer on this shot. The charge collector result will be discussed in more detail below, in Section 2.

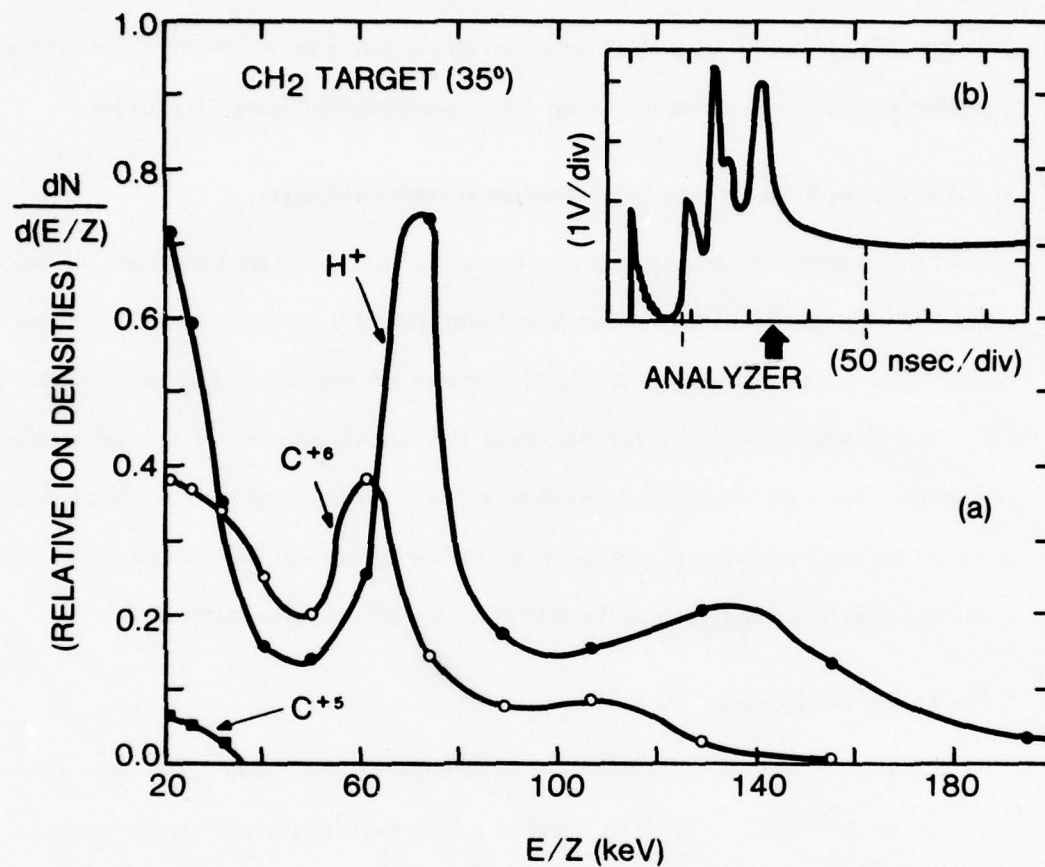


Fig. 3.2. (a) High energy ion distributions from a CH_2 target normal to the analyzer axis. (b) Oscilloscope trace from a biased charge collector showing the portion of the trace sampled by the ion analyzer.

We now discuss some features of the ion energy distributions such as shown in Fig. 3.2a. About 15 shots were taken under similar conditions to those of Fig. 3.2. Multiple peaks were always observed on both the H^+ and carbon energy distributions but were nonreproducible in detail. Another common feature, which can be seen in Fig. 3.2, is that no ionization stages lower than C^{+5} (and only a small fraction of C^{+5}) appeared under good vacuum conditions ($< 10^{-5}$ Torr). This guarantees that recombination does not determine the charge state or affect the expansion of the high energy ions.

Although the relationship between individual C^{+6} and H^+ peaks is obscure, the average ratio of H^+ to C^{+6} ions is increasing with E/Z . In fact, above 50 keV/Z, close to half the ion energy is transported by H^+ ions in Fig. 3.2. An average over seven shots is shown for the ion energy distributions of the hydrogen and carbon species in Fig. 3.3. The large error bars (standard deviations) are due to the nonreproducibility of the multi-peak structures from shot to shot. Averaging several shots smoothed out some of the structures on the ion distributions. It then becomes more obvious that an important fraction of the expansion energy is carried away by H^+ ions at high energy.

The ion energy distributions obtained using a CH (polystyrene) target under similar conditions to those used for the CH_2 targets are shown in Fig. 3.4a. The portion of the charge collector signal detailed by the analyzer data is shown in Fig. 3.4b. The charge collector signal is similar in shape to the CH_2 target results presented in Fig. 3.2b. The nonreproducibility of the structure on the ion energy distributions makes detailed quantitative comparison with the CH_2 results difficult. However, for the four shots taken under these conditions, an important group of H^+ ions is always observed at higher energy than the C^{+6} ions, as in the CH_2 case. Except for the expected reduction in the number of H^+ ions (about a factor of two less than CH_2), the results obtained from a CH target are found to be very similar to those obtained from CH_2 targets.

In summary, some of the predominant features of high energy ion distributions observed normally to a CH_n ($n = 1$ or 2) target surface at $\sim 10^{16}$ W/cm² are: the energetic ion species

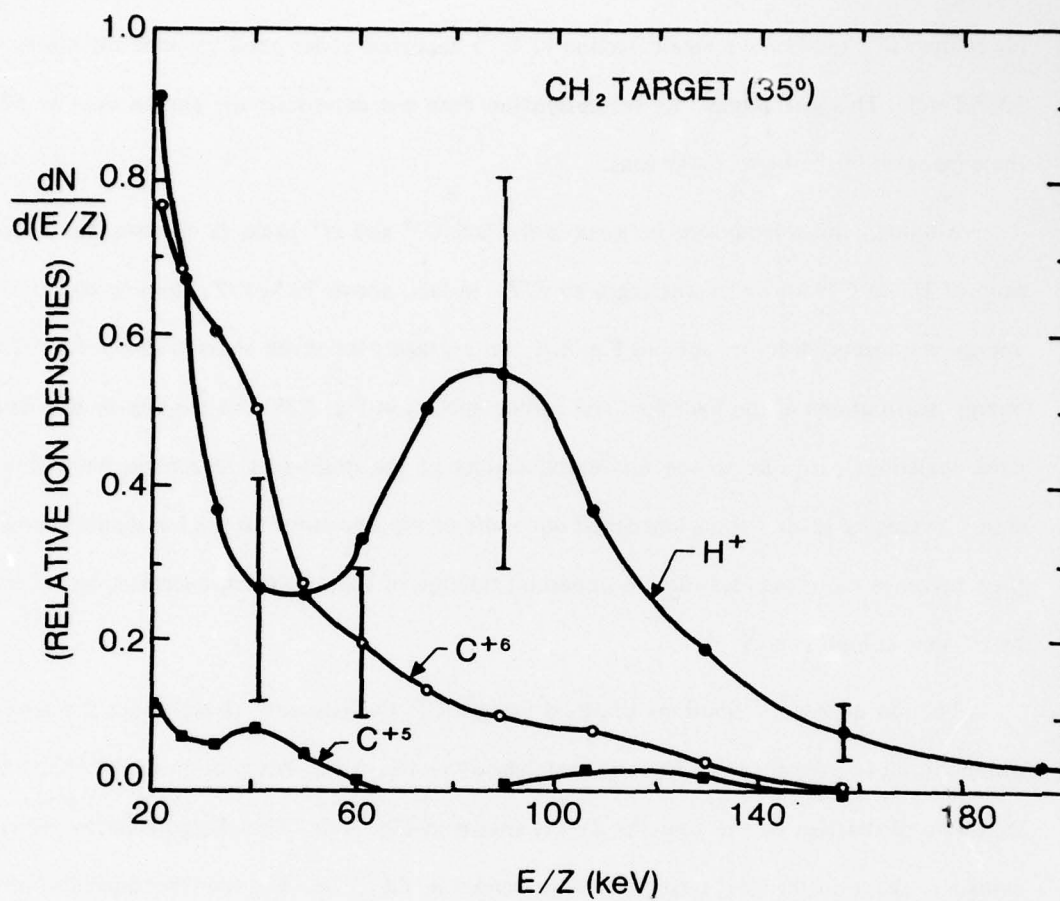


Fig. 3.3. Average over 7 shots of ion energy distributions from a CH_2 target normal to the analyzer axis. The large standard deviations are due to the unreproducible multi-peak structures from shot to shot.

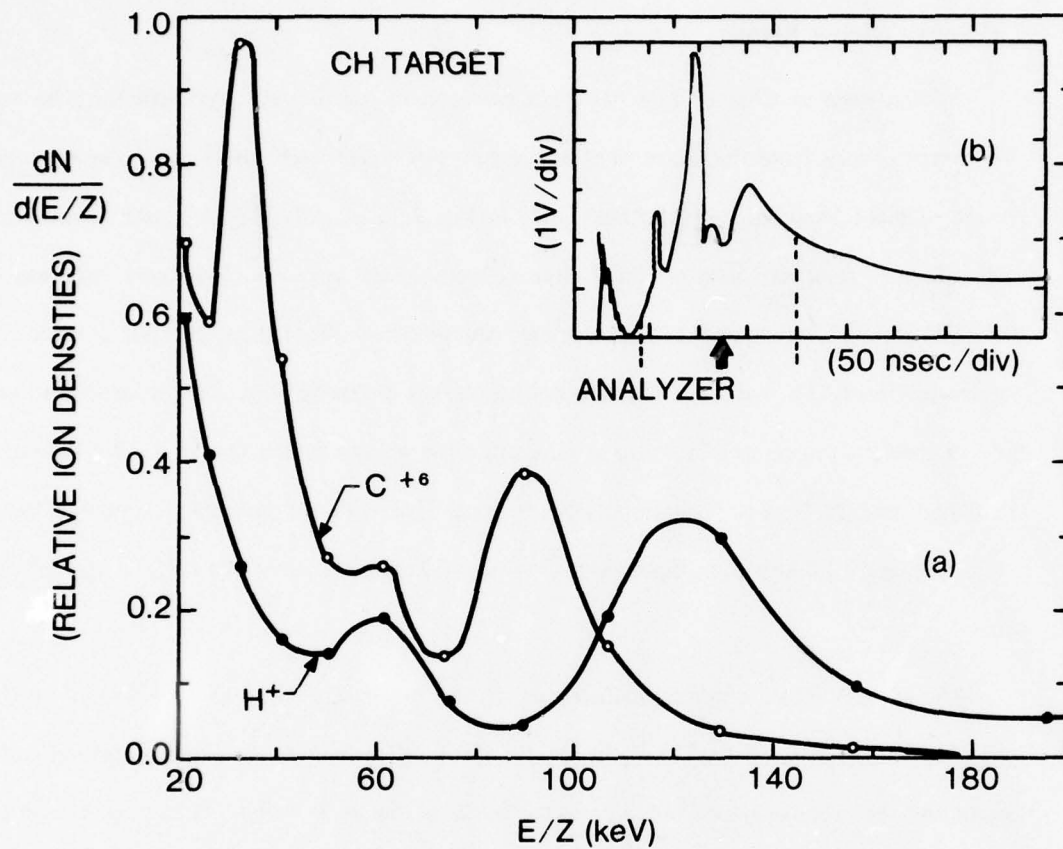


Fig. 3.4. (a) High energy ion distributions from a *CH* target normal to the analyzer axis. (b) Oscilloscope trace from a biased charge collector showing the portion of the trace sampled by the ion analyzer.

are highly ionized, little correlation exist between the structure on the energy distributions of the ion species, and H^+ ions are preferentially accelerated to higher E/Z than the C^{+6} ions. We will see later that preferential acceleration of the H^+ ions to higher E/Z than the C^{+6} is a characteristic of a strong pressure gradient accelerating the ions to high energies.

2. Charge Collector Results

As discussed in Chapter I, it has been common in the literature to distinguish between two groups of ions from the shape of a charge collector signal trace: the bulk of the expanding plasma or main blow-off, and the "fast" ion. In Fig. 3.2b, the "fast" ions would be associated with the early peak structure on the charge collector trace (e.g. $t < 130$ nsec), whereas the "thermal" blow-off, which arrives later in time, contains the bulk of the expanding plasma. It is noteworthy, however, that "fast" ions are not necessarily energetic ions. Proper identification of the ion species is necessary in order to determine the energy of the fast ions. We define the term "high energy" ions or "energetic" ions, here, as ions with energies above a predetermined arbitrary energy (50 keV/Z in most cases), without reference to structure on a charge collector trace.

The charge collector signal reconstructed from the partial current of hydrogen and carbon ions obtained from Fig. 3.2 is shown in Fig. 3.5. The difference between the carbon ion contribution and the reconstructed charge collector signal is due to H^+ ions. The actual charge collector signal, obtained on the same shot as Fig. 3.2, at almost the same angle as the analyzer, differs somewhat from the analyzer reconstruction of the collector signal in Fig. 3.5. A fraction, but not all of the discrepancy can be accounted for from the finite energy resolution of the analyzer. A more consistent explanation is that the multi-peak structure observed in Fig. 3.2a varies on an angular scale as small as the 2 degrees between the collector and the analyzer axis. We will see in the next section that the multi-peak structure is angle dependent. In Fig. 3.2b (and the remainder of this chapter), the reconstruction of the analyzer results was used for the high energy part of the collector signal. Beyond 140 nsec in Fig. 3.2b, the actual charge collector signal was used because the analyzer results for H^+ are no longer available.

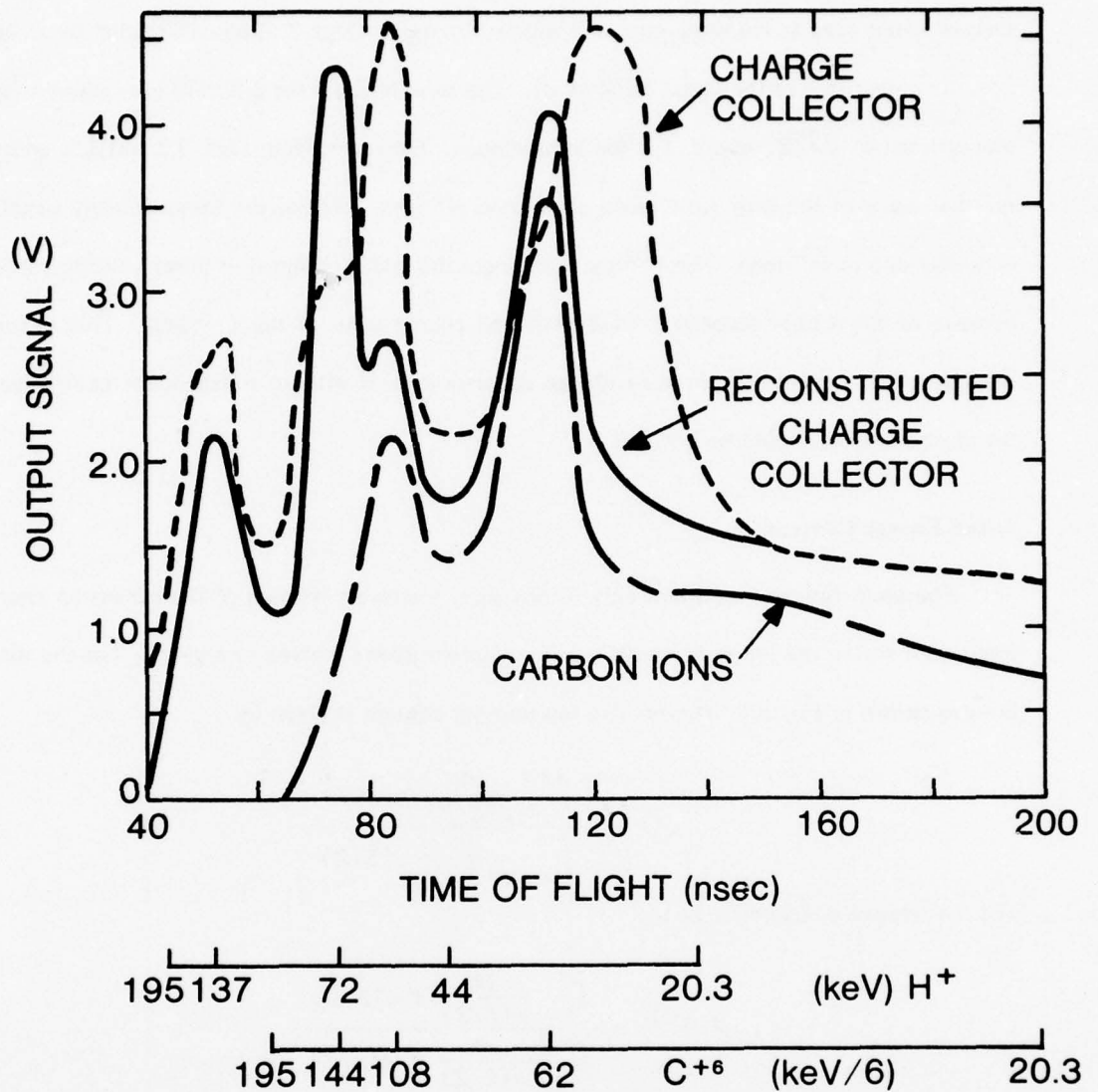


Fig. 3.5. Reconstruction of the charge collector and carbon ion signal from the ion energy distributions shown in Fig. 3.2. The actual charge collector signal measured 27 cm from the target surface at almost the same angle as the analyzer is also shown for comparison. The energy scales represent the analyzer energy range for H^+ and C^{+6} ions.

It was argued²³⁻²⁵, before ion analyzers were in common usage, that the first peak on the charge collector, such as in Fig. 3.5, was due to H^+ ions and that subsequent peaks were successively lower ionization stages of carbon ions. This interpretation assumed that different ion species would peak at the same energy E divided by their charge Z after acceleration by an electrostatic potential ϕ at the target ($E/Z = \phi$). The time-of-flight for different ion species is then proportional to $\sqrt{A/Z}$, where A is the atomic mass. However, from Figs. 3.2 and 3.5, one can see that many of the early time peaks are due to H^+ ions, whereas the lower velocity structure is mostly due to C^{+6} ions. The C^{+6} ions dominate the collector signal at lower velocity partially because of the higher secondary coefficient and charge state of the C^{+6} ions. This example illustrates that the interpretation of charge collector signals without independent knowledge of the charge species should be avoided.

3. Ion Energy Content

Energetic ions are important only if they carry a sizeable fraction of the expansion energy. Figure 3.6 shows the ion energy and number content above a given energy E_{\min} for the distributions shown in Fig. 3.2. The relative ion number content is given by

$$\eta(E) = \frac{\int_{E/Z}^{\infty} \frac{dN}{d(E/Z)} d(E/Z)}{\int_{E_{\min}}^{\infty} \frac{dN}{d(E/Z)} d(E/Z)},$$

and the relative energy content by,

$$\epsilon(E) = \frac{\int_{E/Z}^{\infty} \frac{dN}{d(E/Z)} E d(E/Z)}{\int_{E_{\min}}^{\infty} \frac{dN}{d(E/Z)} E d(E/Z)}.$$

The minimum energy considered is $E_{\min} = 5 \text{ keV/Z}$. Between 5 and 20 keV/Z the charge collector signal was used with the assumption that the number of H^+ ions remains twice the number of carbon ions over this energy range. The secondary coefficients and charge states assumed over this energy range are shown in Table 3.1. Uncertainties in the secondary coefficients and charge states of the ions make the collector signal unreliable below 5 keV/Z. A gross estimate of the ion energy distributions below 5 keV/Z indicates that neglecting the ions

Table 3.1. Average charge state and secondary electron emission coefficient, used in Fig. 3.6, below 20 keV/Z.

Energy (keV/Z)	$\gamma + Z$	
	Hydrogen	Carbon
5	3.0	10
10	3.3	11
15	3.6	12

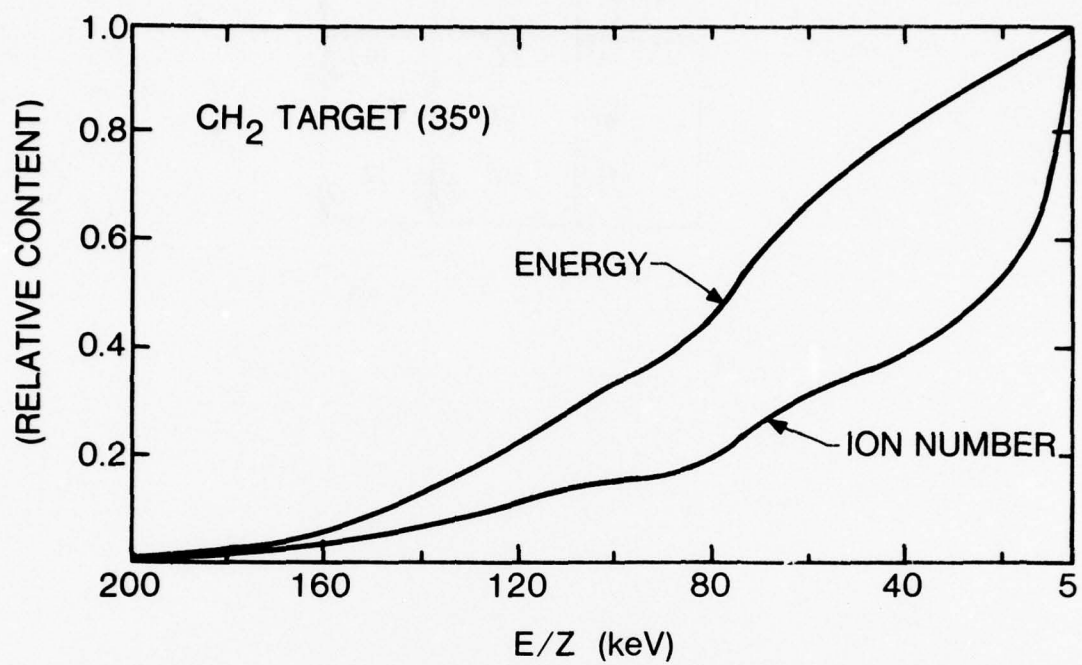


Fig. 3.6. Energy and ion number content inferred from the analyzer and charge collector results of Fig. 3.2.

below 5 keV/Z probably underestimates the ablated total ion mass by at least a factor of two, while the energy content is likely to be affected by no more than 10%.

Figure 3.6 can be used to estimate the fraction of the ion expansion energy transported by the so-called "fast" ion group of Fig. 3.2b in the direction normal to the target. We arbitrarily chose the separation between "fast" and slow ions at 130 nsec (50 keV/Z for C^{+6} ions). From Fig. 3.6, we then find that less than 35% of the ions carry 75% of the expansion energy. Keeping in mind that the 35% figure is an upper-bound on the fast-to-slow ion number ratio, we conclude that the fast ions normal to the target are a relatively small group of ions transporting an important fraction of the ion expansion energy.

b). Observations at Other Target Angles and Irradiances

The last section dealt with the basic features of the ion expansion normal to a CH_n target surface at $\sim 10^{16}$ W/cm². At this point, it would be useful to consider the effects of lower target irradiances and different relative target-analyzer angles on the ion measurements. In this section, we show that the basic features discussed in the previous section about the ion distributions are insensitive to the target angle. The relative energy content of the energetic ions is, however, angular dependent. Finally, the energy content in the fast ions appears to scale linearly with target irradiance at a given collector angle.

1. Ion Energy Distributions

In order to see the effects of the target angle on the ion energy distributions, we repeated the same set of experiments as those reported in the previous section, except that the CH_2 target was rotated to 22.5° with respect to the laser axis instead of 35°. The analyzer axis was kept at 35°. Typical single-shot ion energy distributions are shown in Fig. 3.7a for the conditions $\theta_t = 22.5^\circ$, $\theta_d = 35^\circ$ and $\sim 10^{16}$ W/cm². The portion of the charge collector signal covered by the analyzer results is indicated by the dashed lines in Fig. 3.7b. The structures on the H^+ and C^{+6} ion energy distributions are both still observed and nonreproducible from shot-to-shot. Little correlation is again found between the C^{+6} and H^+ peaks, except that the average ratio of

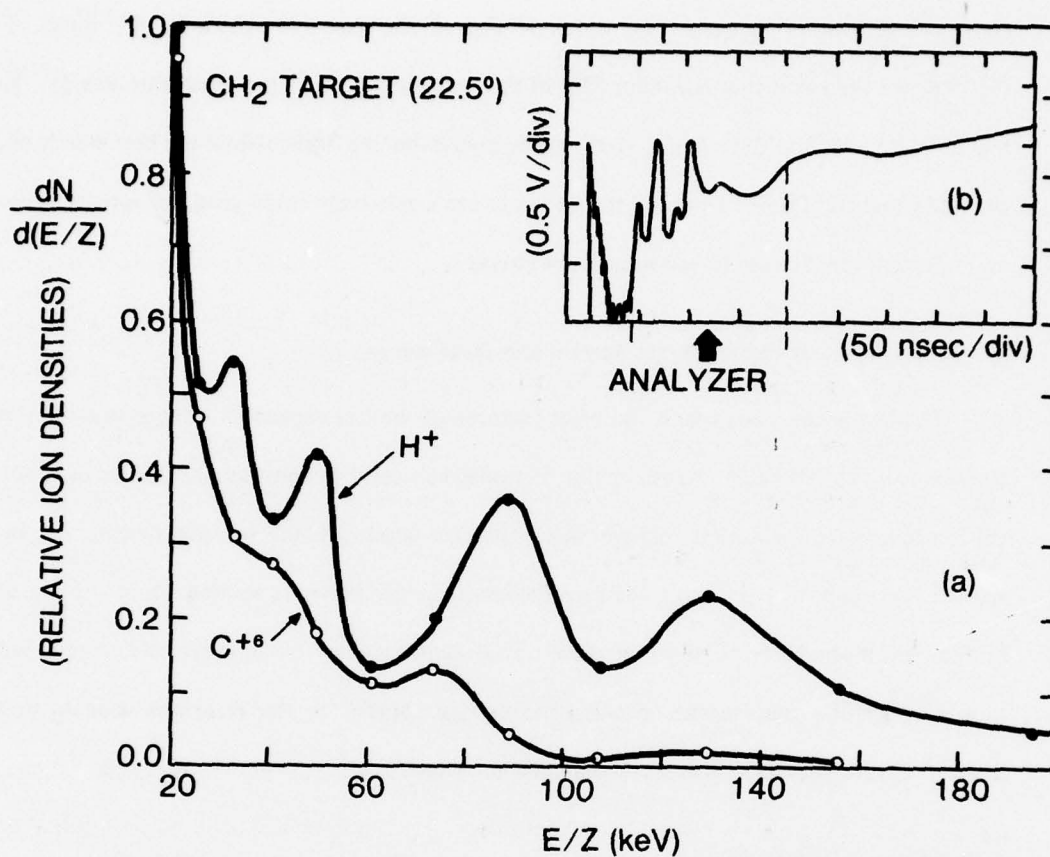


Fig. 3.7 (a) High energy ion distributions from a CH_2 target at a different angle than the analyzer axis. (b) Oscilloscope trace showing the portion of the trace sampled by the ion analyzer.

H^+ to C^{+6} ions is still increasing with E/Z . Above 50 keV/Z, more than half the ion energy is transported by H^+ ions. The reconstruction of the charge collector signal from the analyzer results is shown in Fig. 3.8. Again, the early peak structure is dominated by the H^+ ions, whereas the later portion is due mostly to the C^{+6} ions.

Figure 3.9 represents an average over seven shots of the ion energy distributions of the H^+ and C^{+6} ion species. Again, the carbon ions are essentially fully ionized. It is also obvious that the ratio of H^+ to C^{+6} ions is increasing with energy and that an important fraction of the energy is transported by energetic H^+ ions.

We will see, in the next section, that the energetic ion blow-off portion is limited mostly to a relatively narrow cone angle with a peak intensity somewhere between the target normal and the laser axis. The ion energy distributions presented above for the case $\theta_t = 35^\circ$ and 22.5° are samples of this intense blow-off region. Since both target angles exhibit many similar results, we conclude that the basic features of the ion energy distributions are insensitive to the target angle near the normal directions.

2. Angular Dependence of Ion Expansion

We have already mentioned that the energy content of the energetic ions is strongly angular dependent. This can readily be observed in Fig. 3.7b and 3.2b where two typical charge collector results are shown for the same observations angle, but with a target rotated at a different angle, i.e., 22.5° and 35° respectively. Although some features mentioned above about the ion distributions are common to both target angles, differences exist between the charge collector results. The ion current of the main ion blow-off ($t > 130$ nsec) is comparable at the two angles, but the energetic ion current (> 50 keV/Z for C^{+6} ions) is reduced by almost a factor of three, for the target rotated to 22.5° relative to 35° . In Fig. 3.7b, the energy transported by the energetic ions is then reduced to about 50% of the total ion expansion energy above 5 keV/Z. This is to be compared with 75% of the ion energy in energetic ions at the target normal in Fig. 3.2b.

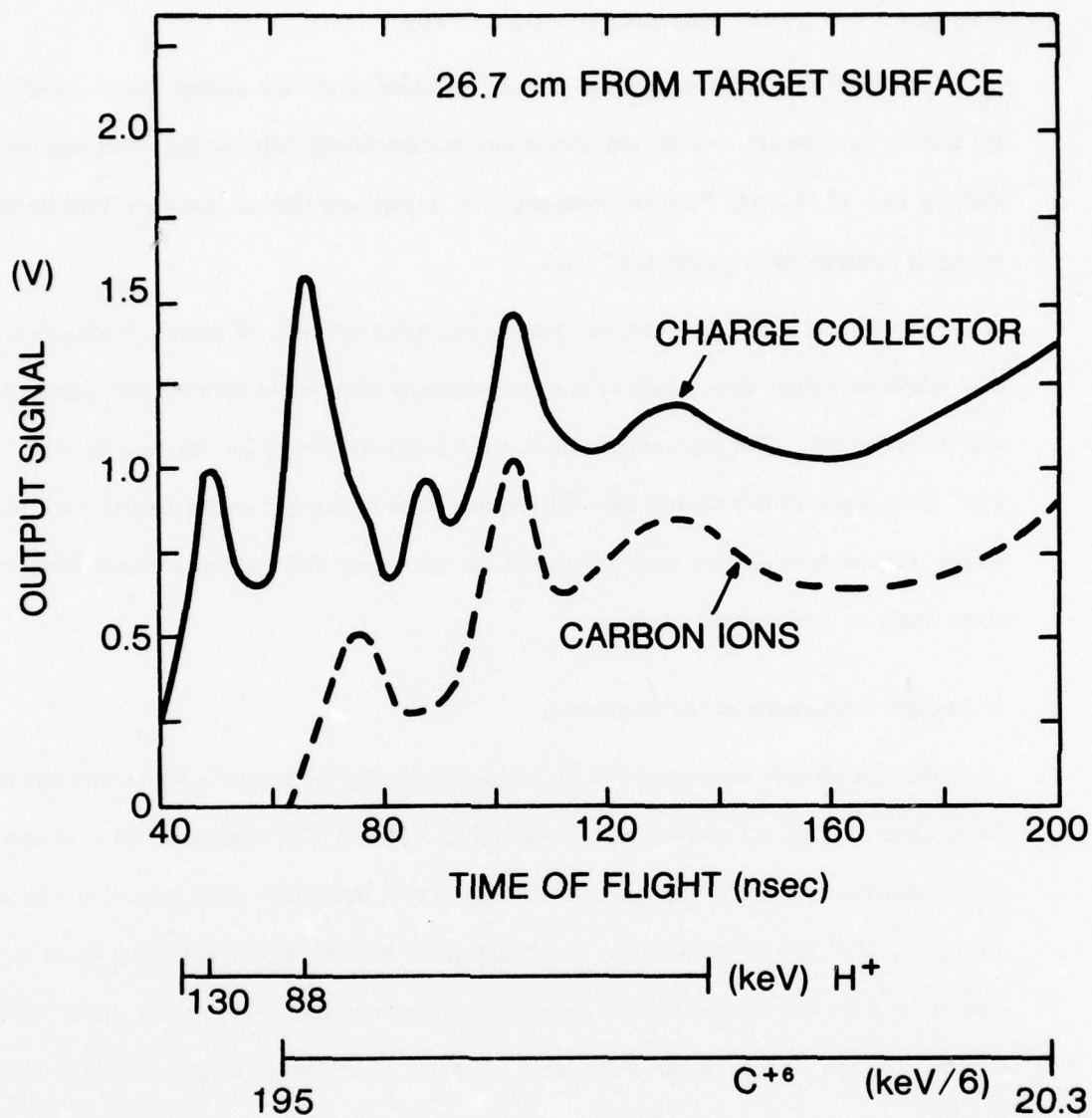


Fig. 3.8. Contribution of the carbon ion signal to the charge collector signal for the ion energy distributions of Fig. 3.7. The difference between the carbon ion and the charge collector signal is due to H^+ ions. The energy scales represent the analyzer energy range for H^+ and C^{+6} .

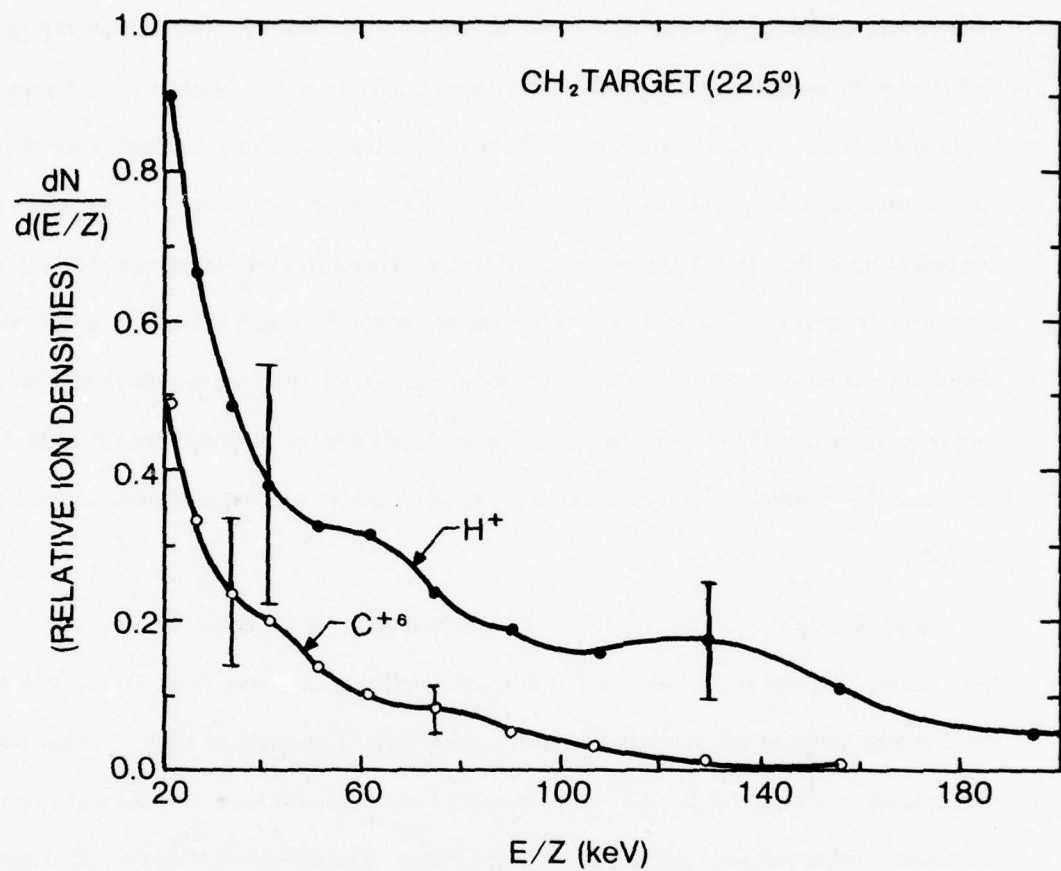


Fig. 3.9. Average over 7 shots of ion energy distributions from a CH_2 target at a different angle than the analyzer axis.

It is noteworthy that changing the target angle instead of the direction of observation can affect the laser-plasma interaction and/or the plasma expansion. Under similar conditions to those reported above ($\sim 10^{16}$ W/cm² with a f/1.9 lens), the fractional absorption of the incident laser energy was shown to remain approximately constant⁵⁸ as the target is rotated from normal incidence up to 50°-60°. The hot electron temperature inferred from the spatially and temporally integrated x-ray emission in the next section is also insensitive to whether the target angle is 35° or 22.5°. However, although some features of the ion energy distributions are common to both target angles, the shape of the angular distribution of energetic ions is dependent upon the target angle as discussed below. Therefore, the ion energy contents measured at a given location for different target angles cannot be readily related to measurements obtained for a fixed target angle at different locations. The purpose of the above estimates was simply to show that the energy content of the energetic ions is, indeed, strongly angle dependent, and that a sizeable fraction of the ion energy is carried by energetic ions near the target normal.

A gross estimate of the relative angular distribution of energetic ions can be obtained from charge collector signals recorded at different angles on the same shot. Figure 3.10 shows three charge collector traces obtained on the same shot. The angle of the CH target was 35° with respect to the laser axis. All three detectors have been corrected, in time and amplitude, for different solid angles and distances from the target. The detector at 0° is a small charge collector which was mounted on the lens axis.

From Fig. 3.10, one sees that, for a target rotated to a given angle, the ion blow-off is asymmetrical with respect to the target normal. Such an asymmetry is not observed when the target normal is parallel to the laser axis. Another general observation is that the high energy ions tend to expand more along the laser axis than the slower ions. The angular distribution of the slower ions is also more isotropic than the high energy ion distribution, i.e., the energetic ions expand into a smaller cone angle than the "thermal" ions. These results have also been observed by other means under different experimental conditions^{96,97}. The 1-D model

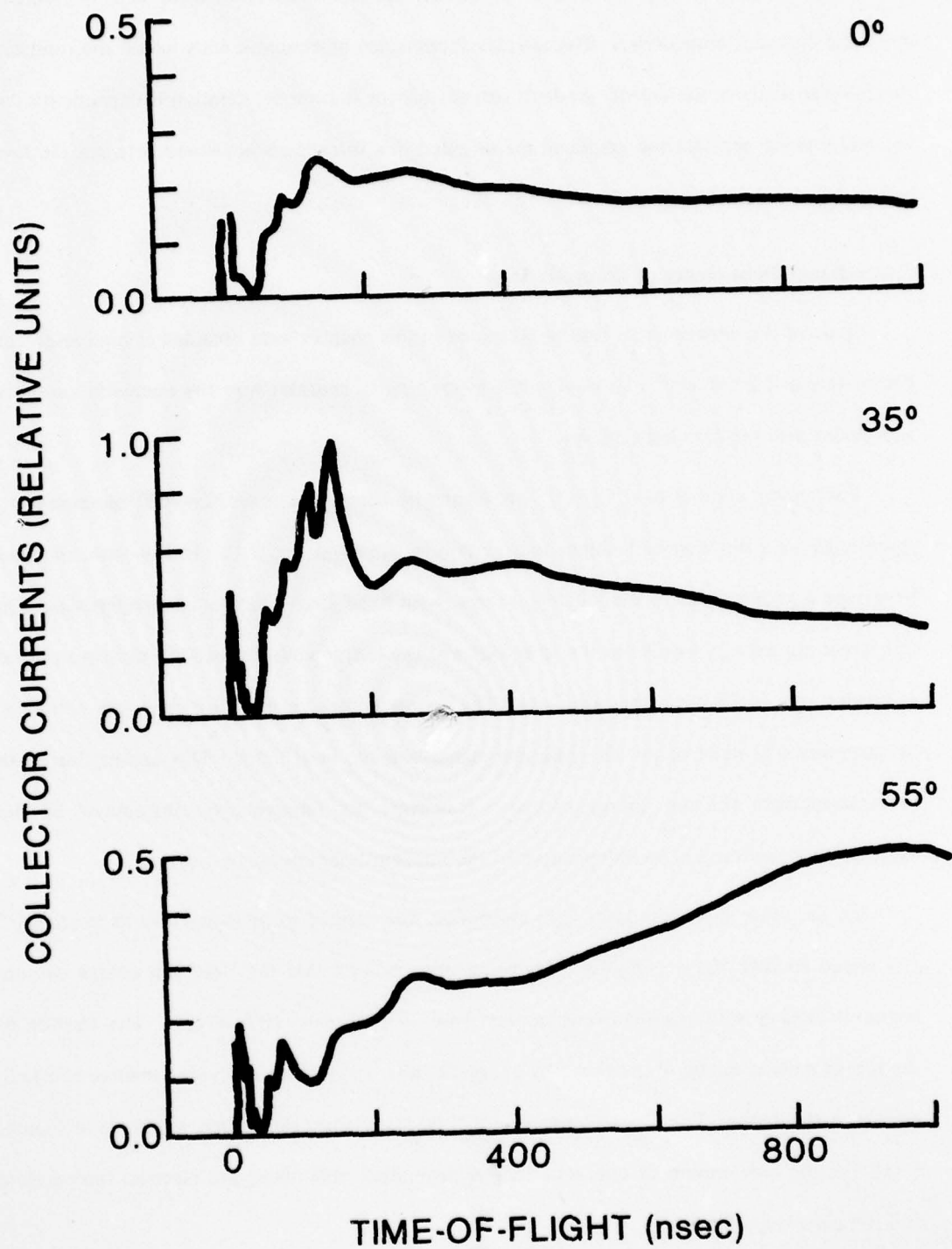


Fig. 3.10. Normalized charge collector signals obtained on the same shot at three different angles between the collectors and the laser axis. The CH_2 target was normal to the 35° collector.

presented in the next chapter shows that energetic ions are produced by steep density gradients and high electron temperature. The angular dependence of energetic ions would then indicate that the geometry of the density gradient responsible for the ion acceleration is dependent upon the target angle and that the gradients are oriented in a direction somewhere between the laser axis and the target normal.

3. Irradiance Dependence of Energetic Ions

Most of the experimental results presented in this chapter were obtained at high laser irradiance (about 10^{16} W/cm²). However, it is interesting to consider how the energetic ion emission scales with incident laser energy.

The energy content of the "fast" ions (structure before the main blow-off) measured at a given angle as a function of incident laser energy is shown in Fig. 3.11. In this case, the laser irradiance is proportional to the incident energy, with fixed focal and beam characteristics. The CH target normal was parallel to the laser axis and the charge collector used to measure the ion expansion was at 35° from the laser axis. The energy content in the "fast" ions was estimated by assuming that most of the energetic ion signal was due to H⁺ ions. This assumption tends to underestimate the ion energy content. However, the relative error introduced by this assumption is assumed to be independent of the incident laser energy on target.

On the same shots, the laser light absorption was verified to be insensitive to irradiance⁹⁸ (measured by B.H. Ripin). Figure 3.11 would then indicate that the "fast" ion energy content increases linearly with absorbed laser energy from $\sim 10^{15}$ to $\sim 10^{16}$ W/cm². The fraction of the ion expansion energy transported by energetic ions is therefore not very sensitive to irradiance over this range. The physical meaning of this result is not clear since, as shown in chapter I and IV, the acceleration of energetic ions is dependent both upon the electron temperature and the density gradient.

AD-A057 439

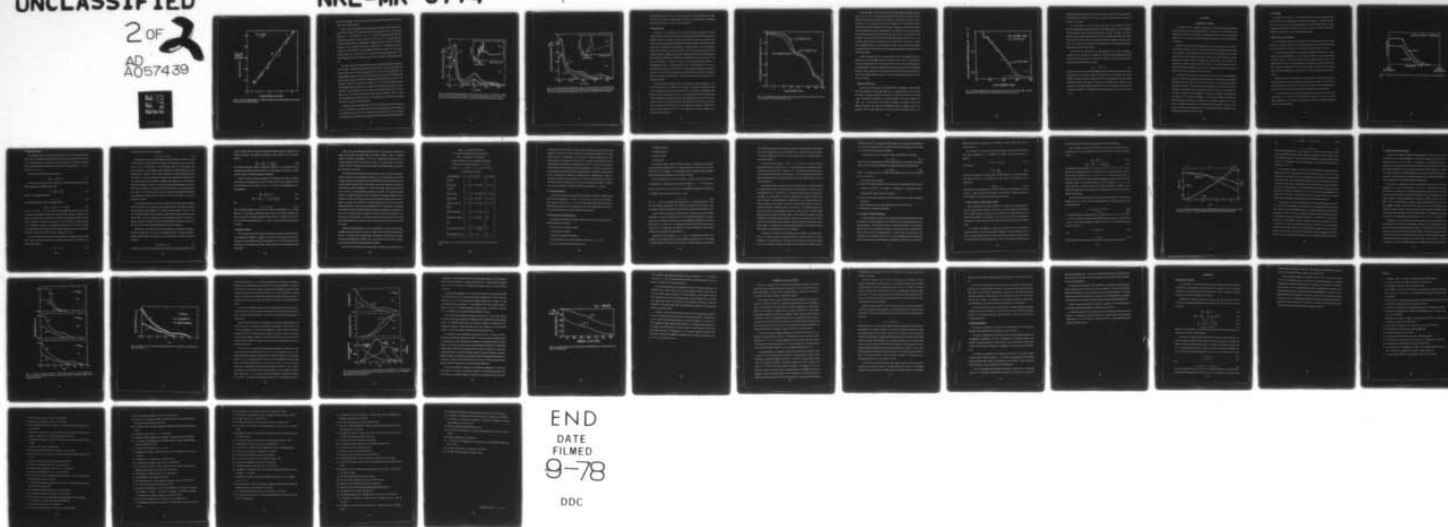
NAVAL RESEARCH LAB WASHINGTON D C
HIGH-ENERGY ION EXPANSION IN LASER-PLASMA INTERACTIONS.(U)
APR 78 R DECOSTE
NRL-MR-3774

F/G 20/9

UNCLASSIFIED

2 OF 2
AD
A057439

NL



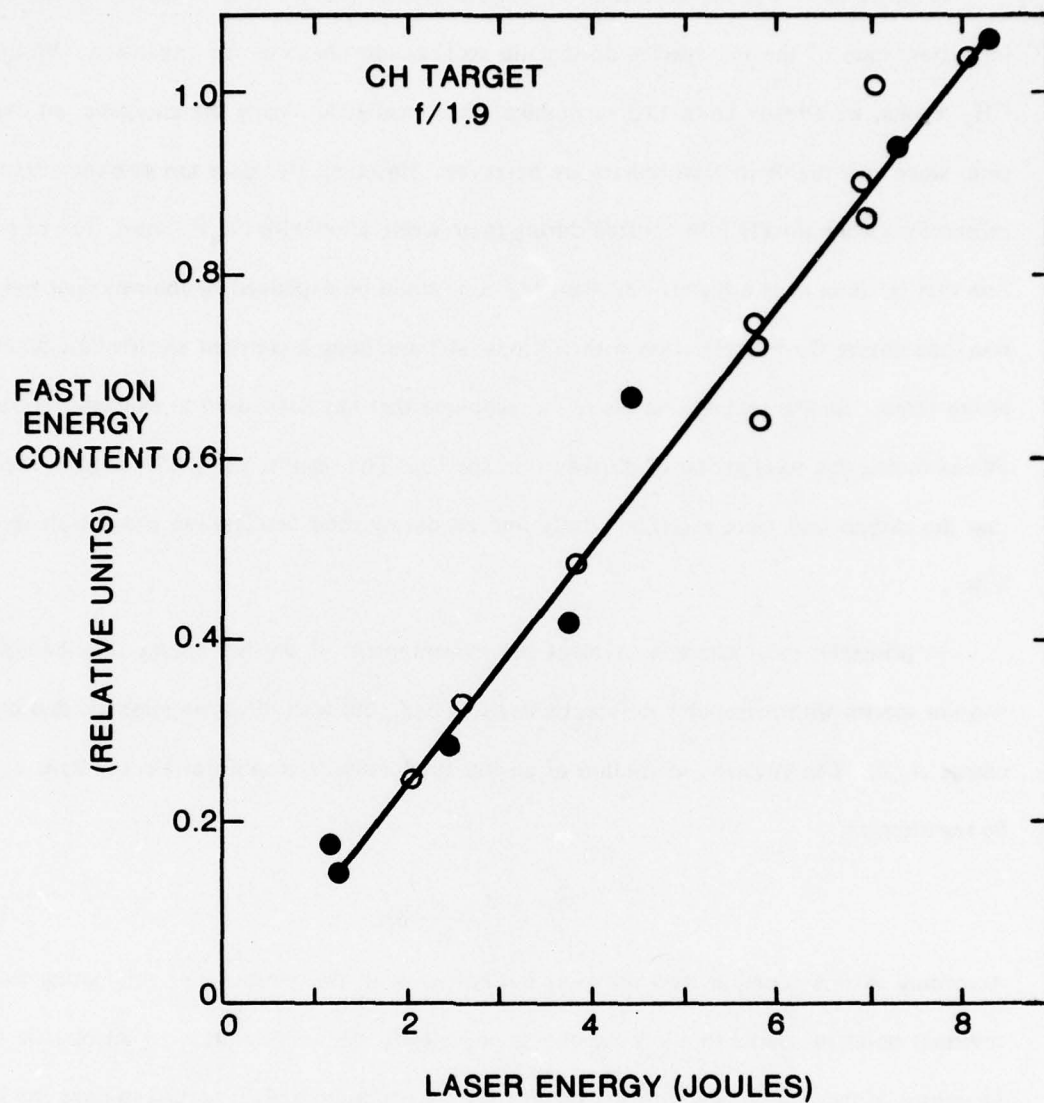


Fig. 3.11. Fast ion energy content as a function of incident laser energy measured at one observation angle with a charge collector.

phase of their expansion. We will see below that the experimental results, obtained with CD_2 targets, yield the same conclusion.

In order to determine the degree of ionization during the expansion of the carbon ions, an extensive series of shots was taken using CD_2 targets under conditions similar to the CH_2 target irradiation, i.e., $\sim 10^{16} \text{ W/cm}^2$ and $\theta_i = \theta_d = 35^\circ$. Typical ion energy distributions with their associated charge collector traces are shown in Fig. 3.12 and 3.13. The special technique involved in obtaining these ion distributions was explained in detail in Chapter II. The small number of H^+ ions, observed in both cases, is consistent with a 3% hydrogen concentration measured in the CD_2 material. The only significant contribution of the H^+ ions to the charge collector signal in Fig. 3.12b (and 3.13b), is the small peak arriving at around 40 nsec. The relative behavior of the H^+ ion with respect to the D^+ and C^{+6} ions will be discussed in Chapter IV.

We now point out some interesting features of the ion energy distributions obtained from the CD_2 targets. One first notices that the multi-peak structures, which were also observed in the CH_n (CH_2 or CH) cases, are still present on the D^+ and C^{+6} energy distributions. One striking difference between the CD_2 and CH_n target is that the D^+ and C^{+6} distributions have almost the same structure, whereas little correlation was observed between the H^+ and C^{+6} distributions. In Fig. 3.12a, the ratio of the number of D^+ to C^{+6} ions remains almost constant with increasing energy. In Fig. 3.13a, the C^{+6} and D^+ ion distributions are similar up to about 200 keV/Z. Above 200 keV/Z, very few carbon ions seem to be associated with the last D^+ peak at 225 keV/Z. Most other shots, taken under the same conditions (4 shots), are cases that fall between those of Fig. 3.12 and 3.13, i.e., the relative number of carbon ions associated with the last D^+ peak varies from shot-to-shot.

Except for the very high energy portion of the ion distributions, the relative behavior of the C^{+6} ion distribution is very similar to the D^+ ion energy distribution and, within experimental uncertainties, the ratio of D^+ to C^{+6} ion number is consistent with a CD_2 target. Therefore, we conclude that the carbon ions were already fully ionized during the acceleration phase of

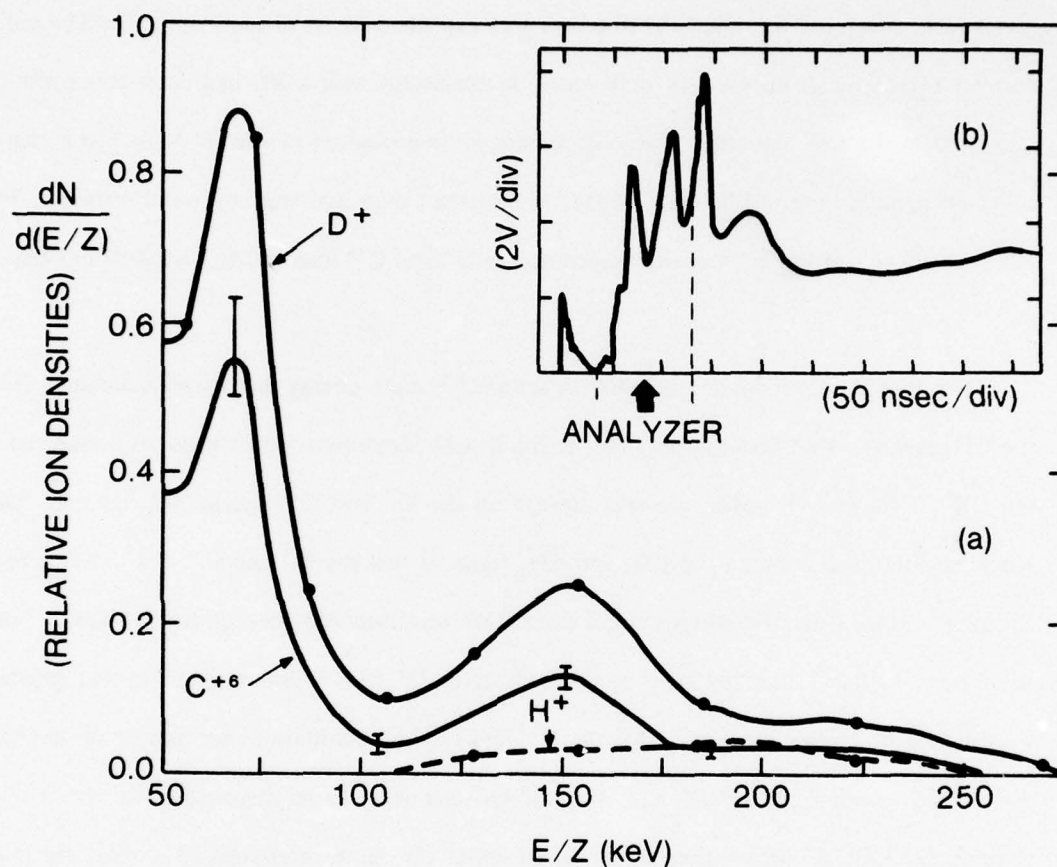


Fig. 3.12. (a) High energy ion distributions from a CD_2 target normal to the analyzer axis. The number of H^+ ions is consistent with a 3% hydrogen concentration measured in the CD_2 material. (b) Oscilloscope trace showing the portion of the trace sampled by the ion analyzer.

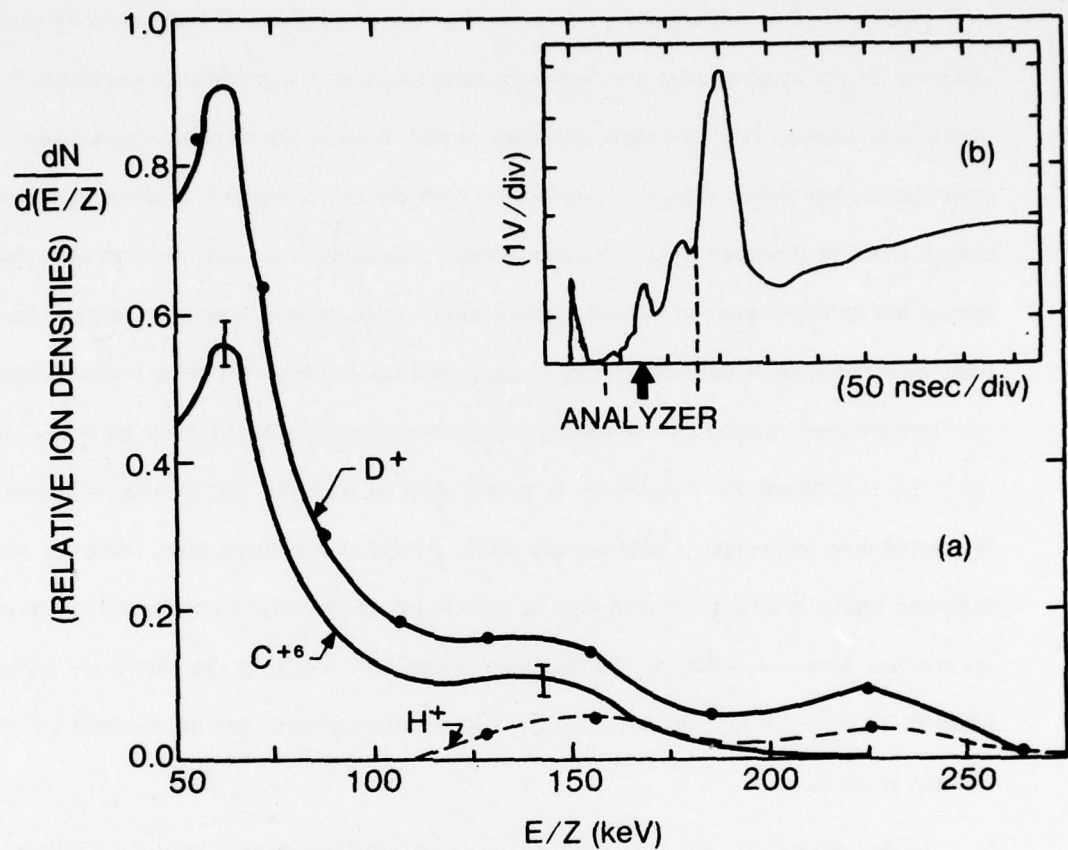


Fig. 3.13. (a) High energy ion distributions from a CD_2 target normal to the analyzer axis. The number of H^+ ions is consistent with a 3% hydrogen concentration measured in the CD_2 material. (b) Oscilloscope trace showing the portion of the trace sampled by the ion analyzer.

their acceleration with the D^+ ions. The same conclusion can also be applied to CH_n targets such that, in the expansion model presented in Chapter IV, ionization effects can be neglected and only two ion species, C^{+6} and H^+ , need to be considered.

B. X-Ray Emission

In Chapter I, it was already pointed out that the observation of energetic ions is indirect evidence for the occurrence of anomalous processes leading to high electron temperature in the underdense region. Heat transport inhibition would increase the electron temperature locally, such that the hot plasma regions are decoupled from the colder regions. Alternatively, the laser energy could be absorbed by a reduced number of electrons such that hot and cold electrons coexist but do not interact in the absorption region. Since, in both cases, the cold and hot electrons emit radiation in different energy ranges, information about the electron temperatures in the laser-produced plasma can be obtained from measurements of the x-ray emission. In this case, the continuum x-ray radiation is mostly due to free-free electron-ion collisions, i.e., bremsstrahlung emission. Unfortunately most current x-ray diagnostics, such as the one described briefly in Chapter II, can only be used to obtain spatially and temporally integrated x-ray spectra. However, since the hot electrons, which emit mostly in the hard x-ray region, are likely to be localized in time and space, a lower-bound estimate can be obtained on the hot electron temperature.

Typical space and time integrated x-ray spectra obtained at high laser irradiance ($\sim 10^{16}$ W/cm²) are shown in Fig. 3.14 (taken by F.C. Young). As explained in Chapter II and Ref. 13, each spectrum was deduced from the response of 15 x-ray detectors with different energy filters, covering the entire energy range. The x-ray measurements were done concurrently with the ion measurements reported in this chapter. The slight differences between the three spectra are due to shot-to-shot reproducibility rather than differences between the target conditions. The x-ray spectra are therefore not sensitive to the target angle with respect to the laser axis, or whether the target material is CH_2 or CD_2 . This suggests that the plasma conditions, for the three cases, were very similar.

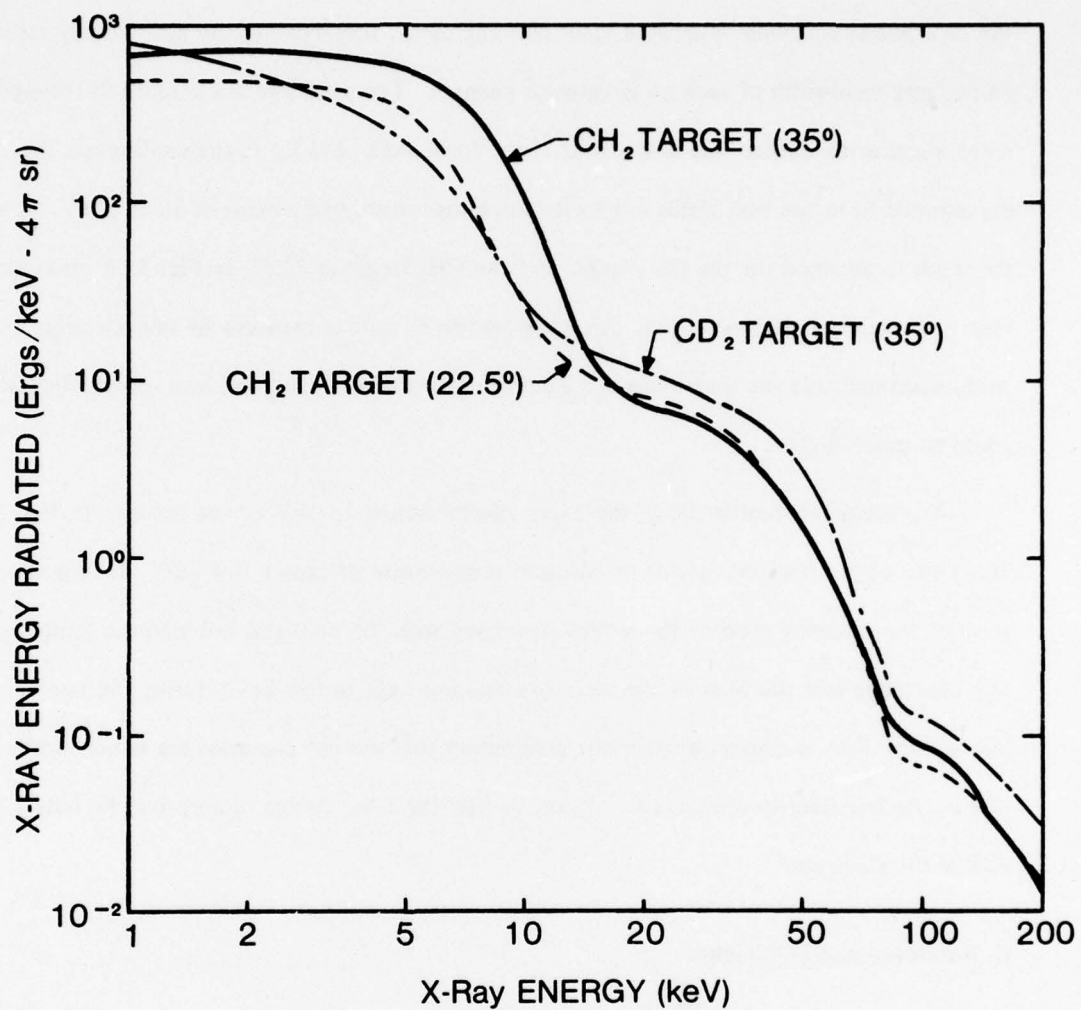


Fig. 3.14. Continuum X-ray spectra from a CH_2 target rotated by 35° and 22.5° , and a CD_2 target rotated by 35° with respect to the laser axis.

At least two groups of electrons can be seen to emit with different characteristic temperatures in Fig. 3.14. The x-ray emission associated with the hot electrons mentioned above is typically observed between 15 and 90 keV on most shots. This portion of the spectra is shown in Fig. 3.15, on a semi-log scale, for the case of a CH₂ target at 35°. The horizontal location of the data points and their associated error bars represent, respectively, the peak energy response and energy bandwidth of each x-ray detector channel. The solid line is a smooth fit through the data, whereas the dashed line is a best fit of the form $\exp(-E/kT_e)$ to the continuous line. The exponential fit to the data yields a hot electron temperature component of 16 ± 2 keV. A similar result is obtained for the CD₂ target and the CH₂ target at 22.5°, in Fig. 3.14. It is important to remember, however, that this temperature is only a measure of one electron energy component and that the maximum hot electron temperature during the laser-plasma interaction could be much higher.

A precise exponential fit of the x-ray spectra below 15 keV is not possible in Fig. 3.14. However, a gross estimate yields an electron temperature of only a few keV. Taking also into account the intensity ratio of the x-rays associated with the cold and hot electron temperature, one concludes that the bulk of the electrons remains cold (a few keV) during the laser-plasma interaction. This is consistent with our assumption that the hot electrons are either locally limited to the low density underdense region, or that the laser energy is absorbed by only a fraction of the electrons.

C. Summary and Discussion

In summary, we have measured the energy distribution of energetic ion species obtained from intense irradiation of plastic targets (CH_n, CD₂). An important fraction of the ion expansion energy is transported by energetic ions with $E/Z > 50$ keV/Z for directions near the target normal. This fraction also appears to be relatively insensitive to the laser irradiance in the range $\sim 10^{15} - 10^{16}$ W/cm² for a given direction of expansion. The energetic ion blow-off is almost fully ionized, which means that recombination effects are negligible during the ion expansion. From the CD₂ target results, we have also shown that ionization effects can be

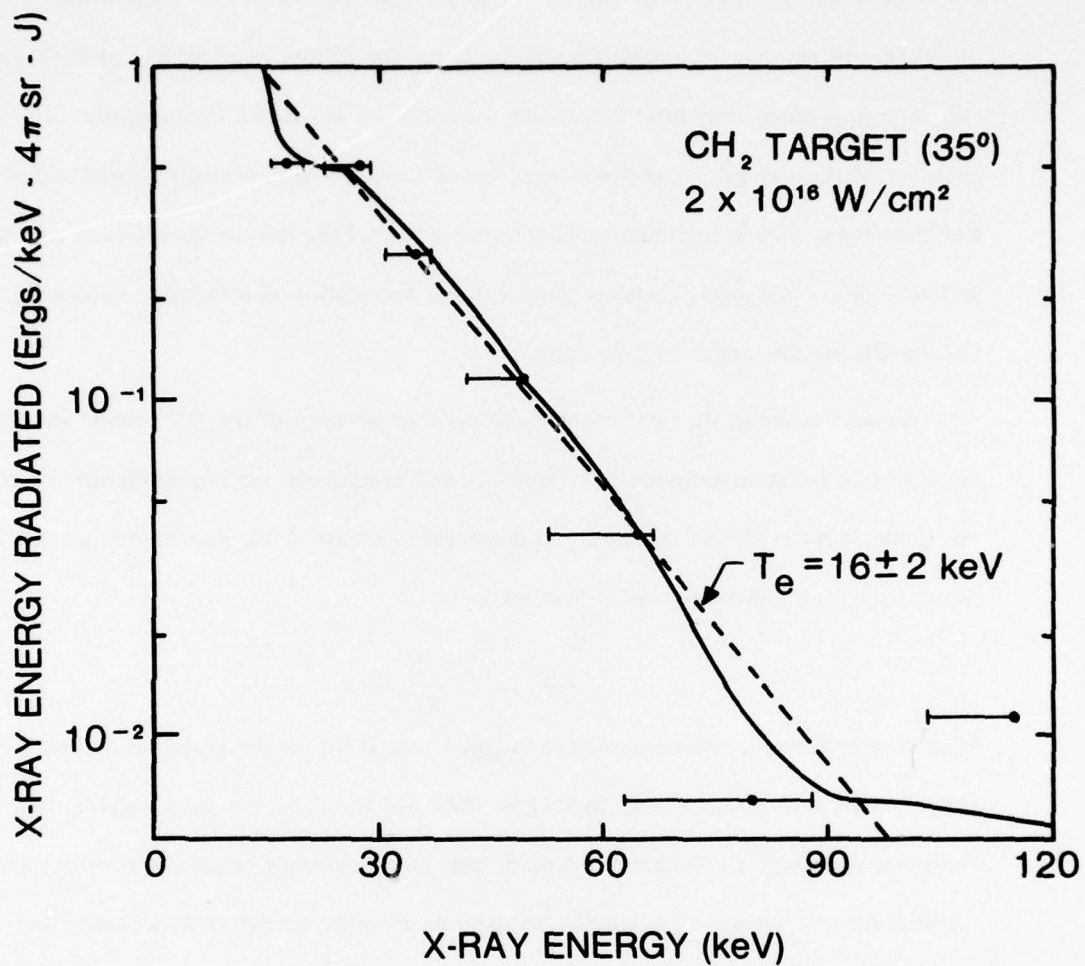


Fig. 3.15. High energy portion of the continuum X-ray spectra from a CH_2 target. The electron temperature is inferred from an exponential fit through the data points.

neglected during the acceleration phase of the ion expansion. The ion expansion can therefore be modeled with two ion species, C^{+6} and H^+ , for the case of a CH_n target, or with one ion species for a CD_n target.

The relative behavior of the C^{+6} and H^+ ion species is also noteworthy. We have observed nonreproducible multipeak structures on the energy distributions of both hydrogen and carbon species, with little correlation between the H^+ and C^{+6} structures. The relative behavior of the ion species indicates that the H^+ ions are preferentially accelerated to higher E/Z than the C^{+6} ions, such that an important fraction of the ion energy is transported by energetic H^+ ions. This result is inconsistent with the assumption of a constant electrostatic potential accelerating the ions to high energies.

As we will see in the next chapter, the relative behavior of the C^{+6} and H^+ ion species is consistent with the assumption of a spatially and temporally varying ambipolar electric field associated with the plasma pressure. As discussed in chapter I, the accelerating electric field \bar{E}_0 associated with the plasma pressure is given by

$$e \bar{E}_0 \approx - \frac{k T_e}{n_e} \nabla n_e. \quad (3.1)$$

Interferometric and x-ray measurements suggest that steep density gradients and high electron temperatures exist at high laser irradiance. We will show, in the next chapter, that electric fields strong enough to accelerate energetic ions can be created, assuming reasonable electron temperature and density scale length. In the case of multi-species plasma expansions, we will also show that an ambipolar expansion accelerates lower A_i/Z_i ion species to higher E/Z than ion species with higher A_i/Z_i , explaining the preferential acceleration of H^+ ions over heavier C^{+6} ions.

CHAPTER IV

THEORETICAL MODEL

In Chapters I and III, we argued that strong electric fields associated with large pressure gradients are likely to exist at high target irradiance. In this chapter, we show how these strong ambipolar electric fields can accelerate ions to high energies consistent with the experimental observations. For that purpose, a simple multi-fluid model has been developed to describe the ion expansion.

Quantitative agreement with the experimental results is not expected due to the simplicity of the model. The model is a 1-D, initial-value problem without laser energy deposition during the ion expansion. Another deficiency of the model is that the fluid representation is marginally valid, due to high electron temperatures, relatively short density gradients and strong ambipolar electric fields. However, the model does provide insight to the acceleration of a small group of energetic ions by a large pressure gradient. The model also demonstrates that multi-species plasmas with different A/Z ions cannot be adequately represented by a single-ion species during the acceleration phase of the ion expansion.

In the first section, we present the fluid model used to describe the multi-species plasma expansion. We first discuss briefly the basic plasma geometry, then describe the fluid equations and, finally, discuss the validity of the model from estimates of the characteristic parameters pertinent to our problem. In the second section, the numerical code that was used to solve the fluid equations is described. For the reader who is content to believe in the numerical code as a "black-box" integrator of the fluid equations, this section may be skipped. More details about this "black box" are also found in Appendix A. In the last two sections, we present some results illustrating the acceleration of energetic ions under different conditions. In the third section, a single-ion species expansion is compared with analytical solutions. Finally, the properties of a multi-ion species plasma expansion are detailed and qualitatively compared with the experimental observations in the fourth section.

A. Fluid Model

The purpose of this section is to provide a specification of the plasma expansion model. First, we outline the basic plasma geometry and specify the parameters of our initial-value problem. Next, we list the system of fluid equations used to model the plasma expansion and discuss the physics treated by, and omitted from, the model. Finally, the validity of this model is addressed by a brief survey of relevant characteristic parameters.

a) Basic Geometry and Parameters

First we briefly summarize the basic geometry and the physical parameters and variables involved in the model. Details about the underlying physical assumptions will be discussed later as we proceed with a discussion of the fluid equations and the validity of the model.

The one-dimensional ambipolar plasma expansion is modeled with either one or two relatively cold ion fluids with different A_i/Z_i . The ion density profiles for this initial-value problem are shown in Fig. 4.1. Initially, both density profiles are specified to have velocities much smaller than final velocities. The left boundary is an impenetrable wall and the plasma expansion is toward the right boundary. A hot electron background component, with an initially uniform temperature throughout the expansion region, is assumed to maintain quasi-neutrality at all times.

The model does not include absorption of the laser energy. We assume that the initial-value problem begins after the laser energy is deposited into hot electrons. Alternatively, the laser energy deposition is assumed to act as a heat reservoir which can supply thermal energy to be converted into ion kinetic energy during the ion acceleration phase of the expansion.

If two ion species are involved, the fluid equations must be solved for the ion and electron densities $n_i (i = 1, 2)$ and n_e , the ion and electron velocities $v_i (i = 1, 2)$ and v_e , and the electron temperature T_e , as a function of time and space. The choice of appropriate boundary conditions will be discussed later.

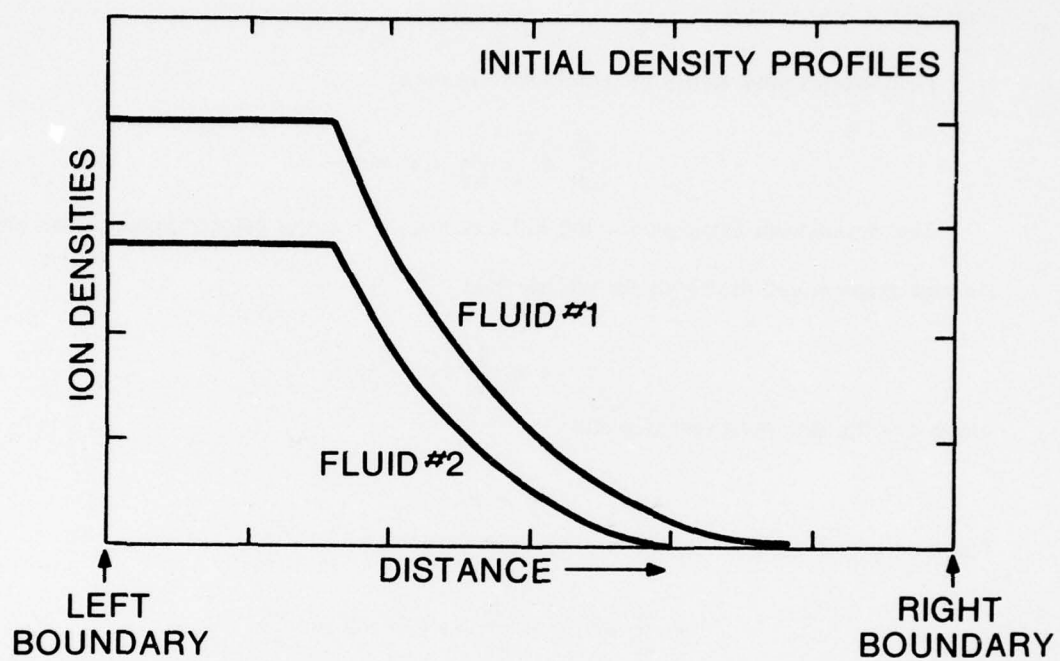


Fig. 4.1. Schematic of the basic geometry and the ion density profiles for our initial-value problem.

b) Fluid Representation

The temporal evolution of the fluid variables is given by the set of standard fluid equations⁴⁰. First, we consider the general case of three species, one electron and two ions which later is simplified for the case of electrons with a single ion species. In the general case, the set of self-consistent equations must describe the time evolution of seven variables: n_α , v_α and T_e , where $\alpha = i, e$ and $i = 1, 2$.

Each species must satisfy the continuity equation

$$\frac{\partial}{\partial t} n_\alpha + \frac{\partial}{\partial x} n_\alpha v_\alpha = 0. \quad (4.1)$$

The momentum equation for the hot electrons is a stress balance between the electron pressure gradient and the ambipolar electric field

$$0 = e n_e \frac{\partial}{\partial x} \phi - \frac{\partial}{\partial x} p_e, \quad (4.2)$$

where ϕ is the ambipolar potential and

$$p_e = n_e k T_e. \quad (4.3)$$

The momentum equation for the two ion fluids is given by

$$m_i \frac{\partial}{\partial t} n_i v_i + m_i \frac{\partial}{\partial x} n_i v_i v_i = -Z_i e n_i \frac{\partial \phi}{\partial x}, \quad (4.4)$$

where $m_i = A_i m_p$ and $i = 1, 2$. In Eq. (4.4), the only interaction between the two ion species is through the self-consistent electric field. Collisional effects have been neglected in this model. As we will see below, the electron-ion collisions can be neglected because of the high electron temperature. An initial ion temperature of a few hundred eV also makes viscosity ($\propto T_i^{-3/2}$) negligible with respect to the ambipolar electric field in Eq. (4.4). The ion temperature, although high enough to neglect viscosity, remains relatively low compared to the electron temperature, so that the ion pressure can also be neglected in Eq. (4.4).

Since we assume that the density gradient scale length is much greater than the electron Debye length, the Poisson equation for the ambipolar potential can be replaced by the quasineutrality condition

$$n_e = Z_1 n_1 + Z_2 n_2, \quad (4.5)$$

or alternatively, by a no-net-current condition

$$n_e v_e = Z_1 n_1 v_1 + Z_2 n_2 v_2. \quad (4.6)$$

An assumption about the electron temperature and the heat flow is required to close the moment equations. In all cases treated in this chapter, the left boundary in Fig. 4.1 is impenetrable, i.e., with $v_i = 0$, and $\partial p_e / \partial x = 0$ at the boundary. Hence, no heat is allowed to flow across that boundary. Three different heat flow assumptions are considered alternatively in the expansion region. Usually, a uniform electron temperature is assumed throughout the expansion region, i.e., the plasma expansion is isothermal. This is equivalent to assuming that the heat is allowed to flow without inhibition throughout the expansion region. This isothermal assumption is divided into two types. In the first, the uniform electron temperature is left constant during the expansion. This assumption will be later referred to as the "constant temperature" condition. In the other type, the total energy is conserved by reducing the uniform electron temperature according to the rate of change of total ion kinetic energy, i.e., an "energy conservation" condition.

The isothermal assumption is based on the belief that the high electron temperature should ensure effective heat transport across the expansion region. For example, the classical (Spitzer) electron thermal conductivity is a strongly increasing function of $T_e (\propto T_e^{5/2})$. However, the electron collision mean free path can be longer than the density scale length at high target irradiance. Thus, the assumptions used to derive classical conductivity are violated. As discussed in Chapter I, alternate heat transport schemes have been modeled, but the heat transport in both the overdense and underdense regions is still not well described.

The third type of heat transport model tried, the antithesis of an isothermal assumption, is the adiabatic assumption. In this case, the ambipolar potential of the plasma expansion is assumed to confine (trap) the hot electrons, i.e., the total energy E of an electron is conserved according to

$$E = \frac{1}{2} m_e v_{th}^2 - e\phi. \quad (4.7)$$

To make sure that the results presented later in this chapter are not drastically affected by our

choice of thermal transport mechanism we modeled the adiabatic expansion in addition to the isothermal conditions. This required the inclusion of a third equation, for the hot electron pressure,

$$\frac{\partial}{\partial t} p_e + \frac{\partial}{\partial x} p_e v_e = -\frac{2}{3} p_e \frac{\partial}{\partial x} v_e. \quad (4.8)$$

The adiabatic assumption yielded no fundamental differences in the qualitative features obtained from the isothermal expansion model. Our two-fluid model is, therefore, not a strong test of the validity of the isothermal expansion assumption.

In Eqs. (4.1)-(4.6), the electron variables can be eliminated in favor of the ion densities and velocities by substituting Eq. (4.5) into (4.1) and Eq. (4.2) into (4.4). Having done so, the time evolution of the 4 ion variables n_i , and v_i ($i = 1, 2$) and p_e can be described by the following equations:

$$\frac{\partial}{\partial t} n_i + \frac{\partial}{\partial x} n_i v_i = 0, \quad (4.9)$$

$$\frac{\partial}{\partial t} n_i v_i + \frac{\partial}{\partial x} n_i v_i v_i = -\frac{Z_i}{A_i} \frac{n_i}{n_e} \frac{1}{m_p} \frac{\partial}{\partial x} p_e, \quad (4.10)$$

and

$$n_e = Z_1 n_1 + Z_2 n_2. \quad (4.11)$$

With an isothermal expansion, Eqs. (4.9)-(4.11) are solved self-consistently for n_i , v_i , with the addition of T_e if the energy conservation condition is used. For the adiabatic expansion case, Eqs. (4.6) and (4.8) are required in addition to Eqs. (4.9)-(4.11). Equations (4.6) and (4.8)-(4.11) are then solved self-consistently for n_i , v_i and T_e , as a function of time and space for all 5 variables.

c) Validity of the Model

We now proceed to examine the validity of this model by means of a brief survey of pertinent characteristic parameters. In general, we find that a fluid description of the plasma expansion is not well justified for high electron temperatures. For this reason and others, discussed below, only semi-quantitative results should be expected from this model (and other fluid models).

Table 4.1 lists some characteristic parameters relevant to a high electron temperature and relatively short density scale length plasma. The results in Table 4.1 apply to a hydrogen plasma at the Nd-laser critical density ($n_c = 10^{+21} \text{cm}^{-3}$). Representative electron and ion temperatures assumed are 25 keV and 500 eV respectively. The initial density scale length is assumed to be 10 μm . While these parameters are realistic, they would probably not all apply to the same place at the same time.

The collision time scales and mean-free paths given in Table 4.1 should be compared to typical ion acceleration times and density scale lengths. The basic requirements for the validity of a fluid model are that the length and time scales of fluid quantities should be greater than the mean-free paths and collision times. Small collision times are also required for the species to be described as approximately Maxwellian. In view of the collision times and mean-free paths given in Table 4.1, these requirements are generally not satisfied. This signals the possible existence of non-Maxwellian electron and ion distributions and imposes limitations upon the validity of our model. The concept of electron and ion temperatures might therefore be meaningless in the present case. However, for convenience (and due to the lack of other suitable plasma descriptions), we make the gross approximation that the ion and electron distributions were initially (and remain) Maxwellian during the expansion. The Maxwellian assumption is not essential for the ions since they are assumed to be cold, and thus the ion temperature is not used directly in our fluid equations. The electron temperature may be thought of as an average particle energy assigned to the electrons in order to define an electron pressure that can be used in the model.

Although the fluid representation is often not well justified, our choice of terms representing different physical processes in the model is consistent with the characteristic parameters of Table 4.1. For example, since the Debye length is much shorter than the density scale length, the quasi-neutrality assumption is justified. Also, the large electron mean-free path to gradient scale length ratio justifies the isothermal atmosphere assumption.

Since the ion-ion collision time and mean-free path are larger than the characteristic ion

Table 4.1 — Characteristic Parameters.

The results and quantities are expressed in psec for

times, μm for lengths, cm^{-3} for densities,

cm/sec for velocities and eV for temperatures and energies.

The results in the fourth column are for $T_e = 25 \text{ keV}$,

$T_i = 500 \text{ eV}$, $n_i = n_e = 10^{21} \text{ cm}^{-3}$, $A = Z = 1$ and $L = 10 \mu\text{m}$ is

the initial density scale length.

Electron thermal velocity	$v_{th, e}$	$7.3 \times 10^7 \sqrt{T_e}$	1.1×10^{10}
Ion thermal velocity	$v_{th, i}$	$1.7 \times 10^6 \sqrt{T_i/Z}$	3.8×10^7
Sound speed	C_s	$9.8 \times 10^5 \sqrt{Z T_e/A}$	1.5×10^8
Debye length	λ_D	$7.4 \times 10^6 \sqrt{T_e/n_e}$	3.7×10^{-2}
Electron mean-free path	λ_e	$2.5 \times 10^{16} T_e^2/Z^2 n_i$	1.5×10^4
Ion mean-free path	λ_i	$2.5 \times 10^{16} T_i^2/Z^4 n_i$	6.5
Electron-ion collision time ¹	τ_{ei}	$3.4 \times 10^{16} \frac{T_e^{3/2}}{Z^2 n_i}$	130
Ion-ion collision time ¹	τ_{ii}	$1.5 \times 10^{18} \frac{A^{1/2} T_i^{3/2}}{Z^4 n_i}$	17
Ion acceleration time	τ_{ac}	$10^8 L/C_s$	6.6

1. I.P. Shkarofsky, T.W. Johnston and M.P. Bachynski, "The Particle Kinetics of Plasma", Addison-Wesley (1966).

acceleration time and the density scale length, ion-ion collisions and viscosity effects can be neglected in the model. This lack of collisions and viscosity allows separation of the charge species during the acceleration phase of the expansion. Otherwise, different species would expand together with a single center of mass velocity⁹⁹. A regime of target irradiance for which viscosity effects were dominant was considered in Ref. 100. It is to be noted that the lack of ion-ion collisions is also inconsistent with a fluid representation. For instance, a strong ambipolar electric field can narrow the thermal ion energy distribution,⁵ resulting in an effective cooling of the ions during the expansion and a possible increase in collisional effects. However, it has also been argued that the ion temperature T_i in the ion-ion collision and the ion mean-free path formulae should be replaced by the actual ion kinetic energy of expansion³⁹, increasing these quantities furthermore and offsetting the effective cooling effect on the viscosity.

B. Computational Model

The system of equations describing the plasma expansion is solved with a numerical code. Given the five major variables n_i , v_i and T_e ($i = 1, 2$) at time t on a mesh, the code calculates their values on that mesh at time $t + \Delta t$. First, we describe the numerical treatment of the system of fluid equations given in the previous section. Next, the technique used to infer asymptotic ion energy distributions from the numerical results is presented.

a) Numerical Solution of Fluid Equations

In this section, we describe the numerical code used to solve the set of equations and conditions described in the last section.

To run the code it is necessary to specify:

- a) initial mesh point locations;
- b) Eulerian or Lagrangian hydrodynamics;
- c) initial distribution of the 5 major variables on that mesh (n_1 , n_2 , v_1 , v_2 , T_e);
- d) ion atomic masses and charge numbers A_i and Z_i ;

- e) boundary conditions;
- f) heat flow condition;
- g) time step control;
- h) output control.

The numerical model is coded in Fortran IV and runs on the NRL Texas Instrument Advanced Scientific Computer (ASC). In a typical 30 seconds run (CPU time) on the ASC, 500 timesteps can be integrated. A rather general facility for handling the time integration modules and the plotting subroutines is also provided on the ASC.

The computational mesh is a 1-D cartesian system. There are N cells and their positions at the beginning of a numerical timestep are denoted by $\left\{r_n^o\right\}$ ($n = 1, \dots, N$). The location of each cell corresponds to the center of the cell. For a Lagrangian representation, the grid points are at $\left\{r_n^f\right\}$ at the end of a timestep of duration Δt . Here

$$r_n^f = r_n^o + v_{n,i} \Delta t \quad (4.12)$$

for $n = 1, \dots, N$ and i can represent either ion fluid (1 or 2). The grid displacement $v_{n,i} \Delta t$ is zero for an Eulerian representation. The initial grid point spacing is initially constant in both the Lagrangian and Eulerian representations (and, obviously, remains fixed in the Eulerian case).

Typical, 200 cells are used with a spatial resolution of 25 grid points per density gradient scale length L . In order to minimize the loss of ions through the right boundary, the code is usually run in a sliding-zone mode where the mesh displacement corresponds to the heavier fluid motion i.e., the code is run in a Lagrangian mode with the mesh moving at the heavier fluid's velocity. The lighter fluid, with higher velocity than the heavy fluid, is then convected through the mesh according to the fluid equations.

Initially, the 5 major variables n_1, n_2, v_1, v_2 and T_e are specified for each mesh point. Typically ion density profiles for our initial-value problem were shown in Fig. 4.1. The length of the plateau density is the same for both ion species. The density gradients are exponentials

with the same scale length for both ion species. Initially, both density profiles are also specified with a velocity negligible with respect to the final velocities. Although not completely unrealistic, these initial profile shapes are chosen for convenience rather than as an ideal representation of laboratory conditions.

Given the five major variables n_i , v_i and T_e ($i = 1, 2$) at time t on a mesh, the code calculates their value on that mesh at time $t + \Delta t$. The time integration is performed using the latest flux-corrected-transport (FCT) techniques^{102, 103}. The underlying algorithm gives fourth-order accurate phases and minimum residual diffusion. The time integration modules used for solving generalized continuity equations have been extensively described elsewhere¹⁰³ and will not be discussed here.

The boundary conditions should be chosen such that the physics of the plasma expansion is not affected by the choice of boundary conditions. The left boundary was chosen to be an impenetrable wall with $v_i = 0$ and $\partial p_e / \partial x = 0$, simulating a plasma created at the surface of a thick target. The right boundary is a perfectly absorbing wall which should not affect the free plasma expansion by creating compression or rarefaction waves on the density profiles due to improper mismatch at the boundary. The initial exponential density profiles are assumed to decrease exponentially to infinity beyond the right boundary. The solutions presented in the next section, however, are not affected by the right boundary as long as the density profile remains exponential just before the right boundary. If this condition is not satisfied, numerical instabilities are created which quickly propagate throughout the computational mesh. We will see in the next section under what conditions the plasma profile remains exponential in the low density region. The details about the numerical implementation of the "perfectly absorbing wall" condition at the right boundary are given in Appendix A.

As discussed in the last section, three different heat flow conditions can be selected for a given run. In the first model, the electron temperature is simply left constant and uniform throughout the computational mesh. The second model conserves the total energy, thermal plus ion kinetic energy, by reducing the uniform electron temperature throughout the mesh

according to the total rate of change of ion kinetic energy. In the third case, the pressure equation is solved self-consistently with the momentum and continuity equation for the variables T_e , which then becomes space and time dependent.

The only requirement on the time step Δt is that, at all times and for all the cells,

$$v_i \Delta t < \Delta x / 2, \quad (4.13)$$

where v_i and Δx are respectively the ion velocity and the cell size. In order to optimize the calculation time, Δt is continuously updated at the beginning of each new timestep such that

$$\Delta t = f \Delta x / 2 v_i, \quad (4.14)$$

where f is a constant less than one. Typically, 100 timesteps are required per ion acceleration time τ_{ac} (see Table 4.1).

The output of each run includes:

- a) graphs of the following quantities as functions of space at predetermined times during the expansion: ion densities n_i , ion velocities v_i , ion energies $\frac{1}{2} m_i v_i^2$, thermal and ion kinetic energy densities, respectively $\frac{3}{2} n_e k T_e$ and $\frac{1}{2} n_i m_i v_i^2$;
- b) tables of the mesh point locations with the above quantities plus the electron temperature and velocity;
- c) tables of the mass, momentum and energy balances as functions of time; and,
- d) warnings and error diagnostics if applicable.

b) Asymptotic Ion Energy Distributions

In order to compare the results from the numerical model with the experimental results, the asymptotic ion energy distributions must be inferred from the numerical solution of set of the fluid equations. To calculate this, we have to assume that the behavior of the expanding plasma long after the ion acceleration has ended, can be determined from a simulation following no more than a few ion acceleration times τ_{ac} . As we will see in the next section, this assumption is not unreasonable, since after only a few ion acceleration times the large pressure gradient responsible for the ion acceleration is quite reduced. Therefore, the ion velocities of

different fluid elements on the mesh can be assumed to remain constant after a few ion acceleration times τ_{ac} .

The calculation of the asymptotic ion energy distribution is relatively simple (the technique was first suggested by D.G. Colombant). We consider J energy intervals ΔE , the j_{th} defined as

$$(j-1)\Delta E \leq E_i \leq j\Delta E, \quad (4.15)$$

and centered on

$$E_j = \left(j - \frac{1}{2} \right) \Delta E. \quad (4.16)$$

The choice of ΔE determines the resolution of the energy distribution. For each fluid element on the mesh, we add to the j_{th} energy group $n_j \Delta x$ ions, where Δx is the cell size and j the integer part of

$$(E_i / \Delta E) + 1. \quad (4.17)$$

The asymptotic ion energy distribution is reconstructed from the J energy groups with average energies E_j . Smooth energy distribution graphs can be obtained by increasing ΔE since the statistics depends on the number of mesh points per energy group.

C. Analytic Single-Ion-Species Expansion Model

Before considering multi-ion-species expansions, it is useful to look at some general properties of single-ion-species expansions. For the case of a constant, uniform electron temperature, the single-ion-species expansion can also be described by analytical solutions valid in different spatial regions of the expansion. These solutions can be used to understand the consequences of a particular choice of initial conditions on the results from the ion acceleration model.

It is noteworthy that different ion species with the same A/Z can also be effectively modeled with a single ion species, as discussed in Chapter III. The energy distributions of C^{+6} and D^+ ion species obtained using a CD_2 target were shown to be similar in shape, in Chapter III. We also modeled the plasma expansion of C^{+6} and D^+ ion species and found the results to

be the same than those obtained from a single species expansion discussed below.

We now consider the expansion of a single-ion species of charge Z and atomic mass A for the isothermal case with a constant and uniform electron temperature. The system of equations reduces to

$$\frac{\partial}{\partial t} n + \frac{\partial}{\partial x} n v = 0, \quad (4.18)$$

$$\frac{\partial}{\partial t} n v + \frac{\partial}{\partial x} n v v = -\frac{Z}{A} \frac{k T_e}{m_p} \frac{\partial}{\partial x} n, \quad (4.19)$$

The initial density profile is given by $n = n_0 \exp(-x/L)$ for $x \geq 0$, and $n = n_0$ for $x \leq 0$, as illustrated by the dashed line in Fig. 4.2. The evolution of the velocity and density profiles are shown in Fig. 4.2. (solid line) at $t = 2\tau_{ac}$, where $\tau_{ac} = L/C_s$. For convenience, in Fig. 4.2, the distances, densities and velocities have been respectively normalized to the initial density profile scale length L , the initial plateau density n_0 and the sound speed C_s . At $t = 2\tau_{ac}$, the density profile can be divided into three distinct regions characterized by different density profile scale lengths and velocities. Region II is expanding further to the right and left as the expansion time increases.

We now proceed with a discussion of the analytical solutions pertinent to the three regions identified in Fig. 4.2. With the initial conditions given above, an analytical solution to Eqs. (4.18) and (4.19) is⁶⁶

$$n = n_0 \exp(-x/L + C_s^2 t^2 / 2L^2), \quad (4.20)$$

$$v = C_s^2 t / L \quad (4.21)$$

In a reference frame having acceleration C_s^2/L , the solution becomes $n = n_0 \exp(-x/L)$ and $v = 0$. Thus, the analytic solution describes a profile maintaining its shape as it accelerates at a rate C_s^2/L . This solution corresponds to region III in Fig. 4.2. If the initial conditions were instead (for positive x)

$$n = n_0 \exp(-x/L), \quad (4.22)$$

and

$$v = x C_s / L, \quad (4.23)$$

then the solution to Eqs. (4.20) and (4.21) would have been the self-similar solution⁶⁴⁻⁶⁵

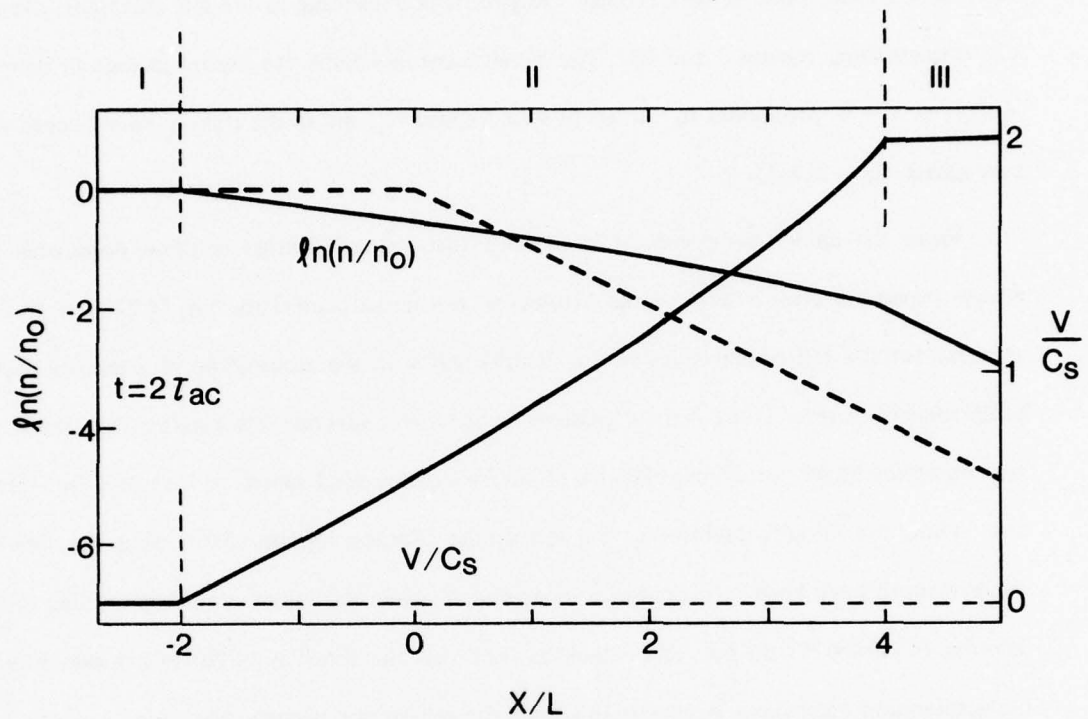


Fig. 4.2. Normalized density and velocity profiles initially (dashed lines) and at a time $2\tau_{ac}$ (solid lines), where τ_{ac} is the initial density scale length divided by the sound speed.

$$n = n_0 \exp\left[-(x - C_s t)/(L + C_s t)\right], \quad (4.22)$$

and

$$v = C_s(x + C_s t)/(L + C_s t). \quad (4.23)$$

Within the expanding region II, it can be seen that the solution is almost self-similar (linear velocity and logarithmic density profile). Region II is expanding to the left and right, eventually extinguishing regions I and III. The signal communicating the abrupt change in density, initially at $x = 0$, propagates to the left at sound speed C_s , and to the right at sound speed plus flow speed, $C_s + C_s^2 t/L$.

From the above discussion, it is obvious that the self-similar solution dominates the plasma expansion after a certain time. However, the initial conditions, Eq. (4.22) and (4.23), assumed for the self-similar solution are inconsistent with the assumption of a density profile accelerated from rest. If the density gradient extends over several scale lengths, then these initial conditions imply initial ion velocities of several times sound speed, or ions that are already fast. Thus, the initial conditions or the self-similar solution require some strong acceleration mechanism to have been in operation prior to $t = 0$, while the initial conditions leading to the solution (4.20)-(4.21) do not. We conclude then that the solution (4.20)-(4.21) can provide the acceleration mechanism necessary to launch the self-similar plasma expansion.

The assumption of an initial density gradient at rest of exponential form is rather arbitrary. From the above discussion, it can be seen that other initial density profile shapes could also be used to launch the self-similar solution. The exponential profile was in fact chosen for convenience. It allows us to find a set of simple self-consistent right hand boundary conditions for the numerical simulation, as explained in Appendix A. For the case of two ion fluids discussed next, the three different regions of expansion are still observed, although in region II, the solution has no longer the self-similar form of Eqs. (4.22)-(4.23), due to the interaction between the two ion fluids. However, initial exponential density profiles are still used to launch solutions in region II, which decouple from the exponential profiles propagating in region III. Most of the physics discussed about the interaction of two ion fluids will be restricted to region

II.

D. Multi-Species Plasma Expansions

In this section, we consider multi-species plasma expansions with emphasis on the interaction between two ion species with different A_i/Z_i during the expansion. The case of two ion species with the same A_i/Z_i was shown to be equivalent to a single-species expansion in Chapter III. The results obtained from the fluid model described in the first half of this chapter are compared qualitatively with the experimental observations reported in Chapter III. Because of the model's limitations, quantitative agreement of the theoretical model with the experimental results is not expected. However, the model does provide useful insight about large electron pressure gradients as an acceleration mechanism for energetic ions.

Since most of our experimental results were obtained from CH_2 targets, we restrict our discussions to a C^{+6} and H^+ plasma with a H^+ to C^{+6} ratio of 2. The assumption of fully ionized carbon ions is consistent with experimental observations presented in Chapter III which show that the carbon ions were fully stripped during and after the acceleration phase of the plasma expansion. The density profiles for our initial-value problem are shown in Fig. 4.3. Both C^{+6} and H^+ density profiles have initially the same exponential scale length L and a velocity negligible with respect to the final velocities. Again, in Fig. 4.3 and the remainder of this section, the distances, densities, velocities and times have been respectively normalized to the initial density profile scale length L , the initial plateau density n_o for hydrogen, the hydrogen sound speed C_s and the hydrogen ion acceleration time τ_{ac} [$\tau_{ac} = L/C_s$, $C_s = (kT_{eo}/m_p)^{1/2}$].

We first look at the time evolution of the density profiles for two cases with different heat flow assumptions. In both cases the total energy is conserved. In the isothermal assumption case, the total energy is conserved during the expansion by reducing the electron temperature according to the total rate of change of ion kinetic energy. The adiabatic expansion is solved with Eq. (4.8) which gives the temporal and spatial evolution of the hot electron temperature. The density profiles for the isothermal case are shown in Fig. 4.3 b and c after $2.4 \tau_{ac}$ and $3.6 \tau_{ac}$ respectively. In Fig. 4.4, the density profiles for an adiabatic expansion are compared with

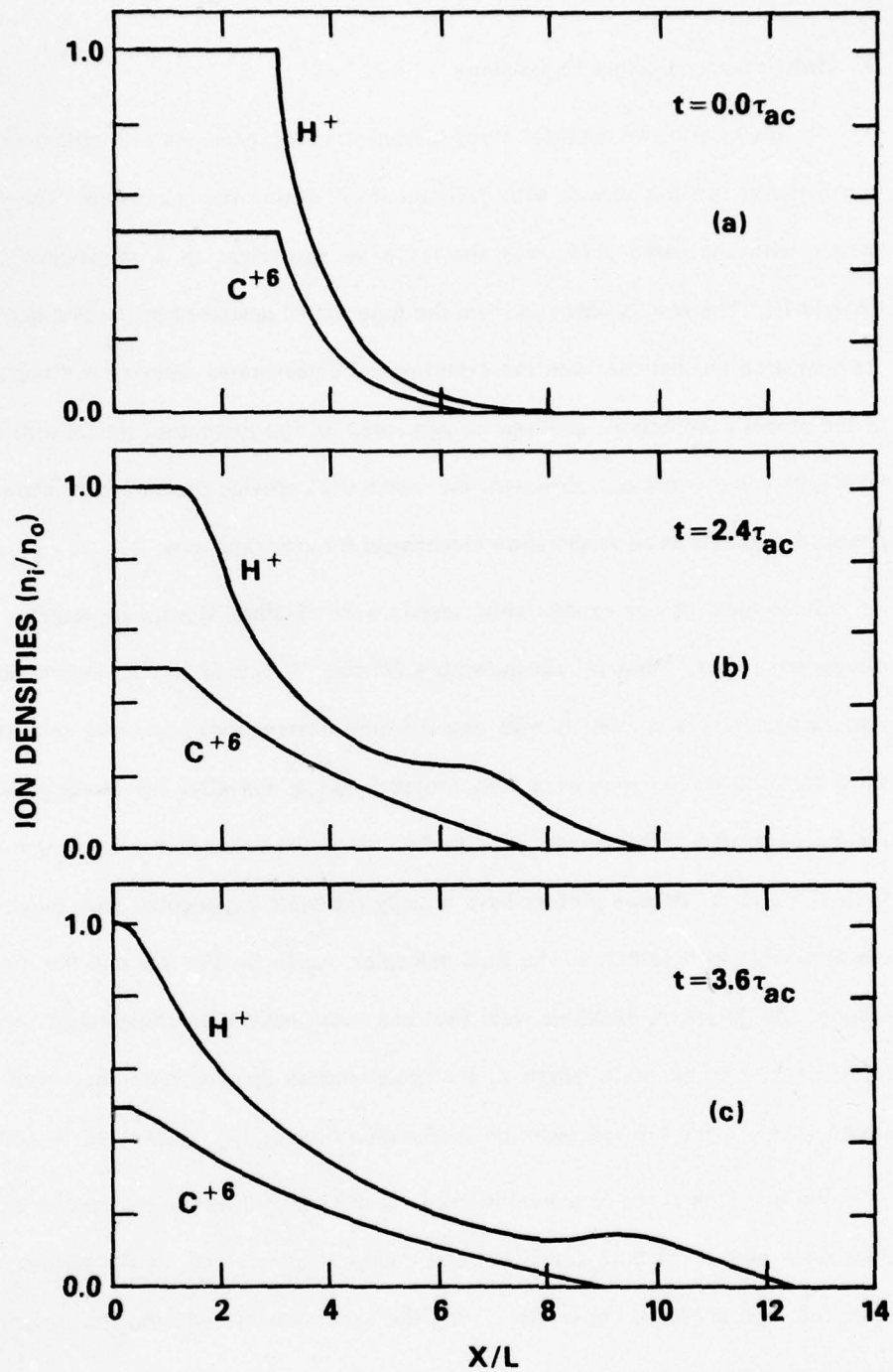


Fig. 4.3. (a) Initial ion density profiles. (b) Profiles after a time $2.4\tau_{ac}$, and (c), after $3.6\tau_{ac}$. The characteristic ion acceleration time τ_{ac} is the initial density scale length divided by the hydrogen sound speed.

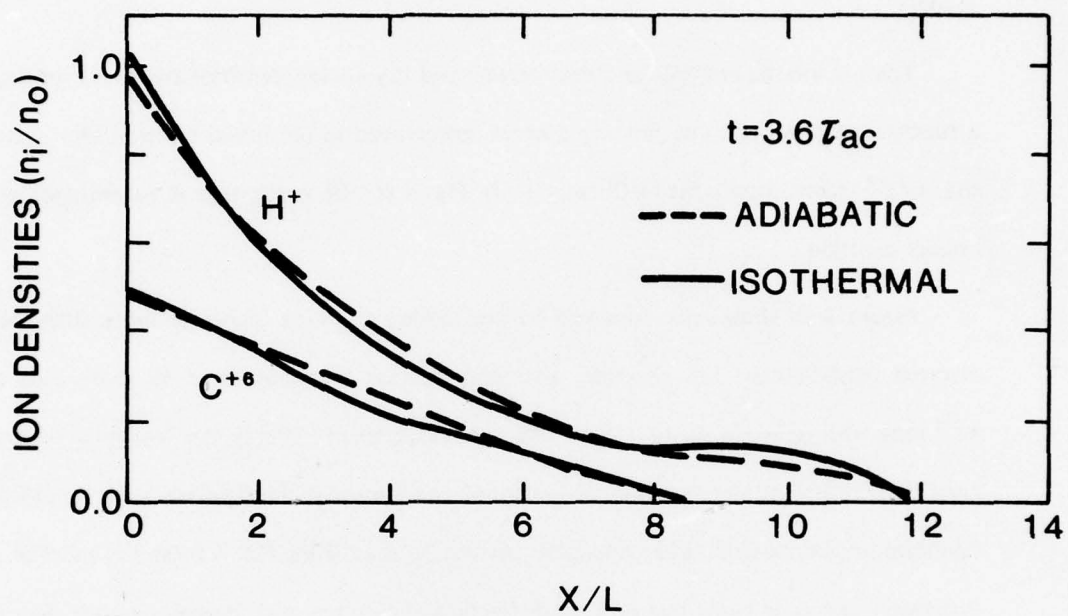


Fig. 4.4. Comparison of the ion density profiles obtained from an adiabatic and an isothermal expansion after $3.6 \tau_{ac}$.

the isothermal results at $3.6 \tau_{ac}$. Aside from small differences in the shape of the profiles, the qualitative features discussed below are not affected by the heat flow assumption. A more accurate treatment of the heat flow during the expansion would probably yield density profiles somewhere between the solid and the dashed lines in Fig. 4.3. We conclude that our two-fluid model is not a strong test of the validity of an isothermal or adiabatic expansion assumption. In the remainder of this section we will mostly discuss the results from the isothermal expansion model.

The ion kinetic energies and the thermal and ion energy densities are shown in Fig. 4.5 as a function of distance. The ion energies are normalized to the initial electron temperature and the A_i/Z_i^2 factor introduced in Chapter I. In Fig. 4.5c, the percentage in parentheses gives the energy partition.

Figure 4.5b shows that ions can be accelerated to much higher energies than the initial electron temperature. For example, an initial electron temperature of 30 keV yields H^+ and C^{+6} ions with energies up to 150 to 450 keV respectively. Using the "constant temperature" condition instead of the "energy conservation" condition for the heat transport would increase *furthermore the maximum ion energies*. As can be seen from Fig. 4.5b and c, most of the ion expansion energy is contained in a small fraction of the ions with energies higher than the initial electron temperature.

From Fig. 4.5, one can also see that, although the acceleration time was about the same for both ion species, the electric field was not. The H^+ ions, being faster, can get to the stronger electric field region and take advantage of the pressure gradient set up by the slower moving C^{+6} ions. The acceleration of H^+ ions by C^{+6} ions is responsible for the bump appearing on the H^+ density profiles around $x \approx 10 L$ in Fig. 4.5a. For $x < 10 L$, the C^{+6} ions contribute most of the electrons to the electron density gradient, whereas for $x > 10 L$, the pressure gradient is mostly controlled by the increased number of H^+ ions. Between the plateau density region and $x < 10 L$, a relatively large pressure gradient is therefore maintained by slow moving C^{+6} ions. Because of their higher velocities, the H^+ ions produced from the pla-

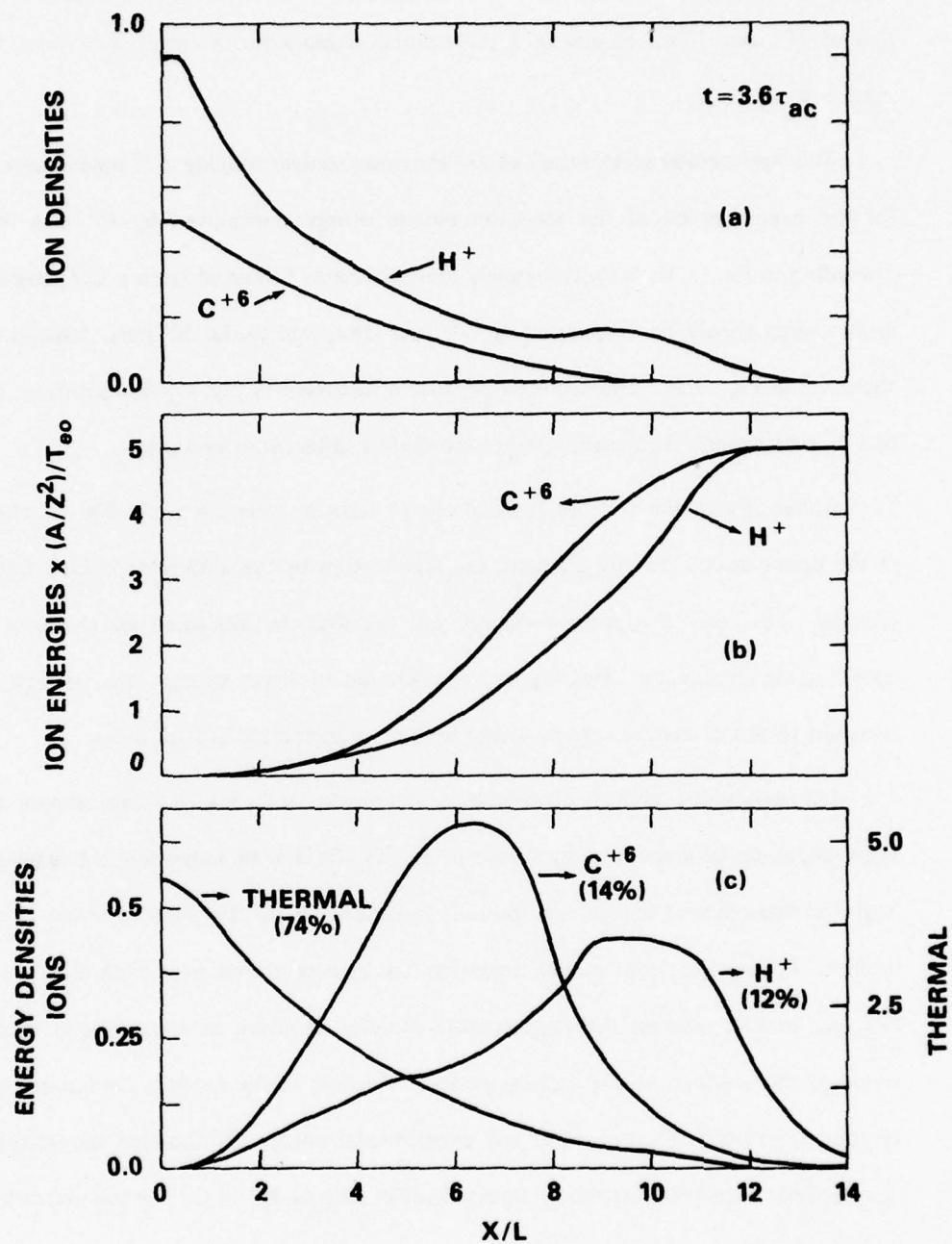


Fig. 4.5. Ion densities, ion energies, and energy densities versus distance at $t = 3.6 \tau_{ac}$ (τ_{ac} is the initial density scale length divided by the hydrogen sound speed). The percentages in parentheses give the energy partition.

teau region are quickly accelerated through this large pressure gradient until they reached a region where the acceleration is no longer controlled by the C^{+6} ions but rather by accumulation of H^+ ions. This results in a preferential acceleration of lower A_i/Z_i ions over higher A_i/Z_i ions.

This preferential acceleration of H^+ ions over slower moving C^{+6} ions is also responsible for the large fraction of the total ion kinetic energy transported by H^+ ions in Fig. 4.5c. According to Eq. (1.3), for a completely ionized plasma produced from a CH_2 target, 1.5 times more energy should be transported by C^{+6} ions compared to the H^+ ions. Instead, the ratio is about 1.2 in Fig. 4.5c. The adiabatic expansion discussed in Fig. 4.3 also yields an energy ratio of 1.2, even though the density profiles are slightly different in this case.

About 75% of the electron thermal energy remains after $3.6 \tau_{ac}$ in Fig. 3c when, because of the much weaker density gradient, ion acceleration by the ambipolar electric field is greatly reduced. The remaining thermal energy will therefore be dissipated via channels other than energetic-ion production. Heating and acceleration of lower energy ions, as well as thermal transport to denser plasma regions would become predominant at later times.

The asymptotic energy distributions, calculated from Fig. 4.5, are shown in Fig. 4.6 assuming an initial electron temperature of 30 keV. It is to be noted that the detailed structure in the asymptotic ion energy distributions is dependent on the detailed shape of the density profiles. For instance, our model treats the low density plasma expansion as an exponentially decaying profile, whereas the experimental situation involves an expansion in vacuum which would probably affect the exponential profiles. Because of the model's limitations, quantitative agreement between the theoretical and experimental energy distributions should therefore not be expected. However, the model shows that the ratio of H^+ to C^{+6} ions is increasing with ion energy, in qualitative agreement with the measured energy distributions.

A typical ion acceleration timescale for an initial electron temperature of ~ 30 keV and scale length of a few microns is a few tens of picoseconds. The relatively high electron temperature required to accelerate energetic ions has then to be maintained for only a short time

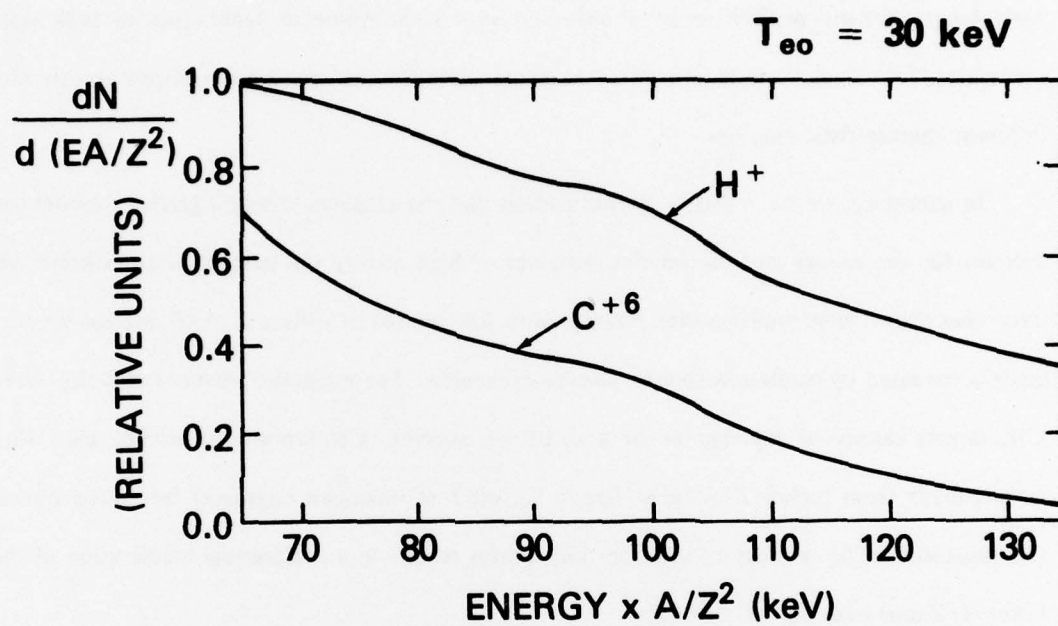


Fig. 4.6. Asymptotic high energy ion distributions calculated from Fig. 4.5 using a 30 keV initial electron temperature.

and is therefore a peak temperature consistent with other simulations.^{38, 53, 59} It is noteworthy that, since $\tau_{ac} \propto L/\sqrt{T_e}$, an increased density scale length can accelerate energetic ions only if a high T_e is maintained over a longer period of time.

The multi-peak structure on the experimentally observed ion energy distributions is not reproduced by our model. However, since the ion acceleration timescale is shorter than the laser pulse length, temporal variations of the pressure gradient on the timescale mentioned above could give bursts of ions of decreasing energies. Another possibility involves the multi-scale length density profiles recently observed with interferometric techniques at high laser intensities.^{60, 61} Each scale length might be responsible for the acceleration of ion groups with different characteristic energies.

In summary, we have shown in this section that the electron pressure gradient model can account for the energy and the relative behavior of high energy ion species. Furthermore, we have also shown that multi-species plasmas with ion species of different A/Z , cannot be adequately modeled by single-ion-species plasma expansion. For example, plasma expansion from CH_n targets cannot be represented by a single ion species. Caution should also be used with targets made from higher Z material (glass, Al, etc.) of unknown degree of ionization during the expansion. The mixture of different ion species results in a preferential acceleration of the lower A/Z ions over higher A/Z ions.

SUMMARY AND CONCLUSIONS

This work is concerned with an experimental and theoretical investigation of the high energy ions produced at high laser irradiance of solid targets. The major conclusion is that the large pressure gradients, believed to exist at high laser intensity, can account for the observed ion energies and the relative behavior of high energy ion species.

A high energy ion analyzer, used to measure the energy distribution of the energetic ion species, was described in Chapter II. The simple electrostatic multi-channel time-of-flight ion analyzer was optimized to study high energy ion species expanding from a laser-produced plasma. For this application, moderate species and energy resolution over a wide dynamic energy range are desirable. The analyzer was designed to achieve a dynamic energy range from 1 to 1000 keV/Z with a 10% species and energy resolution. The calibration of the ion detection system used in the analyzer involved the measurement of secondary electrons emitted from the detector surface upon the arrival of an ion. The secondary electron emission coefficients for hydrogen and carbon ions striking "gassy" copper surfaces were presented in Chapter II.

A technique for measuring energy distributions of ion species with the same A_i/Z_i but different Z_i was also described in Chapter II. This technique was used to measure the energy distributions of C^{+6} and D^+ ion species produced from a CD_2 target at high laser intensity. The technique uses charge exchange of the C^{+6} ions with nitrogen gas in the target chamber. The resulting lower ionization stages than C^{+6} can be differentiated from the D^+ ions.

The energy distribution of energetic ion species obtained from intense irradiation of plastic targets (CH_n , CD_2) were presented in Chapter III. An important fraction of the ion expansion energy is transported by energetic ions with $E/Z > 50$ keV/Z for directions near the target normal. This fraction also appears to be relatively insensitive to the laser irradiance in the range $10^{15} - 10^{16}$ W/cm² for a given direction of expansion. The energetic ion blow-off is almost fully ionized, which means that recombination effects are negligible during the ion expansion. From the CD_2 target results, we have also shown that ionization effects can be neglected during the acceleration phase of the ion expansion. The ion expansion can therefore

be modeled with two ion species, C^{+6} and H^+ , for the case of a CH_n target, or with one ion species for a CD_n target.

The relative behavior of the C^{+6} and H^+ ion species is also noteworthy. We have observed nonreproducible multi-peak structures on the energy distributions of both hydrogen and carbon species, with little correlation between the H^+ and C^{+6} structures. The relative behavior of the ion species indicates that the H^+ ions are preferentially accelerated to higher E/Z than the C^{+6} ions, such that an important fraction of the ion energy is transported by energetic H^+ ions. This result is inconsistent with the assumption of a constant electrostatic potential accelerating the ions to high energies.

The relative behavior of the C^{+6} and H^+ ion species is consistent with the assumption of a spatially and temporally varying ambipolar electric field associated with the plasma pressure. As discussed in Chapter I, the accelerating electric field \bar{E}_o associated with the plasma pressure is given by

$$e \bar{E}_o \approx - \frac{k T_e}{n_e} \nabla n_e.$$

Interferometric and x-ray measurements suggest that steep density gradients and high electron temperatures exist at high laser irradiance. The fluid model presented in Chapter IV describes the ambipolar expansion of hot electrons and either one or two relatively cold ion species from an electron pressure gradient. Although the fluid approximation is not well justified, the model does provide insight to the acceleration of a small group of energetic ions by a large pressure gradient. The model shows that electric fields strong enough to accelerate energetic ions can be created, assuming reasonable electron temperature and density scale length. In the case of multi-species plasma expansions, the model also shows that an ambipolar expansion accelerates lower A_i/Z_i ion species to higher E/Z than ion species with higher A_i/Z_i , explaining the preferential acceleration of H^+ ions over heavier C^{+6} ions.

For the case of an isothermal expansion with a single ion species and a constant electron temperature, the numerical solutions of the fluid equations are shown to be adequately represented by analytical solutions in different regions of the plasma expansion. New analytical

solutions provide a means for launching self-similar solutions from a density profile initially at rest.

Most of the ion measurements presented in this work were obtained for short laser pulse length (75 psec) at high irradiance (10^{16} W/cm²). Another interesting intensity regime for laser fusion is 10^{13} – 10^{14} W/cm² with longer pulse lengths (nsecs). Ion measurements should therefore be performed at lower intensity to see how the energy content in the energetic ions scales with laser intensity. The development and calibration of suitable ion energy detector such a pyroelectrics could also be used to quantify and simplify the ion measurement.

The multi-species fluid model can also be improved by including 2-D effects and a proper treatment of the laser energy deposition. Comparison of the results from the fluid model with those from a PIC (particle in cell) code would also be useful in order to verify the validity of the fluid approximation.

ACKNOWLEDGMENTS

This report was submitted as a dissertation to the Graduate School of the University of Maryland in partial fulfillment of the requirements for the Ph.D. degree.

The author is deeply grateful to Dr. Barret H. Ripin of the Naval Research Laboratory for his suggestions and guidance. His advice, encouragement and friendship throughout this endeavor is very much appreciated. I would also like to express my gratitude to Professor Hans R. Griem of the University of Maryland for his suggestions, continued interest and encouragement.

I have been very fortunate to have conducted my thesis with a very dynamic research group at the Naval Research Laboratory. It is a pleasure to acknowledge fruitful discussions with Steve Bodner, Edgar McLean, John Stamper and John McMahon. Special thanks go to Frank Young for his x-ray measurements and related discussions.

I wish to acknowledge useful discussions and help from Frank Felber for the analytical solutions of the theoretical model and Denis Colombant who instructed me in the use of a

numerical hydrodynamic code. I also wish to acknowledge interesting and stimulating discussions with Carter Armstrong, Orville Barr, Ira Bernstein, Dave Forslund, Herbert Lashinsky, Chuan Liu and Bob Whitlock.

The expert technical assistance of Ed Turbyfill for the maintenance of the target facility and Tom DeRieux for providing the laser shots is appreciated. I also wish to thank Robin McGill and Bob Burns for useful discussions about the experimental apparatus. The expert secretarial services of Pat Fletcher and the typing of most of this dissertation by the Editorial Processing Center of the Technical Information Division at NRL are also highly appreciated.

Finally, I would like to thank my wife, Hélène, for typing part of this dissertation and for her unending support and encouragement during the course of this work.

The research reported here was performed at the Naval Research Laboratory under the auspices of the Department of Energy (formerly U.S. Energy Research and Development Administration). It is also a pleasure to acknowledge receipt of a Hydro-Quebec fellowship (Canada) throughout this work.

APPENDIX A

Right Boundary Conditions

In this appendix, the numerical implementation of the "perfectly absorbing wall" condition required for the right boundary of the computational mesh is described. First we discuss the motivation for our particular choice of boundary conditions. Then, we describe the numerical technique used in the code to implement this condition.

Singling out the continuity equation for the ions and the electrons from Eqs. (4.8) and (4.10) the set of equations describing the plasma expansion, Eqs. (4.8)-(4.11) and (4.6), can be rewritten as

$$\frac{\partial}{\partial t} n_i + \frac{\partial}{\partial x} n_i v_i = 0, \quad (\text{A-1})$$

$$\frac{\partial}{\partial t} v_i + v_i \frac{\partial}{\partial x} v_i = -\frac{Z_i}{A_i} \frac{1}{n_e m_p} \frac{\partial}{\partial x} n_e k T_e, \quad (\text{A-2})$$

$$n_e = Z_1 n_1 + Z_2 n_2, \quad (\text{A-3})$$

$$\frac{\partial}{\partial t} T_e + v_e \frac{\partial}{\partial x} T_e = -\frac{2}{3} T_e \frac{\partial}{\partial x} v_e, \quad (\text{A-4})$$

$$v_e = (Z_1 n_1 v_1 + Z_2 n_2 v_2) / n_e. \quad (\text{A-5})$$

Equations (A-1) through (A-3) are used to describe an isothermal expansion, whereas (A-1) through (A-5) describe an adiabatic expansion.

For the case of a single ion species expanding with a constant, uniform temperature, it is shown in Chapter III, Section C that a portion of the initial exponential density profile propagates to the right while maintaining its shape. This solution corresponds to region III in Fig. 4.2. For the more general case of two ion species and either an isothermal or adiabatic condition, it can also be shown by direct substitution in Eqs. (A-1)-(A-5), that solutions of the form

$$n_1 = A_1(t) e^{-x/L}, \quad (\text{A-6})$$

$$n_2 = A_2(t) e^{-x/L}, \quad (\text{A-7})$$

and

$$n_e = Z_1 A_1(t) e^{-x/L} + Z_2 A_2(t) e^{-x/L} \quad (\text{A-8})$$

also exist in region III, where A_1 and A_2 are time dependent coefficients. This means that the initial exponential density profiles for both ion species can propagate with increasing uniform

velocities without deformation in region III. This property of exponential density profiles is used to set accurate right boundary conditions in the numerical code.

Accurate boundary conditions are required for the N^{th} and $(N-1)^{th}$ cells if N cells are used on the computational mesh. At the end of each complete timestep, the code verifies whether both ion velocities are still uniform for cell number $(N-7)$ through $(N-3)$ inclusively. If this condition is not met, region III of Fig. 4.2 is almost extinguished. The expansion is then terminated and the results are printed. Otherwise, average coefficients $A_1(t)$ and $A_2(t)$ are calculated from cells $(N-7)$ through $(N-3)$ and used in (A-6) and (A-7) to calculate the densities of the last two cells. The velocities and temperature of the last two cells are accordingly determined from the results of cells $(N-7)$ through $(N-3)$. Five cells are used in the above process in order to average out the numerical noise introduced in the solution.

References

1. J. Nuckolls, L. Wood, A. Thiessen, G. Zimmerman, *Nature* **239**, 139 (1972).
2. J.S. Clarke, H.N. Fisher, R.J. Mason, *Phys. Rev. Lett.* **30**, 89 (1973).
3. K.A. Bruckner, S. Jorna, *Rev. Mod. Phys.* **46**, 325 (1974).
4. Yu.V. Afanas'ev, N.G. Basov, P.P. Volosevich, E.G. Gamalii, O.N. Krokhin, S.P. Kurdyumov, E.I. Levanov, V.B. Rozanov, A.A. Samarskii and A.N. Tikhonov, *Sov. Phys. -JETP* **21**, 68 (1975).
5. L. Spitzer, "Physics of Fully Ionized Gases", 2nd ed., Wiley (Interscience), New York (1967).
6. T.W. Johnston and J.M. Dawson, *Phys. Fluids*, **16**, 722 (1973).
7. F.F. Chen, in "Laser Interactions and Related Phenomena" Vol. 3, Plenum Press, (1974).
8. B.H. Ripin, J.M. McMahon, E.A. McLean, W.M. Manheimer and J.A. Stamper, *Phys. Rev. Lett.* **33**, 634 (1974).
9. B.H. Ripin, F.C. Young, J.A. Stamper, C.M. Armstrong, R. Decoste, E.A. McLean, and S.E. Bodner, *Phys. Rev. Lett.* **39**, 611 (1977).
10. D.W. Phillion, W.L. Kruer, and V.C. Rupert, *Phys. Rev. Lett.* **39**, 1529 (1977).
11. R.L. Morse and C.W. Nielson, *Phys. Fluids*, **16**, 909 (1973).
12. M. Mattioli, *Plasma Phys.*, **13**, 19 (1971).
13. Yu.V. Afanas'ev and V.B. Rozanov, *Sov. Phys. - JETP* **35**, 133 (1972).
14. E.E. Lovetskii, A.N. Polyanichev and V.S. Fetisov, *Sov. J. Plasma Phys.*, **1**, 422 (1975).
15. R.R. Goforth and P. Hammerling, *J. Appl. Phys.* **47**, 3918 (1976).
16. Yu.A. Bykovskii, N.N. Degtyarenko, V.F. Elesin, Yu.P. Kozyrev and S.M. Sil'nov, *Sov. Phys. - Tech. Phys.* **15**, 2020 (1971), *Sov. Phys. - JETP* **33**, 706 (1971).
17. F.E. Irons, R.W.P. McWhirter and N.J. Peacock, *J. Phys. B*, **5**, 1975 (1972).

18. F.E. Irons and N.J. Peacock, *J. Phys. B*, **7**, 2084 (1974).
19. B.H. Ripen et al., *NRL Report 7838*, Ch. IV (Oct. 1974).
20. P.M. Campbell, R.R. Johnson, F.J. Mayer, L.V. Powers and D.C. Slater, *Phys. Rev. Lett.*, **39**, 274 (1977).
21. R.A. Haas, W.C. Mead, W.L. Kruer, D.W. Phillion, H.N. Kornblum, J.D. Lindl, D. MacQuigg, V.C. Rupert and K.G. Tirsell, *Phys. Fluids*, **20**, 322 (1977).
22. J. Martineau, M. Rabeau, J.-L. Bocher, J.-P. Elie and C. Patou, *Optics Commun.*, **18**, 347 (1976).
23. A.W. Ehler, *J. Appl. Phys.*, **46**, 2464 (1975).
24. B. Luther-Davies and J.L. Hughes, *Optics Commun.*, **18**, 351 (1976).
25. B. Grek, H. Pepin, T.W. Johnston, J.N. Leboeuf, H.A. Baldis, *Nuclear Fusion*, **17**, 1165 (1977).
26. R. Decoste and B.H. Ripin, *Rev. Sci. Instrum.*, **48**, 232 (1977).
27. R. Decoste and B.H. Ripin, *Appl. Phys. Lett.*, **31**, 68 (1977).
28. F. Young and G.H. McCall, *Bull. Am. Phys. Soc.*, **22**, 1129 (1977).
29. R. Decoste and B.H. Ripin, *Phys. Rev. Lett.*, **40**, 34 (1978).
30. H. Hora, "Laser Interaction and Related Plasma Phenomena", ed. by H.J. Schwarz and H. Hora, Plenum Press, New York, (1971).
31. J.A. Stamper, K. Papadopoulos, R.N. Sudan, S.O. Dean, E.A. McLean, and J.M. Dawson, *Phys. Rev. Lett.*, **26**, 1012 (1971).
32. J.A. Stamper and B.H. Ripin, *Phys. Rev. Lett.*, **34**, 138 (1975).
33. M.G. Drouet and R. Bolton, *Phys. Rev. Lett.*, **36**, 591 (1976).
34. J.A. Stamper, E.A. McLean and B.H. Ripin, *NRL Memo Report 3758*, (April 1978).
35. J.A. Stamper and D.A. Tidman, *Phys. Fluids*, **16**, 2024 (1973).
36. D.A. Tidman, *Phys. Rev. Lett.*, **35**, 1228 (1975).
37. D.G. Colombant and N.K. Winsor, *Phys. Rev. Lett.*, **38**, 697 (1977).

38. R.S. Craxton and M.G. Haines, Phys. Rev. Lett., **35**, 1336 (1975).
39. R.S. Craxton, "A Numerical Investigation of Magnetic Fields in Laser-Produced Plasmas", Ph.D. thesis, Imperial College, London (1976).
40. N.A. Krall and A.W. Trivelpiece, "Principles of Plasma Physics," McGraw-Hill, New York (1973).
41. K. Itoh and S. Inoue, Phys. Rev. Lett., **37**, 508 (1976).
42. G. Schmidt, "Physics of High Temperature Plasmas", Academic Press, New-York (1966).
43. V.L. Ginzburg, "The Propagation of Electromagnetic Waves in Plasmas," Pergamon Press, New York (1964), 2nd ed., 1970.
44. V.P. Silin, Sov. Phys. JETP Lett., **21**, 152 (1975).
45. D. Baboneau, G. Di Bona, P. Chelle, M. Decroisette and J. Martineau, Phys. Lett., **57A**, 247 (1976).
46. P. Mulser and C. Van Kessel, Phys. Lett., **59A**, 33 (1976).
47. J.S. Pearlman and J.P. Anthes, Appl. Phys. Lett., **27**, 581 (1975).
48. F.C. Young, R.R. Whitlock, R. Decoste, B.H. Ripin, D.J. Nagel, J.A. Stamper, J.M. McMahon and S.E. Bodner, Appl. Phys. Lett., **30**, 45 (1977).
49. B. Yaakobi and T.C. Bristow, Phys. Rev. Lett., **38**, 350 (1977).
50. W.M. Manheimer, Phys. Fluids, **20**, 265 (1977).
51. W.M. Manheimer, D.G. Colombant and B.H. Ripin, Phys. Rev. Lett., **38**, 1135 (1977).
52. R.J. Faehl and W.L. Kruer, Phys. Fluids, **20**, 55 (1977).
53. B.H. Ripin, P.G. Burkhalter, F.C. Young, J.M. McMahon, D.G. Colombant, S.E. Bodner, R.R. Whitlock, D.J. Nagel, D.J. Johnson, N.K. Winsor, C.M. Dozier, R.D. Bleach, J.A. Stamper and E.A. McLean, Phys. Rev. Lett., **34**, 1313 (1975).
54. D.W. Forslund, J.M. Kindel and K. Lee, Phys. Rev. Lett., **39**, 284 (1977).
55. J.P. Freidberg, R.W. Mitchell, R.L. Morse and L.I. Rudinski, Phys. Rev. Lett., **28**, 795 (1972).

56. K.G. Estabrook, E.J. Valeo and W.L. Kruer, *Phys. Fluids*, **18**, 1151 (1975).
57. D.W. Forslund, J.M. Kindel, K. Lee and E.L. Lindman, *Phys. Rev. Lett.*, **36**, 35 (1976).
58. B.H. Ripin, *Appl. Phys. Lett.*, **30**, 134 (1977).
59. R.C. Malone, R.L. McCrory and R.L. Morse, *Phys. Rev. Lett.*, **34**, 721 (1975).
60. D.T. Attwood, D.W. Sweeney, J.M. Auerbach and P.H.Y. Lee, *Phys. Rev. Lett.*, **40**, 184 (1978).
61. R. Fedosejevs, I.V. Tomov, N.H. Burnett, G.D. Enright and M.C. Richardson, *Phys. Rev. Lett.*, **39**, 932 (1977).
62. K. Lee, D.W. Forslund, J.M. Kindel and E.L. Lindman, *Phys. Fluids*, **20**, 51 (1977).
63. F. Mulser and C. van Kessel, *Phys. Rev. Lett.*, **38**, 902 (1977).
64. A.V. Gurevich, L.V. Pariiskaya and L.P. Pitaevskii, *Sov. Phys. - JETP*, **22**, 449 (1966).
65. J.E. Allen and J.G. Andrews, *J. Plasma Phys.*, **4**, 187 (1970).
66. F.S. Felber and R. Decoste, *Phys. Fluids*, **21**, 520 (1978).
67. J.E. Crow, P.L. Auer and J.E. Allen, *J. Plasma Phys.*, **14**, 65 (1975).
68. E.J. Valeo and I.B. Bernstein, *Phys. Fluids*, **19**, 1348 (1976).
69. K.A. Bruckner and R.S. Janda, *Nucl. Fusion*, **17**, 1265 (1977).
70. J. McMahon, R. Lehmberg, B. Ripin, and J. Stamper, *NRL Memo Report 3315*, Ch. II, S.E. Bodner, ed. (Aug. 1976).
71. J. McMahon, R. Lehmberg and R. McGill, *NRL Memo Report 3591*, Ch. II, S. Bodner, ed. (Oct. 1977).
72. B. Ripin, R. Decoste, E. McLean, R. McGill, J. Stamper, R. Whitlock and F. Young, *NRL Memo Report 3591*, Ch. III, S. Bodner, ed. (Oct. 1977).
73. F.C. Young, *NRL Memo Report 3591*, Ch. III, S. Bodner, ed. (Oct. 1977).
74. C.A. Armstrong, R. Decoste, F.C. Young and B.H. Ripin, *Bull. Am. Phys. Soc.* **22**, 1128 (1977), (to be published).

75. E.A. McLean, R. Decoste, B.H. Ripin, J.A. Stamper, H.R. Griem, J.M. McMahon, and S. Bodner, *Appl. Phys. Lett.*, **31**, 9 (1977).
76. H.J. Karr, Los Alamos Sci. Lab. report LAMS-2916 (1963).
77. J.E. Osher, in "Plasma Diagnostic Techniques", edited by R.H. Huddleston and S.L. Leonard (Academic, New York, 1965).
78. S.S. Glaros, K.G. Tirsell, V.C. Rupert, H.C. Catron, V.W. Slivinsky, *Bull. Am. Phys. Soc.* **21**, 1120 (1976), UCRL Report 78427 (Nov. 1976).
79. D.C. Slater and F.J. Mayer, KMS report U568 (1976).
80. J.N. Olsen, G.W. Kuswa, and E.D. Jones, *J. Appl. Phys.* **44**, 2275 (1973).
81. F.J. Allen, *Rev. Sci. Instrum.* **42**, 1423 (1971).
82. R.R. Goforth, *Rev. Sci. Instrum.* **47**, 548 (1976).
83. M. Oron and Y. Paiss, *Rev. Sci. Instrum.* **44**, 1293 (1973).
84. H.H. Fleischmann, D.E.T.F. Ashby, and A.V. Larson, *Nucl. Fusion* **5**, 349 (1965).
85. P.T. Kirstein, G.S. Kino, and W.E. Waters, "Space Charge Flow", McGraw-Hill, New-York (1967).
86. M Kaminsky, "Atomic and Ionic Impact Phenomena on Metal Surfaces", Academic Press Inc., New York (1965).
87. K.H. Krebs, *Fortschritte der Physik* **16**, 419 (1968).
88. L.N. Large, and W.S. Whitlock, *Proc. Phys. Soc.*, **79**, 148 (1962).
89. B.H. Ripin, Univ. of Maryland Techn. Report 71-038 (1970).
90. B.H. Ripin and R. Decoste, NRL Memorandum Report 3494 (May 1977).
91. J.S. Pearlman, *Rev. Sci. Instrum.* **48**, 1064 (1977).
92. R. Decoste, B.H. Ripin and D.G. Colombant, *Bull. Am. Phys. Soc.*, **22**, 1129 (1977).
93. V.S. Nikolaev, I.S. Dmitriev, L.N. Fateeva, and Ya. A. Teplova, *Sov. Phys. - JETP* **13**, 695 (1961).
94. V.S. Nikolaev, L.N. Fateeva, I.S. Dmitriev, and Ya. A. Teplova, *Sov. Phys. - JETP* **14**, 67 (1962).

95. J.S. Pearlman, M.K. Matzen and R.L. Morse, Bull. Am. Phys. Soc., **22**, 1224 (1977).
96. U. Feldman, G.A. Doschek, D.K. Prinz and D.J. Nagel, J. Appl. Phys. **47**, 1341 (1976).
97. G.A. Doschek, U. Feldman, P.G. Burkhalter, T. Finn and W.A. Feibelman, J. Phys. B: Atom. Molec. phys., **10**, L745 (1977).
98. B.H. Ripin, NRL Memo Report 3684, (Dec. 1977).
99. D.W. Forslund, J.M. Kindel, K. Lee and E.L. Lindman, Bull. Am. Phys. Soc., **20**, 1377 (1975)
100. P. Mulser, Plasma Phys., **13**, 1007 (1971).
101. A.V. Gurevich, L.V. Pariiskaya and L.P. Pitaevskii, Sov. Phys. JETP **22**, 449 (1966), and **36**, 274 (1973).
102. J.P. Boris and D.L. Book, J. Compt. Phys., **11**, 38 (1973).
103. J.P. Boris, NRL Memo Report 3237 (March 1976).